Magnetic fluidized bed for sample preconcentration and immunoextraction in microfluidic systems

Sanae Tabnaoui

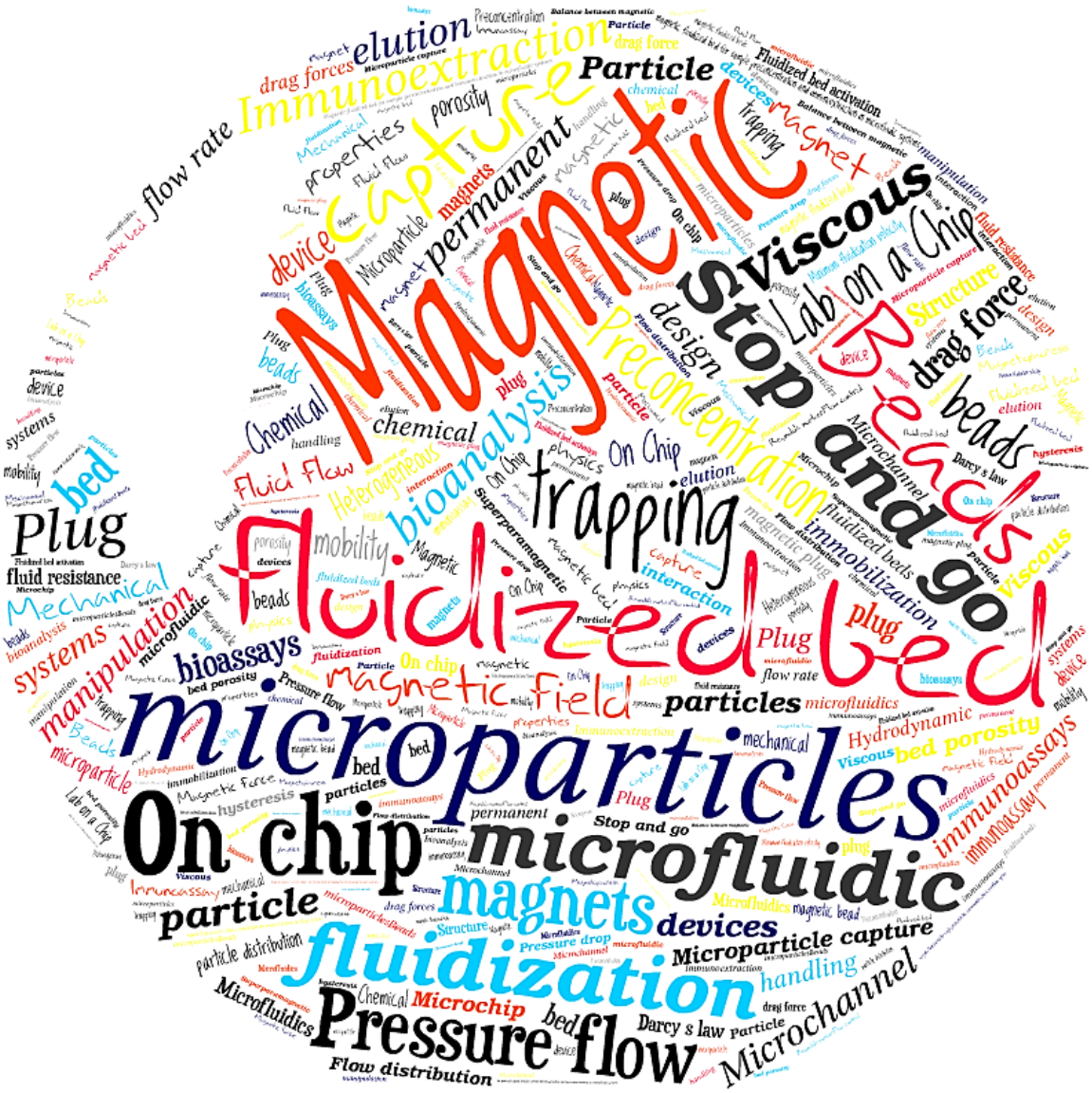

Magnetic fluidized bed for sample preconcentration and immunoextraction in microfluidic systems

SanaeTabnaoui

2008-2012

THESE DE DOCTORAT DE
L'UNIVERSITE PIERRE ET MARIE CURIE

Spécialité
Chimie Analytique et Chimie Physique (ED 388)

Présentée par

Sanae Tabnaoui

Pour obtenir le grade de

DOCTEUR de l'UNIVERSITÉ PIERRE ET MARIE CURIE

Sujet de la thèse :

Magnetic fluidized bed for sample preconcentration and immunoextraction in microfluidic systems

Soutenue le 10 septembre 2012 devant le jury composé de :

Mme. Nicole PAMME	Rapporteur
M. Olivier SANDRE	Rapporteur
M. Marc FERMIGIER	Examinateur
Mme. Christine PEPONNET	Examinateur
Mme. Valérie CABUIL	Invité
Mme. Stéphanie DESCROIX	Invité
M. Laurent MALAQUIN	Co-directeur de thèse
M. Jean-Louis VIOVY	Directeur de thèse

Institut Curie

UMR 168 Physico-Chimie

11 rue Pierre et Marie Curie

75005 Paris

Remerciements

Jean-Louis Viovym'a donné l'opportunité de travailler dans un domaine intéressant et très stimulant avec des projets représentant les défis de demain.
Cher Jean-Louis, malgré ton emploi du temps chargé, merci d'avoir toujours ta porte ouverte pour un doctorant en recherche de conseils ou d'une seconde opinion (il est vrai que même s'il faut prendre son ticket, ta claire vision et ta grand culture scientifique méritent bien d'attendre un peu pour un entretien avec son Gourou de thèse!). J'ai apprécié la liberté et la confiance que tu m'as accordées, cela m'a permis de mener ce travail de recherche dans les meilleures conditions.

Laurent Malaquin, un mentor, sans qui cette aventure n'aurait pas eu lieu.

Cher Laurent, ta passion, ton insatiable curiosité et ton énergie ont indéniablement contribué à la richesse de ces quatre années de thèse, aussi bien au plan scientifique, qu'au plan humain. Un grand merci pour tes conseils toujours judicieux (vecteur ou pas vecteur ?).

Stéphanie Descroix, l'incarnation du modèle féminin scientifique pour l'enthousiasme qu'elle suscite autour d'elle.
Ma chère Stéphanie, je souhaite te remercier pour cette dernière année qui n'aurait pas pu prendre une si jolie tournure sans ta présence.

GiuliaCarzedda, qui joue un rôle essentiel pour nous simplifier toutes les formalités administratives au quotidien.
Cher Giulia, je te remercie pour ta joie de vivre qui donne à ce grand bureau tout son charme, merci également pour ta patience et ta disponibilité.

Brigitte Dasilva, dont l'accueil chaque matin m'a donné tout plein d'entrain pour attaquer la journée.
Chère Brigitte, je te remercie pour tes douces parolesrendant mes journées les plus maussades pleines de perspectives, me permettant ainsi de surmonter les moments les plus difficiles. Merci pour ces moments de bavardages, de fous rires et surtout merci pour ton amitié.

François-Damien que je remercie tout spécialement.

Cher François-Damien, merci de m'avoir accompagnée au quotidien. Partager mon bureau avec toi fut un grand plaisir, nos discussions, tes suggestions et certainement nos pausesgoûter sont autant de moments qui marqueront ces formidables années de doctorat.

Je veux également témoigner de ma sincère reconnaissance à **N**icole Pamme et à **O**livier Sandre qui ont assumé la tâche de rapporteurs de mon manuscrit, ainsi qu'aux autres membres du jury : **V**alèrieCabuil, présidente du jury (qui m'a vu faire mes premiers pas en recherche), **M**arc Fermigier et **C**hristine Peponnet.

Ces travaux ont pu bien sûr être réalisés grâce au cadre épanouissant et exceptionnel que procure notre charmante *" Viovy's team "*. En vrac, je tiens donc à exprimer ma gratitude à toutes les personnes qui ont un jour fait partie de cette formidable équipe MMBM et qui ont su entretenir ce nuage de bonne humeur.

Je tiens à remercier toute ma famille pour leur fidèle soutien avec une pensée toute particulière pour mes parents.


Maeva
Pierre
Youba
Bruno
Giovanni
Laurent
Vélan
Benoit
Stéphanie
Julien
Nadège
Scott
Jean Louis
Valérie Cabuil
Karla
Nicole pamme
Olivier Sandrine
Guillaume
Anaïs
Jérôme
Hassan
Mina
Jamila
Patrick

Abstract

We developed a novel microfluidic device, in which magnetic particles are maintained dynamically in a microchamber, and undergo hydrodynamic recirculation. From a physical point of view, this relatively dense dynamical system is reminiscent of fluidized beds, and its behaviour has been interpreted in this frame. Gravitational fluidized beds were widely investigated in the macroscopic worlds, but their integration in microfluidics is hardly possible as they provide a very limited dynamic range. Magnetic forces offer the opportunity to extend the concept of fluidized bed to miniaturized systems and to our knowledge, this is the first implementation of a magnetically stabilized fluidized in microfluidics. Previous systems using magnetic microparticles in microfluidics consisted in either low density static or dynamic systems, with a low capacity and efficiency, or static systems in which columns

are trapped in a strong and local field potential. These systems have a higher potential capacity, but limited capture efficiency. The new system developed here bridges the gap between these two previous strategies and opens new regimes of operation combining a relatively high density of magnetic particles, for high capacity, an active hydrodynamic stirring, for increased kinetics, and a relatively high flow rate, allowing concentration of very dilute analytes from a rather large sample volume. This system was validated in an immunoassay, using a stop-and-go strategy taking full advantage of the dynamic nature of the magnetic microcolumn. We believe, however, that it also has strong potential of preconcentration of analytes from ml to µl or nl–sized sample downstream microfluidic analysis modules. In particular, this laboratory is involved in the EU project Nadine, aimed at developing early diagnosis of Alzheimer's disease in blood.

Résumé

Nous avons développé un nouveau système microfluidique où des particules magnétiques entraînées par un flux hydrodynamique restent confinées dynamiquement grâce à un champ magnétique au sein d'une micro-chambre. Ces particules sont employées comme support pour un immuno-dosage. Le projet européen Nadine dans lequel s'inscrit ce travail vise au développement d'un module destiné au diagnostic précoce de la maladie d'Alzheimer à partir d'échantillons sanguins. Physiquement, ce système dense et dynamique évoque un lit fluidisé, et son comportement a été interprété dans cette perspective. Bien que les lits fluidisés gravitationnels aient été largement étudiés à une échelle macroscopique, leurs intégrations en microfluidique demeurent impossible, la force de gravitation n'équilibrant plus les forces hydrodynamiques à cette échelle. Les forces magnétiques offrent l'opportunité d'étendre le principe du lit fluidisé aux systèmes miniaturisés, et à notre connaissance, notre système constitue la première réalisation d'un lit fluidisé stabilisé magnétiquement en microfluidique. Les systèmes antérieurs qui employaient des particules magnétiques étaient des systèmes statiques ou dynamiques de faibles densités associés à des efficacités et des capacités de capture limitées. Ce nouveau système autorise une forte densité en particules (nécessaire pour une capacité élevée), une agitation hydrodynamique (pour accroître la cinétique de capture et son efficacité) et un flux élevé (permettant la concentration d'analytes très diluées). Ce module a été validé à l'aide d'un immuno-dosage-modèle (IgG/anti-IgG), par l'emploi d'une stratégie de type stop-and-go, qui permet de bénéficier pleinement de la nature dynamique des colonnes magnétiques. Le système permet par ailleurs l'enrichissement continu en analytes du lit de particules, ce qui augmente significativement la sensibilité de détection (LOD: 1 ng/mL ~ 6.5 pM).

Énigme

Pendant ces dernières années, j'ai travaillé avec un partenaire incontournable mais néanmoins séditieux qui profitait de la moindre inattention de ma part pour prendre la clé des champs.

Il s'agit d'un petit bonhomme qui devient extrêmement violent dès qu'il se trouve à proximité d'un objet métallique.

Qui est-il ?

Mon aimant permanent qui exhibe fièrement ces 1.4 Tesla. C'est lui qui m'a donnée autant de sueurs froides pendans mes expèriences !

Table of contents

Nomenclature

Abbreviations and Acronyms

µTAS	*Micro Total Analysis System*
2D	*bi-dimensional*
3D	*tri-dimensional*
Ab, Abs	*Antibody, Antibodies*
Ag, Ags	*Antigen, Antigens*
AD	*Alzheimer disease*
ASW	*Acoustic Standing Wave*
BSA	*Bovine Serum Albumin*
COC	*Cyclic Olefin Copolymer*
CSF	*CerebroSpinal Fluid*
DEP	*Dielectrophoretic*
DNA	*DeoxyriboNucleic Acid*
EDL	*Electric Double Layer*
ELISA	*Enzyme Linked Immunosorbent Assay*
EOF	*Electroosmotic Flow*
FEM	*Finite Element Method*
FITC	*Fluorescein Isothiocynate*
FRET	*Fluorescence Energy Transfer*
IDT	*InterDigital Transducer*
IgG	*Immunoglobulin G*
LAT	*Latex Agglutination Test*
LOC	*Lab-On-a-Chip*
LOD	*Limit Of Detection*
MAESFLO	*Microfluidic Flow Control Systems*
NdFeB	*Neodymium Iron Boron*
PBS	*Phosphate Buffer Saline*
PCR	*Polymerase Chain Reaction*
PDMA-AGE	*Poly(dimethylacrylamide-allylglycidyl)*
PDMS	*Poly(dimethylsiloxane)*
PEEK	*Poly(etheretherketone)*
PMMA	*Poly(methyl methacrylate)*
POC	*Point Of Care*
RIA	*RadioImmunoAssay*
SDS	*Sodium Dodecyl Sulphate*
SU-8	*Epoxy based negative photoresist*
USW	*Ultrasonic Standing-Wave*

List of Symbols

Symbol	*Description*	*Unit*
K	*Kozeny constant*	≈ 5
ξ	*magnetophoretic mobility*	
Re	*Reynolds number*	
Re^*	*modified Reynolds number*	
μ_r	*relative magnetic permeability*	$-$
χ_{eff}	*effective susceptibility*	$-$
χ_r	*relative susceptibility*	$-$
N_l	*total number of particles*	$-$
χ	*magnetic susceptibility*	$-$
χ_{mat}	*intrinsic material susceptibility*	$-$
χ_p	*susceptibility of the particles*	$-$
χ_w	*susceptibility of the surrounding medium (water)*	$-$
$\chi_{\ mass}$	*mass susceptibility*	$m^3.Kg^{-1}$
ε	*void fraction or porosity*	$-$
C	*solid fraction*	$-$
Pe	*Péclet number*	$-$
N_d	*demagnetization factor*	*($N_d = 1/3$ for a sphere)*
U_{mf}	*minimum fluidizing velocity*	$m.s^{-1}$
S_v	*specific surface area per unit volume*	m^2
A	*bed cross sectional area*	m^2
ν	*kinematic viscosity*	$m^2.s^{-1}$
D	*diffusion coefficient*	$m^2.s^{-1}$
V_p	*volume of particle*	m^3
Q	*flow rate*	$m^3.s^{-1}$
K_B	*Boltzmann constant*	$1.38 \cdot 10^{-23} J.K^{-1}$
P_{atm}	*atmospheric pressure*	$1atm \sim 1\ bar \sim 15\ psi$
R	*resistance*	$Pa.s.m^{-3}$
	R_0 *system resistance without plug*	
	R_s *sensor resistance*	
	R_2 *output resistance*	
	R_{peek} *PEEK tube's resistance*	
	R_p *plug resistance*	
	R_e *Reynolds number*	
	R_{0p} *system resistance with plug*	
$\vec{H}$	*magnetic field strength*	$A.m^{-1}$
H_c	*coercive field*	$A.m^{-1}$
$\vec{M}$	*magnetization*	$A.m^{-1}$
	M_r *remanent magnetization*	$A.m^{-1}$
	M_s *Intrinsic spontaneous magnetization*	$A.m^{-1}$

	M_{sat}	*saturation magnetization*	$A.m^{-1}$
$\vec{m}$	*magnetic moment*		$A.m^2$
E_T	*thermal energy*		J
E_m	*magnetic energy*		J
K_{eff}	*anisotropy energy density*		$J.m^{-3}$
T_c	*Curie temperature*		K
F	*force*		N
	$\vec{F}_{buo}$	*buoyancy force*	
	$\vec{F}_{drag}$	*viscous drag force*	
	$\vec{F}_g$	*gravitational force*	
	$\vec{F}_{mag}$	*magnetic force*	
	$\vec{F}_b$	*force on the bed*	
	$\vec{F}_{1-P}$	*magnetic force on a single particle*	
μ_0	*vacuum permeability*		N/A^{-2}
ΔP	*pressure drop*		Pa
Δp_{mf}	*minimum fluidization pressure*		Pa
η	*dynamic viscosity*		$Pa.s$
$\vec{B}$	*magnetic flux density*		$T\ or\ V.s.m^{-2}$
ρ_f	*fluid density*		$kg.m^{-3}$
ρ_p	*particle density*		$kg.m^{-3}$
d_c	*critical particle diameter*		m
d_s	*superparamagnetic diameter size*		m
d_{Sv}	*Sauter diameter*		m
D_h	*hydraulic channel's diameter*		m
d_p	*particle diameter*		m
r_p	*particle radius*		m
L	*length of the bed*		m
d_p	*particle diameter*		m
k	*permeability of the bed*		m^2
l	*dimension of the system*		m
w	*width*		m
g	*gravitational acceleration*		$m.s^{-2}$
U	*interstitial velocity*		$m.s^{-1}$
U_0	*superficial velocity*		$m.s^{-1}$
v	*velocity of the fluid*		$m.s^{-1}$
τ_0	*length of time characteristic of the material*		s
τ	*length of time*		s

Introduction

One of the main and specific advantages of microfluidics is its ability to manipulate extremely small volumes of fluids, largely below $one\mu L$. This possibility has, in particular, opened in the last years new avenues towards applications in biology out of reach of conventional systems. For instance, in the field of "digital biology", taken in its largest sense, e.g. analysis of single molecules or single cells, it allows to perform biochemical reactions in extremely small volume, increasing dramatically the dynamics and reliability of reactions. This has found beautiful applications, e.g. in single DNA molecule "digital PCR", and in several next generation sequencing technologies. Another advantage of miniaturization in microfluidics is that it follows the progress of miniaturization in detectors and optics, offering strong potential gain in terms of sensitivity. Many detectors or detection methods, such microarrays, fluorescence, electrochemistry, are essentially limited by concentration of the analyte in the analysis volume (or on the sensor surface, for a surface-based sensing), so if the content of a rather large sample can be concentrated down to a *sub-*μL volume, the sensitivity can be increased dramatically. The key question in this case, however, lies in the above "if", which is now a major bottleneck for applying microfluidics to sensitive or ultra-sensitive detection. This is particularly relevant to diagnosis applications, in which some of the new biomarkers can be present at a very low concentration. The present work was developed, in particular, in an attempt to elaborate early diagnosis of Alzheimer disease. For different reasons and in particular the presence of the blood-brain barrier, it is expected that many potential biomarkers are present in blood at a very low concentration, typically in the Pico Molar range. In terms of quantity of analytes, it is thus not appealing to start from only one μl of sample or less, the typical volume that one can accommodate in a microfluidic chamber, and a pre-concentration step from a rather large volume (typically of the order of one to several mL) is a prerequisite. This is the challenge to which this Ph.D. work was addressed.

In the macroscopic world, purification, extraction and concentration are most commonly performed using a solid phase, e.g. through a chromatographic or immunoaffinity process. The implementation of chromatography microcolumns in microfluidic systems, however, raise serious challenges related in particular to increasing difficulties to get a homogeneous packing, high backpressures difficult to handle in microfluidic systems, and tedious fabrication. The use of superparamagnetic beads as a solid state support has also become very popular in the macroscopic world: magnetic particles bound to the analyte of interest are retained with a magnet, while the supernatant fluid is removed. This process can be multiplexed, e.g. using multiple magnets at the bottom of microtiter plates, but it still suffers from significant constraints, notably due to (i) mass transfer limitations, (ii) the need of relatively large elution volumes, and (iii) poor mixing and washing efficiencies.

The use of superparamagnetic particles in microfluidic systems allows to alleviate many of the above problems: it presents the benefit of a large surface-to-volume ratio and flexible surface functionalization, whereas the magnetic properties of the microparticles allow for easy non-contact manipulation, and the formation of microcolumns in a magnetic gradient creates a very convenient spontaneous packing. Various magnetic based systems were proposed in the past by our group [1] and others [2], [3] and interesting performances were reported. Serious limitations remained, however, earlier systems developed in our group involved either an immobilized matrix of large magnetic particles (4), or a "plug" maintained in place by a pair of magnets facing each other across the microchannel[1]. In the first system, the magnetic elements are large and immobile so it is limited by mass-transfer or reaction kinetics. In the second system, when the flow rate increases, a "fracture" regime occurs, inducing inhomogeneous perfusion of the plug and reduced efficiency. We developed in this Ph.D. work a new microchannel and field geometry, which overcomes the above limitations and increases sensitivity to around 1 pMolar.

The manuscript is organized as follows:

In chapter one, we present the basic physics of microfluidics as well as the use of magnetic particles in bioanalysis. In the last part of the chapter, we describe the different technical aspect of microparticles manipulation and the physical methods to study their behaviour.

The second chapter is firstly consecrated to the physical parameters governing the hydrodynamic behaviour of microparticles as magnetic forces, viscous force and to the microchip design and microparticles principle. Secondly, it consecrated to the concept and theory relative with fluidized bed. Thirdly, we describe the different strategies explored in the microfluidic design and subsequently, the capture and the retention of the microparticles in this magnetic fluidized bed device are presented. Finally, the hydrodynamic response of plug in this new device is discussed.

The third chapter deals with the characteristic and optimisation of the protocol off-chip, immunoextraction on-chip, in particular, the extraction of the markers present at very lowconcentration from biological liquids.

Chapter I. Magnetic handling of particles in microfluidic devices

1. Microfluidics toward a Lab-on-a-Chip

a. History and state-of-the-art

The historical beginnings of microfluidics are difficult to point accurately. Indeed, in the 1940s, the implementation of high-pressure liquid chromatography and gas chromatography have required fluid manipulation at the microscale with high precision [4], [5]. In 1975, Terry reported the first proof of concept of a miniaturized analytical silicon made device, through a gas chromatographic analyser. This device was efficient enough to separate a simple mixture of model compounds in a few seconds[6]. Although this early proof of concept was very promising, the real development of microfluidics as a specific domain in science, and the name "microfluidics" itself, emerged in the 1990s thanks to the know-how developed by the Microelectronics community. In 2006, microfluidics has been defined by G.M. Whitesides as "the science and the technology of systems that process or manipulate small (10^{-9} to 10^{-8}L) amounts of fluids, using channels with dimensions of tens to hundreds of micrometres."[7].

To illustrate this definition, Figure I.1shows the characteristic sizes of microfluidic devices.

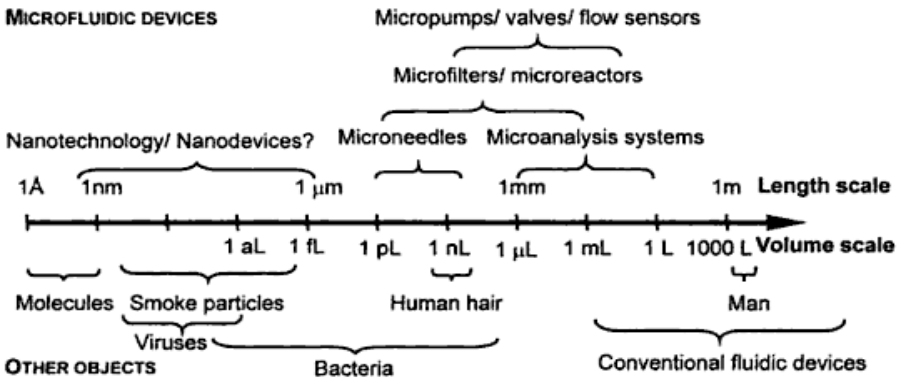

Figure I.1: Size characteristics of microfluidic devices [8].

During the early emerging phase of microfluidics, the community of analytical chemistry took an active part in miniaturized analytical devices, to integrate the different steps of the analytical chain such as the sample pre-treatment, analytes separation and detection within the same device. In 1990, Andreas Manz introduced the concept of miniaturized micro total analysis system (μTAS). Thereafter, microfluidics raised a strong interest among various scientific communities, who proposed various applications. Notably, microfluidics appears as a powerful toolbox with numerous already developed applications in biology and life sciences, and rapidly emerging ones in chemistry, medicine, and environment. Such progress and

the increasing level of complexity associated with it requiredin particular new tools for of liquids handling, and therefore the development and the integration of micro pumps and valves[9–11],Thus, thefastdevelopment of miniaturized fluidic systems is directly connected with the ability to make new types of microstructures or to duplicate existing structures at micro-scale levels.

The current microfabrication techniques, such as micromachining, soft or hard lithography, printing, embossing, injection moulding have been developed and optimized for different materials. Silicon, glass and elastomer have beenthe mostly used materials for microchip microfabrication [12]. Nevertheless, in thelast years, silicon tends to be usedless and less because of its laborious microfabrication, its optical opacity and difficulties to integrate other components. G. Withesides was among the early pioneers in this domain[13]. Glass and silicon, mostly used during the early developments of microdevices, were progressively replaced by polymeric materials such as poly(dimethylsiloxane) (PDMS), an elastomer which is optically transparent, easy to mould and to be used by non-experts. At present,PDMS is the most commonly used material to fabricate microfluidic systems at the research laboratory level [14]. This material, however, is not the ideal one for many industrial applications, and new materials based on mouldable thermoplastics such as COC, Polycarbonate, PMMA, are emerging. The accession to new materials and innovative techniques dedicated to the microfluidic systems' fabrication are continually evolving and already gave rise to many reviews [15], [16].

In the present work, we used PDMS microchip fabricated by soft lithography. Such a technique is particularly useful for pattern replication as it enables rapid prototyping of microfluidic devices and with no need of a cleanroom. Herein, are briefly described the properties, Table 1. For more details, please refer to [17].

Property	Characteristics	Consequence
Optical	Transparent; UV cut-off, 240 nm	Optical detection from 240 to 1100 nm.
Electrical	Insulating; breakdown voltage, $2 \cdot 10^7$ V/m	Allows embedded circuits; and the use of electrokinetic transport and separation
Mechanical	Elastomeric; tunable Young's modulus, typical value of ~750 kPa.	Conforms to surfaces; allows actuation by reversible deformation; facilitates release from moulds. Does not withstand high pressures
Thermal	Insulating; thermal conductivity 0.2 W/(m · K); coefficient of thermal expansion, 310 µm/(m · ° C); stable up to ~300°C.	Can be used to insulate heated solutions; does not allow easy dissipation of resistive heating from electrophoretic separation.
Interfacial	Low surface free energy ~ 20 erg/ cm2.	Replicas release easily from moulds; can be reversibly sealed to materials; not wetted by water unless oxidized to SiOH presenting surface.
Permeability	Impermeable to liquid water; permeable to gases and nonpolar organic solvents.	Contains aqueous solutions in channels; allows gas transport through the bulk material; incompatible with many organic solvents.
Reactivity	Inert; can be oxidized by exposure to a plasma.	Unreactive toward most reagents; surface can be etched; can be modified to be hydrophilic and also reactive toward silanes.
Toxicity	Nontoxic	Can be implanted in vivo; supports mammalian cell growth.

Table 1: The main physical and chemical properties of PDMS (adapted from ref[18]).

Besides these microfabrication progresses, an important contribution towards the integration of complex bioanalytical processes in microdevices lead to the creation of simple methods to fabricate pneumatically activated valves[19], [20], mixers[21–23]and pumps [24][25]. To handle such microfluidic elements it is of high importance to finely control the fluid within

the device and thus to understandthe physical phenomena involved in fluid transport in microchannels[26–28]. The manipulation of fluids in microenvironments, such as channels with typical dimensions of tens to hundreds of micrometres, implies some hydrodynamic properties of fluids further discussed in this manuscript.

The use of microfluidic devices offer several advantages for analytical and bioanalytical applications, notably the use of minute amounts of reagents and samples (down to picolitres) and an important time reductiondue to the decrease of diffusion distance. In addition the large surface-to-volume ratio offers an intrinsic compatibility between microfluidic systems and surface-based assays. Microfluidic systems also offer strong potential for portability,low cost, versatility in design for integration and multiplexing development.

The field of micro total analysis systems has rapidly expanded and has especially evolved towards bioanalytical and biochemical applications (Figure I.2). A rather wide account, ranging from basic research in academia to commercial applications was presented in a series of review articles by A.Manz group [15], [16], [29–33].

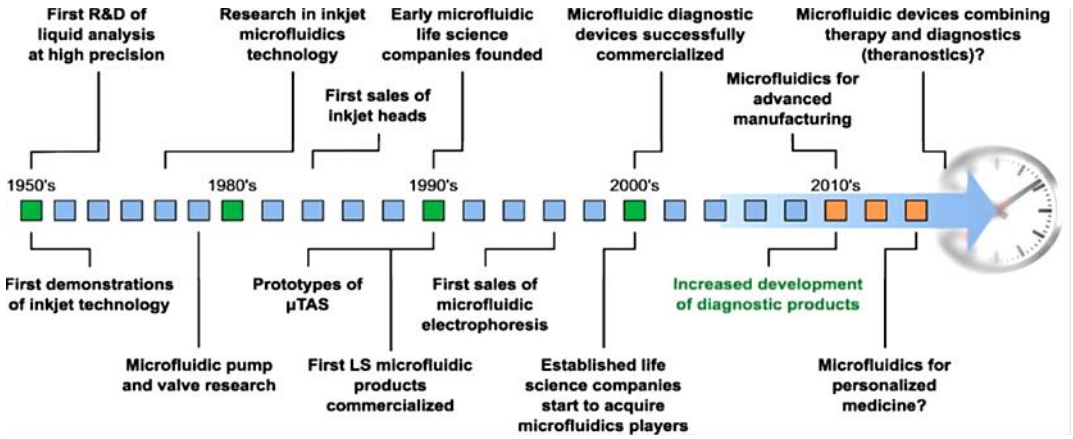

Figure I.2: Timeline of the evolution of microfluidic technology[34].

Progress in the development of bioanalytical microfluidic devices presents particularly interesting features for the development of miniaturized, portable, user friendly and low cost systems called “point-of-care” (POC) systems. A well-known example of lab-on-a-chip is already commercially available on the market: the strip test for pregnancy [35]. In this device, the sample flows across a membrane, which gathers labelling reagents embedded within it, and flows over an area that contains immobilized molecules, the labelled captured analytesform a visible peak. The other major class of POC test is the blood glucose test. The latter is also performed on membranes and uses signal amplification by redox enzyme. The glucose test has improved diabetic patient’s quality of live and reduced risks of over or under dosage. This is by nature a particularly well-fitted application for POC, since the useful sensitivity is within the mM range, i.e. not very challenging, the needed frequency of the testing frequency can be high, typically several tests a day. Many other POC applications,

however, would be more demanding regarding for instance sensitivity, so numerous progress is still needed.

b. The basis physics of microfluidics

In order to better understand the physics at play in our systems, let's briefly introduce the basic fluids properties and the characteristic of dimensional parameters.

i. Reynolds number

At the microscale level, the inertial effects are generally negligible but viscosity and surface tension effects are prevalent. The dimensionless Reynolds number (R_e) gives a measure of the ratio of inertial forces to viscous forces, it is defined for a microchannel with a circular section as:

$$Re = \frac{\rho_f v D_h}{\eta}$$

Equation 1

Where ρ_f is the fluid density ($kg.m^{-3}$), v is the characteristic velocity of the fluid ($m.s^{-1}$), D_h is the hydraulic channel's diameter (m) and η is the dynamic viscosity of the fluid ($Pa.s$). Such a dimensionless number allows to describe the flow regime; laminar or turbulent according to the Reynolds number (R_e)value. We can note that when the characteristic dimension of the channel *d* decreases, the Reynolds number decreases strongly. It is generally smaller than 1 (typically 10^{-2}or10^{-3})at the velocities usually encountered in microfluidics $R_e < 1$ indicates a laminar flow, without any sign of turbulence, while for $Re >> 1$, the flow is considered to be turbulent (Figure I.3).Between $R_e \sim 1$ and $R_e \gg 1$ lies a transition regime, in which turbulence generally does not occur, but inertial effects may be significant.

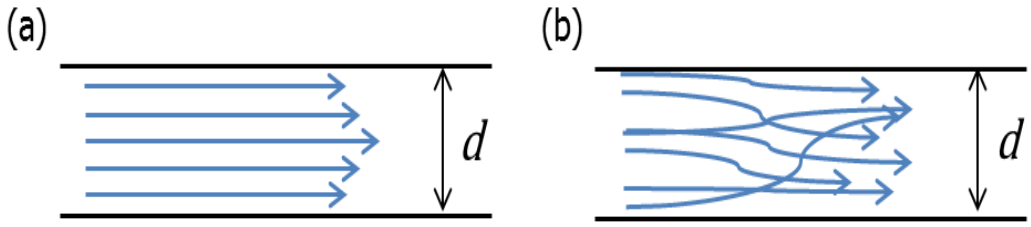

Figure I.3: $\mathcal{R}$e of a fluid flow describes its flow regime (a) Re < 1, laminar and (b) Re >>1, turbulent.

In microchannels the flow is almost exclusively laminar due to their small cross section and even if two or more streams are used, no mixing is observed except by diffusion (Figure I.4) [36].

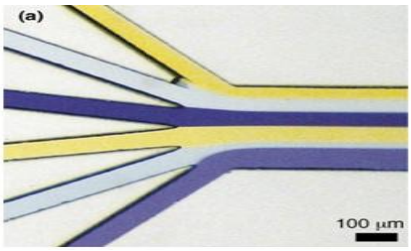

Figure I.4: Side-by-side flowing streams are mixed only by diffusion[37].

ii. Diffusion

In a laminar flow, mixing between several liquids in microdeviceis governed by advection on larger scales, and diffusionacross flow lines on small scales. This involves that transport of mass, energy or momentum in a direction perpendicular to the flow is essentially diffusive. Depending on the applicationthe laminar flow can be desirable or not. With laminar flows, the sorting and analysis of products is in general easier. On the contrary, for some applications notably those requiring a reaction between species initially contained in different fluids or solids, a mixing between the different reagents injected is required.

The relative importance of advectionand diffusion effects is given by the Péclet number:

$$Pe = \frac{v.d}{D}$$

Equation 2

Where v is the velocity (m.s-1), d is a covered distance by the particle during time t (m) and D is the diffusion coefficient of the particle $(m^2.s^{-1})$. Péclet number gives an indication on the diffusion process in microfluidic device. One of the principal applications of diffusive mixing is known as "T-sensor" or "Y-mixer". Two flow fluids are injected to flow alongside each other down the channel, and solute molecules in each stream diffuse into the other one, forming an interdiffusion zone(Figure I.5).

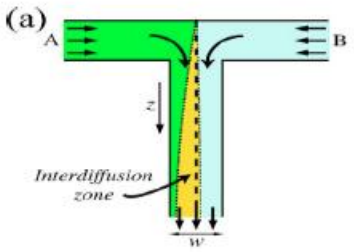

Figure I.5: Schematic representation of the microfluidic T sensor [38].

As the diffusion process is slow, a long channel is required so that an effective mixing can take place, especially to increase the contact area between species to be mixed. In this

aim, several approaches have been considered. They can be characterized as either active, where the sample species is mixed by using an energy input from the exterior, or passive, where particular microchannels configuration increases the contact area between different incoming fluids. Hessel et al. and Lee presented a review on microstructured mixer devices, their mixing principles and their mixing performances[39][40].Table 1and Table 3provide a non-exhaustive list of the different categories available to perform a good mixing in microfluidics.Categories of active microfluidic mixers:

Mixing Technique	Reference
Acoustic / ultrasonic	[41], [42]
Dielectrophoretic	[43]
Electrohydrodynamic force	[44]
Termal actuation	[45]
Electrokinetic instability	[46]
Magneto-hydrodynamic flow	[47]

Table 2: Active micromixers in recent years. (adapted from ref [39]).

For example, Wang et al. presented a numerical simulation of a magnetic micromixer constituted by a microchannel and a pair of electromagnets (Figure I.6). In such a system, mixing is induced by alternating the actuation of suspended magnetic particles in the fluid. Figure shows the performances of this magnetic particle driven micromixer.

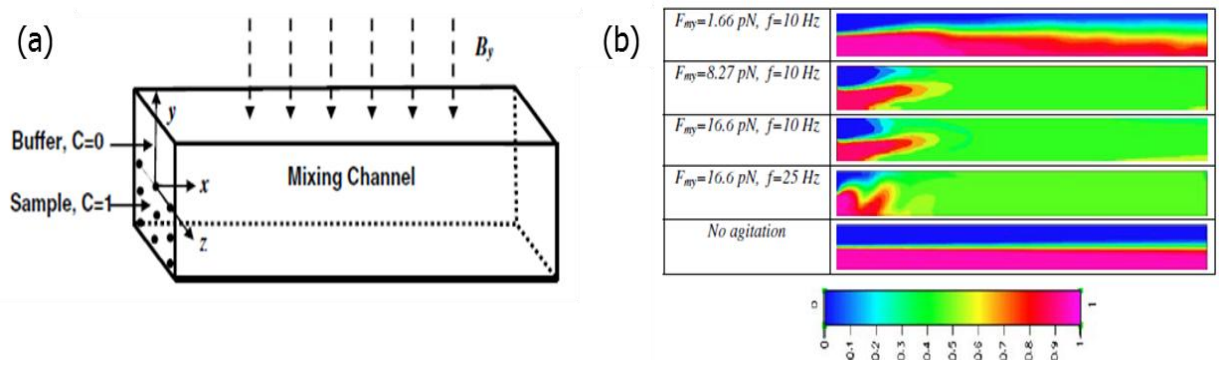

Figure I.6: (a) Mixing microchannel and (b) Concentration contour in the central plane (z = 0) of the magnetic micromixer under different magnetic forces [47].

Categories of passive microfluidic mixers:

Mixing Technique	Reference
Lamination	[48], [49],
Zigzag channels	[50]
3-D serpentine structure	[51–53]
Embedded barriers	[54]
Twisted channels	[55]
Surface-chemistrytechnology (e.g. T-/Y- mixer)	[56]

Table 3: Passive micromixers in recent years (adapted from ref[39]).

Stroock et al. proposed a passive method for mixing streams of stable pressure-driven flows in microchannels at low Reynolds flow. In such mixers, the mixing is due to chaoticadvection thanks to unique channel designs;including bas-relief structures on channel floors (see Figure I.7).

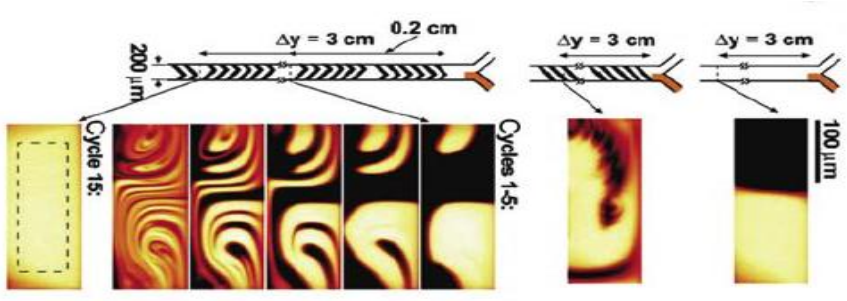

Figure I.7: Schematics of a straight channel with no structure on the walls (top), with straight ridges (middle), and with a staggered herringbone mixer (SHM) (bottom). Confocal micrographs correspond to the vertical cross-sectional views of two fluid stream (one of them contains fluorescent dyes)[51].

Nevertheless, even if the micromixers might exhibit certain advantages and disadvantages as well they offer a high efficient mixing, and now, constitute very useful accessories for different applications in microfluidics.

iii. Flow control

This last decade, many flow control methods have been described in microfluidics. The liquid flow can be controlled using either passive or active pumps. In passive pumping, the forces involved to drive liquids are due to chemical gradients on surfaces, to osmotic pressure, and to permeation through the PDMS or capillary forces.

In active pumping, an external power source is needed; the flow rate can be controlled essentially by electric field, magnetic field or centripetal force, by mechanical displacement(e.g. syringe or peristaltic pump), or by hydrostatic pressure.Until recently, syringe pumps have been the most common in microfluidic laboratories[57], [58].

However, the flow rate range that can be applied limited and it depends on the syringe capacity, so that a compromise must be made between accuracy and capacity. The syringe is connected to the microfluidic chip with tubing connections (device shown in Figure I.8.a), lead to large

dead volumes and significant flow hysteresis. In 2004 a new generation of pressure controller was made available to overcome the defects encountered with the syringe pump (Futterer et al., 2004) and marketed by Fluigent Company®. Further details are given in the MAESFLO controller appendix.

Whatever the type of flow control applied, a pressure-driven flow leads to a parabolic velocity profile. Such flow profile causes an axial dispersion since the fluid velocity is zero at the tube wall and maximum at the centreline, as depicted in the Figure I.8.b with a schematic representation of Poiseuille flow and Taylor dispersion. Due to this phenomenon, the pressure-driven flow is less attractive for separation as it leads mostly to a decrease of separation performance and consequently to a lower resolution.

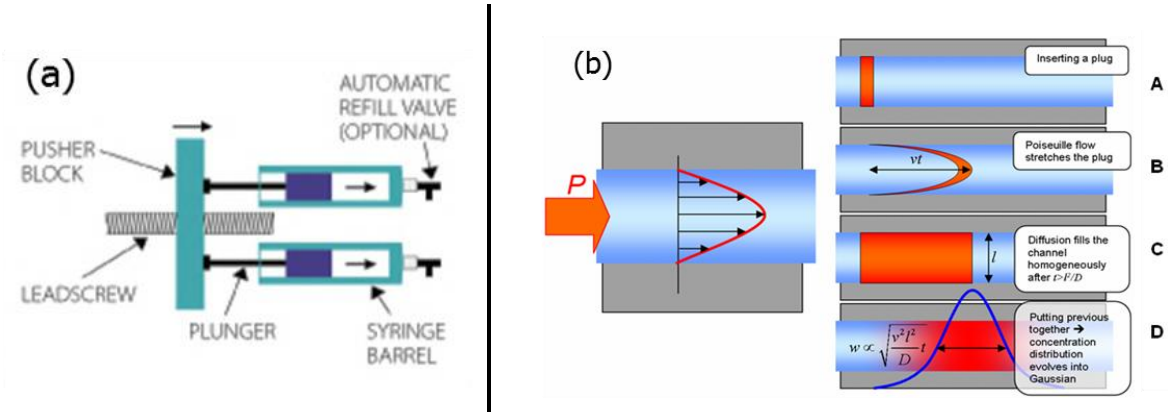

Figure I.8: (a) Schematic drawing of syringe pump. (b) Poiseuille flow and Taylor dispersion [59].

Another approach to control the flow is based on the movement of molecules under an electric field. When a liquid comes into contact with the charged surface of a microchannel, the formation of an interfacial charge causes a rearrangement of the local free ions in the liquid so as to produce a thin region of nonzero net charge density, near the interface. This is the electric double layer (EDL). In presence of an electric field, the solvated ions are driven towards the oppositely charged electrode, and by viscous drag transfer the motion to the rest of the liquid which runs uniformly as a plug-like flow (see Figure I.9)[60][27]. This phenomenon is called electroosmosis, or electroendosmosis. Electroosmotic flow control has been first exploited with glass microchips. But others materials can also generate electroosmotic flow. For instance, the oxidation of PDMS by plasma treatment generates silanol groups (Si-OH) on the surface of the microchannels.

The electroosmotic flow (EOF) creates a uniform flow profile, thus allowing the transport of small volumes of samples while avoiding band broadening in contrast with the hydrodynamic dispersion, in the pressure-driven flow. Nevertheless, the EOF control exhibits important drawbacks for bioassays, including buffer incompatibility i.e. the fluids used in such systems are often so highly conductive that they could generate deleterious Joule heating for assay performance.

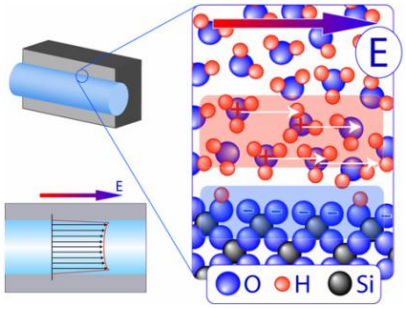

Figure I.9: Electroosmotic flow[59].

2. Lab-on-a-Chip: magnetic microparticles and immunoassays

a. Magnetic microparticles for bioanalysis

i. Magnetic properties

Most commonly magnetic microparticles are composed of an ensemble of magnetic nanocrystals enclosed in a non-magnetic matrix made of an inert and bio-compatible material such as polymer or silicon dioxide. The nanocrystals are usually made of iron oxides such as magnetite (Fe_3O_4) or magnemite (γ-Fe_2O_3), pure metals (amalgams of transition metals) (Ni, Fe, Co, Mg or Zn) or rare earth materials (NdFeB or SmCo)[61], [62]. Iron oxide has a better stability against oxidation than pure iron, and among oxides, maghemite is more stable than magnetite in aqueous media[63].

The origin of magnetic properties arises from the spin and orbital motion of electrons. The orbital motion of electrons around the nucleus produces its own orbital magnetic moment. The spin magnetic moment stems from the rotation of the electron around its own axis (Figure

I.10). Consequently, electron spinning and orbiting, often called spins for brevity, act as tiny current loops[64].

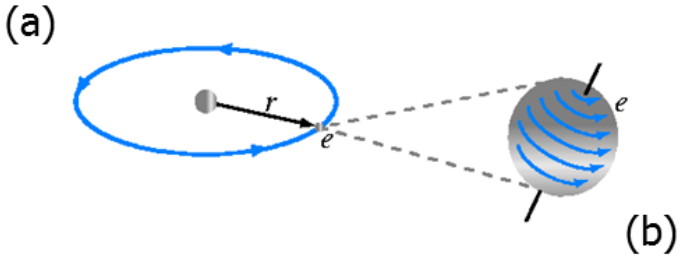

Figure I.10: Motion of an electron around the atomic nucleus. (a) Orbital magnetic moment and (b) spin magnetic moment of an electron.

The electrons can be grouped in parallel or antiparallel pairs. In the latter case, the magnetic moment is cancelled. Under an external magnetic field, magnetic structure of materials gives rise to particular magnetic behaviour according to their magnetic susceptibility, χ and can be classified as *diamagnetic*, *paramagnetic* or *ferromagnetic*. Table 4 summarizes the different types of magnetic materials in an ideal alignment of the electron spins(i.e. temperature of absolute zero, cf.Langevin model and Curie law).

Magnetism Type	Magnetic Susceptibility (χ)	Atomic and Magnetic Behaviour	
Diamagnetism	- small $\chi < 0$ - negative (repulsion) H2O, $(-9.048 \cdot 10^{-6})$ Cu, $(-0.77 \cdot 10^{-6})$	Atoms have no magnetic moment.	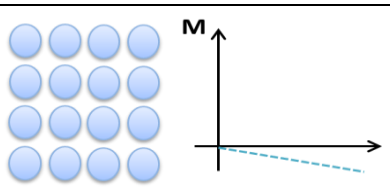
Paramagnetism	- small $\chi > 0$ - positive (attraction) Na, $(-8.6 \cdot 10^{-6})$ Al, $(-2.2 \cdot 10^{-5})$	- Without magnetic field: random orientation of magnetic moments (no-interaction between neighbouring atoms). - In a magnetic field: parallel alignment of magnetic moments.	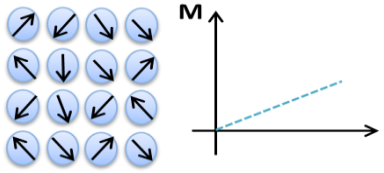
ferromagnetism	- large $\chi \gg 1$ - positive (attraction) - function of applied field Fe, (1000)	Atoms have parallel aligned magnetic moments within domains.	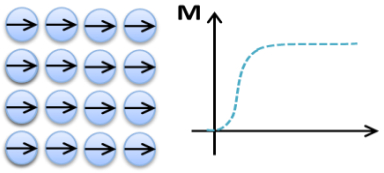

Table 4: Comparison of the three most important types of magnetism.

In *diamagnetic* material, all the electrons are paired so there is no permanent net magnetic moment. However,a weak negative magnetization is produced under a magnetic field. Most materials as water, proteins, polymers are weakly diamagnetic. These are often called non-magnetic [65].

Paramagnetism is due to the cooperative behaviour of orbiting electrons. Some of the atoms or ions in the material have a net magnetic moment. In the presence of a magnetic field, the atomic magnetic moments are partially aligned in the direction of the field, resulting in a net positive magnetization and a positive susceptibility. These materials are slightly attracted towards zones of higher magnetic field, but do not retain their magnetic properties when the external field is removed. Oxygen, ionic solutions and aluminium belong to this category. On the contrary, a large net magnetization is observed in ferromagnetic material, even in the absence of an external magnetic field. At temperature of absolute zero, magnetic moments are aligned parallel and are oriented in the same direction. Nevertheless, above a critical temperature, known as Curie temperatureT_c, azero magnetization is observed due to the large thermal fluctuations which completely disorient and randomize the spins orientation. Iron, Nickel and Cobalt are examples of ferromagnetic materials.

In*ferromagnetic* materials, the atomic magnetic moments are aligned in thesame direction within magnetic *Weiss domain.* The latter is a region in which the direction of magnetization is uniform [66].The transition between two domains, where the magnetization flips (i.e. gradually changes), is called a *Bloch domain wall* (see Figure I.11)[67]. The presence of magnetic domains minimizes the magnetostatic energy of the system and prevents the spontaneous magnetization of ferromagnetic materials. This state is called the *multi-domain* state. In a strong magnetic field, the magnetization of the material reaches a saturation levelat which all domains flip their polarization orientation parallel to the external field, until reaching full magnetization i.e. forming a single domain.

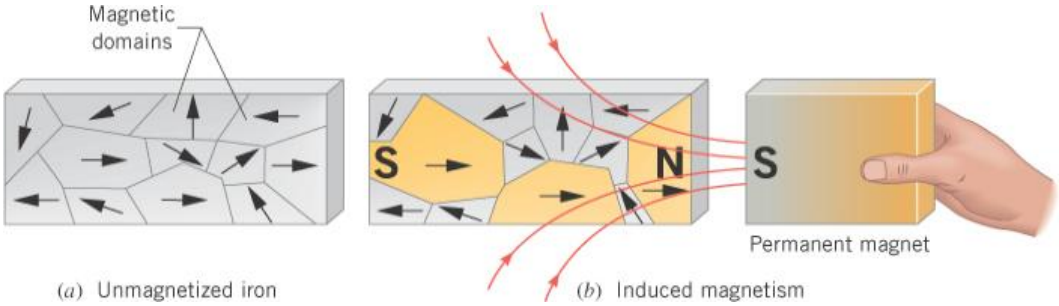

Figure I.11: Illustrations of multi-domain state: (a) without any external magnetic field, domains are misaligned (magnetic domain sizes are ~ 0.01 - 0.1 mm). (b) In a magnetic field, aligned domains make material highly magnetic [68].

If an object is placed in a magnetic field strength$\vec{H}$, it responds by producing a magnetic field, the magnetization$\vec{M}$**.** The magnetic flux density$\vec{B}$ is increased by the magnetization$\vec{M}$ of the material and is defined as:

$$\vec{B} = \mu_0 \left(\vec{H} + \vec{M}\right)$$

Equation 3

Where μ_0 is the vacuum permeability, given by $\mu_0 = 4\pi \cdot 10^{-7}\ N/A^{-2}$. The magnetization is given by$\vec{M} = \vec{\mathrm{m}}/V_p$, i.e. the magnetic moment $\vec{m}$ per volume unit V_p. The magnetic character of a material is represented by relative susceptibility χ_r. The relation between $\vec{M}$ and $\vec{H}$is often expressedfor diamagnetic and paramagnetic materials by:

$$\vec{M} = \chi_\mathrm{r}\, \vec{H}$$

Equation 4

Combination with equation (1) and (2) results in

$$\vec{B} = \mu_0(1 + \chi_\mathrm{r})\vec{H} = \mu_0\mu_\mathrm{r}\, \vec{H}$$

Equation 5

with μ_r, the relative magnetic permeability. The dimensionless parameter μ_r is dependent upon the applied external magnetic field $\vec{H}$ and the temperature T according to laws depending on the type of magnetism [64], [66].

In ferromagnetic materials, the presence of domains leads to a non-linear magnetization behaviour, known as magnetic hysteresis loop. In its demagnetized state, the magnetization vector in domains has different orientation, and the total magnetization average zero.Such materials, however, are able to retain their magnetic properties after an external field has been applied and then removed (the domain walls are not fully reversed to their original position). An example of a magnetization curve is shown in Figure I.12. In this figure, a hysteresis loop is defined by the saturation magnetization M_s(point a and d), the coercive field H_c (point c and f) and the remanent magnetization M_r(point b and e). The saturation magnetization is the maximum magnetization induced in the presence of an external magnetic field. When the magnetic field is switched off, the magnetization does not go to zero and a remanent magnetization M_r is observed. The coercive field H_c is the field necessary to cancel the magnetization of the material.The response of a ferromagnetic material can be described by the parametersM_s, $M_r$and H_c.

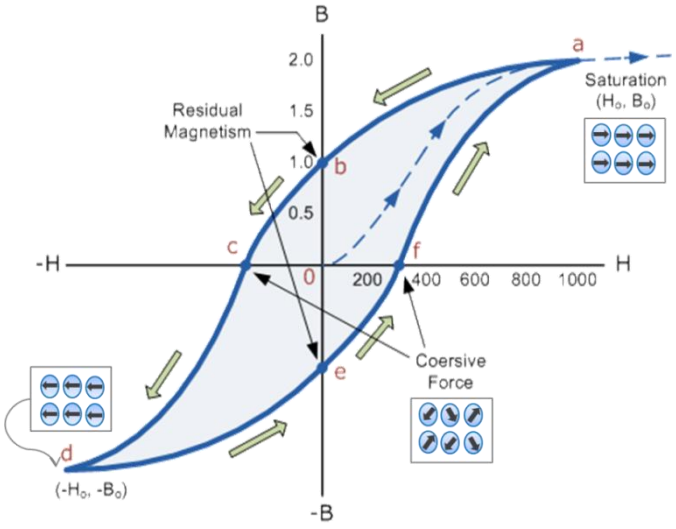

Figure I.12: Hysteresis Loop depicts relation between magnetic flux density and magnetizing force. The dashed line represents the starting magnetization of the material. (i.e. unmagnetised). The full line shows the magnetization loop (adapted fromref [69]).

ii. Superparamagnetic microparticles

As mentioned above, magnetic domains exist because they minimize the magnetostatic energy of the system. In large particles of the order of micrometre or more, the formation of domain walls is favoured and results in a multi-domain structure of the particle even with a small magnetic field, which explains the relatively low coercive files (Figure I.14) [70], [71]. If the particle size decreases down to a critical particle diameter d_c, the formation of domain walls becomes energetically unfavourable, thus the system remains in a single

domain state.In such case, any change of magnetization needs generally a large magnetic energy). As the particle size decreases below the single domain value d_s, ,the thermal energy ($E_T = K_B.T$) becomes of the same order as the magnetic energy barrier($\Delta E = K_{eff}.\frac{4}{3}.\pi.r_p^3$) Therefore, the spin of the particle is free to fluctuate in response to the thermal energy i.e. the particle magnetic moment can jump between two different stable orientations with a frequency higher than the experimental time scale (see Figure I.13).

The relaxation time of the particle magnetic moment is given by Néel-Arrhenius equation:

$$\tau = \tau_0 \, exp\left(\frac{K_{eff}.V_p}{K_B.T}\right)$$

Equation 6

$-$ K_{eff} is the particle's anisotropy energy density and V_p its volume. Then, $K_{eff}.V_p$ is the energy barrier associated with the magnetisation moving from its initial axis direction to another one.

$-$ $\tau_0$is the length of time characteristic of the material (typically $10^{-9}10^{-10}s$)

$-$ τ is thus the average length of time that it takes for the particle magnetisation to randomly flip as a result of thermal fluctuations.

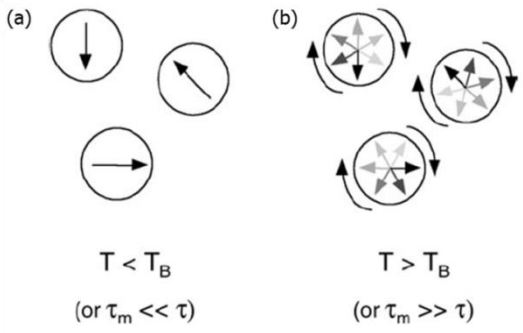

Figure I.13: Illustration of the concept of superparamagnetism. Three magnetic nanoparticles and the arrows represent the net magnetization direction in those particles in two different cases (a) and (b)[72].

The time-averaged magnetization without external magnetic field is zero. Without an external magnetic field the magnetic moments of the iron oxide nanocrystals are randomly oriented. Conversely, if an external field large enough to overcome the thermal energy is applied along an axis, the particle will be magnetized in that direction. When the field is switched off, the particle returns to its initial state Figure I.14.a without keeping any remanence as paramagnetic material. At the scale of the order of ten nanometres or less, the coercive field is mainly equal to zero ($H_c = 0$), leading to an anhysteretic, but still sigmoidal curve. A schematic hysteresis free magnetization curve is shown in Figure I.14.b. Such behaviour, related to the nanosize structure of the particles is termed as superparamagnetic**.**

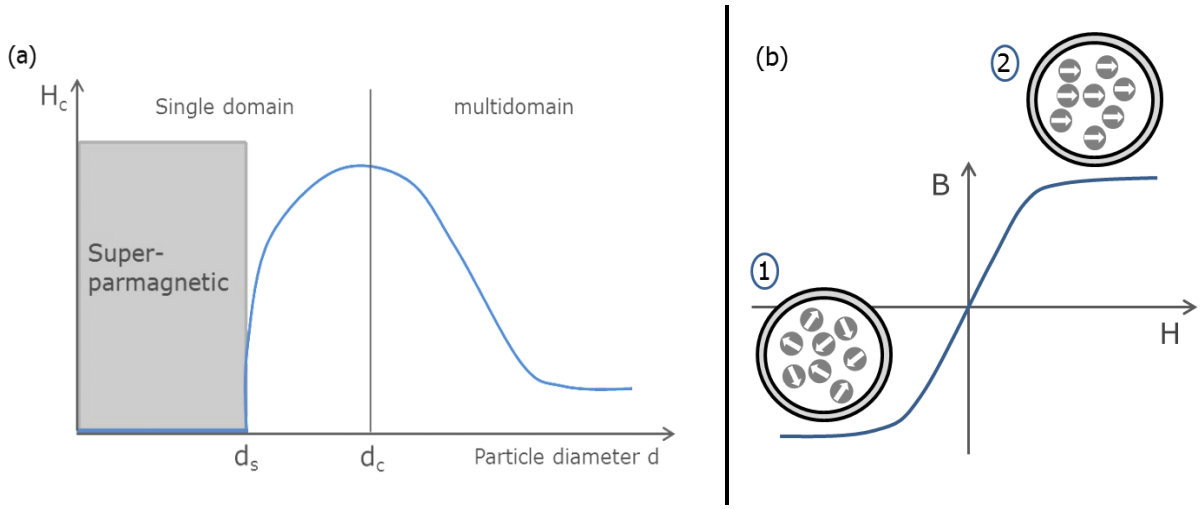

Figure I.14: (a) Illustration of the variation of coercivity as a function of particle size. Below ds, the coercive field of particles is Zero ($d_s = 18\ nm$ for maghemite). (b) Magnetization curve of superparamagnetic particles, no hysteresis. 1) Random orientation of the nanoparticle moments. 2) The nanoparticle moments aligned in a direction of the magnetic field (adapted from[73]).

iii. Structure of microparticles

A superparamagnetic microparticle is synthetized with an ensemble of superparamagnetic nanoparticles (core) encapsulated in a polymer shell. Using a polymer shell protects the magnetic core against environmental influence and allows a wide choice of surface coatings, including the incorporation of fluorescent dyes and bio-molecules such as streptavidin, nucleic acids or specific antibodies [74]. Figure I.15shows two classical structures used to prepare superparamagnetic spheres.

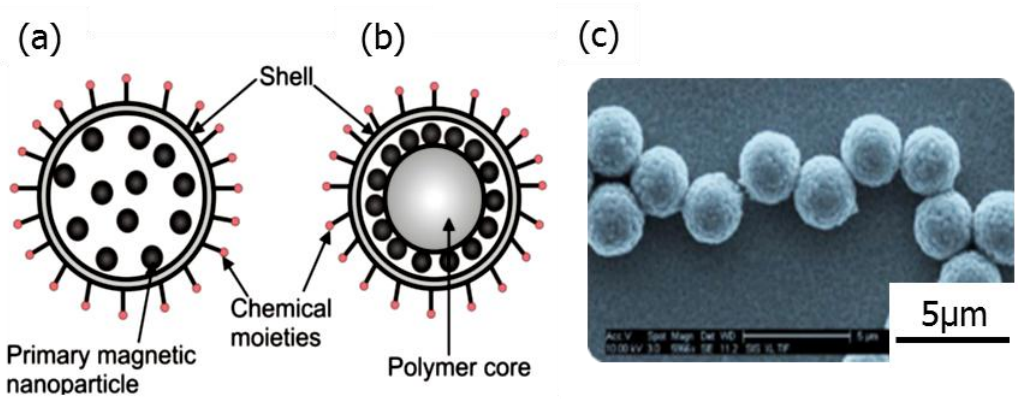

Figure I.15: (a) and (b) Structure and configuration of superpararmagnetic particles. (c) SEM-picture of the magnetic microspheres (ϕ 2.8 μm Dynabeads®).

Because of the weak interaction between the nanoparticles, the overall magnetic moment $\vec{m}$ of a microparticle is usually given by the sum of the moments of the individual magnetic moments of the nanocrystals enclosed in the polymer shell. For that reason, the inner morphology of the particle, i.e. the size and the amount of the encapsulated magnetic crystallites, influences the overall magnetic behaviour. Finally, the choice of the microparticles is strongly dependent on the targeted application. Indeed, the particle size is a critical parameter. Its decrease leads to

an increased surface-to-volume ratio, thus to a larger specific surface area. Nevertheless, the magnetic moment is reduced, giving rise to a low magnetic force. In summary, the choice of the optimal particle size for a give application requires an optimization combining magnetic and biological properties. Superparamagnetic particles used in biological or medical applications typically range from 50 nm (Miltenyi) to 5 μm (Dynal).

b. Immunoassay principle

An immunoassay is a biochemical method dedicated to the detection and quantification of biomolecule targets in various samples, for instance biological fluids (blood, serum or urine). This method is based on the specific binding of an antibody (Ab) and an antigen (Ag). The Ab-Ag complex is known as immuno-complex. The high affinity and specificity of Ab-Ag interaction enable an antibody, to bind only its specific target, even in the presence of many other biomolecules.

$$Ab + Ag \leftrightarrow Ab - Ag\ (immuno - complex)$$

The first reported immunoassay was developed by Yalow and Berson in 1960 to detect and quantify insulin in blood [75]. This work opened up many others opportunities for immunoassays. Since then, immunoassays are commonly used in drug analysis, clinical diagnostic, and food quality testing, environmental monitoring…etc.

Immunoassays can be classified as a function of various parameters such as:

- Homogeneous/heterogeneous
- Competitive/non-competitive
- Label/label-free
- Direct/indirect

The present work deals with magnetic beads-based immunoassay, i.e. a heterogeneous immunoassay. Homogeneous immunoassay

Homogeneous immunoassays are based on the formation of immuno-complex in solution. In case of homogeneous immunoassay, the detection relies on the physical and chemical changes of the bound and unbound antibodies during the assay. Changes can be discriminated for instance by the differences in diffusion properties [38], [76], isoelectric point [77], enzyme activity [78] or fluorescence by Fluorescence Energy Transfer (FRET). Such immunoassay requires less manipulation steps as the antibodies (Abs) immobilization and rinsing steps are not necessary. In absence of any immunosupport, such immunoassay allows to drastically reduce non-specific binding.However, the performance of the immunoassay is mainly limited by lower selectivity and limits of detection. At microfluidic scale, most of homogeneous immunoassays have been performed by microchip

electrophoresis. Indeed, free and complex forms can be separated as a function of their electrokinetic mobility, size or isoelectric point[79].

One of the most common homogeneous assays is the latex agglutination test (LAT). The test was introduced by Singer and Plotzin 1950s [80]. During an agglutination assay, the sample is mixed with colloidal particles (e.g. latex particles) functionalized with capture antibodies. In presence of target Ag, a sandwich-like structure (Ab-Ag-Ab) isproduced as shown inFigure I.16. The aggregates concentration is proportional to the concentration of the target Ag. The detection of particles agglutination may be performed by optical methods, in particular by turbidimetry (measure of transmitted light) or nephelometry (measure base on scattered light)[81]. For example, a recent agglutination test, in a microchip, using a particles actuation conceived by Gijs et al. is described below [82].

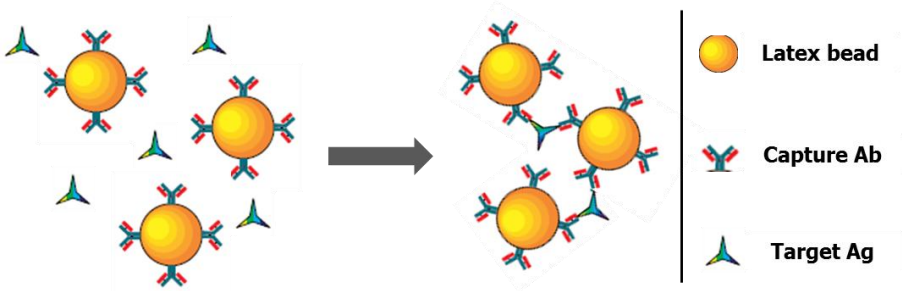

Figure I.16: Schematic illustration of a latex agglutination (LAT). The target antigen (Ag) contained in the sample, binds to capture antibody (Ab) at the surface of latex particles (adapted from ref [83]).

Latex immuno-agglutination assays are simple, cheap and quick to perform. Itrepresents an alternativetoenzyme linked immunosorbent assay (ELISA) which have been reported at the same period [80]. These types of assay are mainly used for infectious diseases and protein quantification. However, their major disadvantage is the lower detection limit as compared to conventional ELISA i.e. 1nM compared to 1pM, respectively [84], [85].

i. Heterogeneous immunoassay

During heterogeneous immunoassay, immunoreactions occur on a solid surface. Thisallows easy analyte preconcentration, washing and consequently a lower limit of detection (LOD). In addition, this approach can be automated in 96-well microplates, allowing easy separation of the immune complex and free forms, and high-throughput analysis. To obtain a high sensitivity, the detection step can be based either on fluorescent or radioactive molecules or a product of enzymatic reaction. Among heterogeneous immunoassays, ELISA is one of the most widely used in clinical diagnosis. When performing an ELISA, the immunoassay starts with the introduction and immobilization of capture Ab (or Ag) on a solid support. The simplest form of immobilization is a physical adsorption of antibody or antigen onto the surface [86–88].After blocking and washing steps, a sample containing an unknown amount of antigen (or Ab) is introduced to interact with the capture

Ab (Ag). In case of sandwich ELISA, a secondary Ab is incubated, this Ab being conjugated with an enzyme (e.g. Phosphatase alkaline or Horse radish Peroxydase) whereas it is labelled by a radioisotope (^{125}I or ^{14}C) in case of radioimmunoassay (RIA). The main limitation of this format is its lesser kinetic efficiency: It relies on the diffusion of a single partnertowards a solid surface on which all of its reaction partners are immobilized. This, leads to a low rate of immunological capture and long analysis times, because the typical diffusion distance is given by the average distance between particles (proportional to the inverse of the 24 number concentration of PARTICLES to the power 1/3), whereas in homogeneous immunoassays, it is proportional to the inverse of the number concentration of MOLECULES to the power 1/3.ELISA techniques can be broadly classified as *competitive* or *non-competitive*.

In a *competitive* assay, the sample is incubated in presence of a given amount of labelled Ag (see Figure I.17). The target antigens present in the sample will thus compete with labelled Ag to interact with the capture Ab. Thesignal intensity allows to estimate the amount of the labelled antigens bound during the test and consequently the amount of target. As a result, a high signal indicates a low concentration of target antigen in the sample and vice-versa. Thus, response is inversely proportional to the amount of label[89].

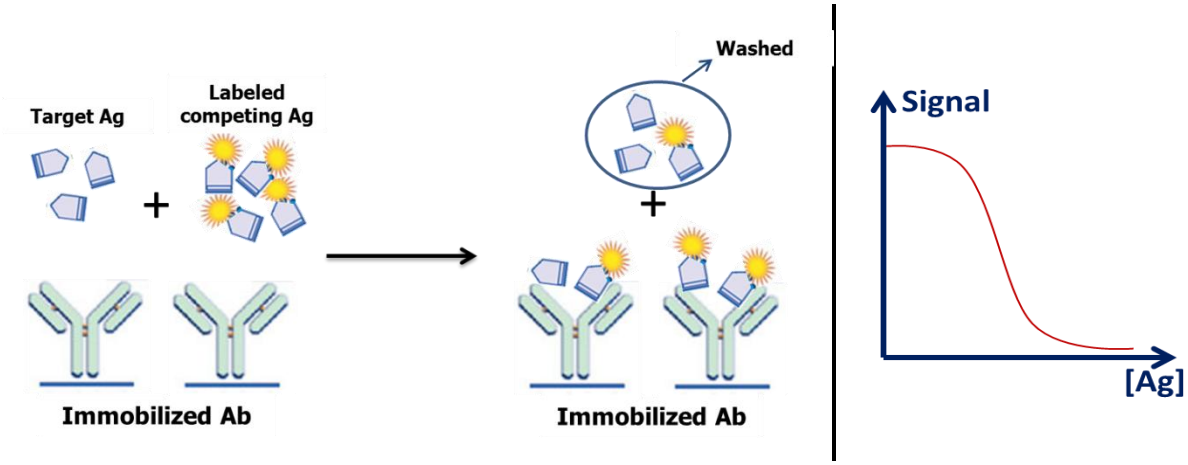

Figure I.17: Schematic illustration of competitive immunoassay.

One disadvantage of competitive assays resides in the fact that the immunoreactivity of the primary Ab is affected by the labelling Ag. The strategy, to overcome this problem, was developed by Miles and Hales and focuses on the labelling of antibody rather than on antigen [90]. Competitive immunoassay also has a limited dynamic range, since it is a difference assay. In *non-competitive heterogeneous* immunoassay, antigens in the sample are captured by the capture immobilizedAbon the solid phase and thereafter detected by using a secondary labelled detection antibody (Figure I.18). The amount of the secondary antibody on the binding sites is directly proportional to the antigen concentration. The limit of detection of non-competitive immunoassay is lower than that of a competitive assay, and its dynamic range is in general higher. As a drawback, it is more sensitive to non-specific binding effects. .

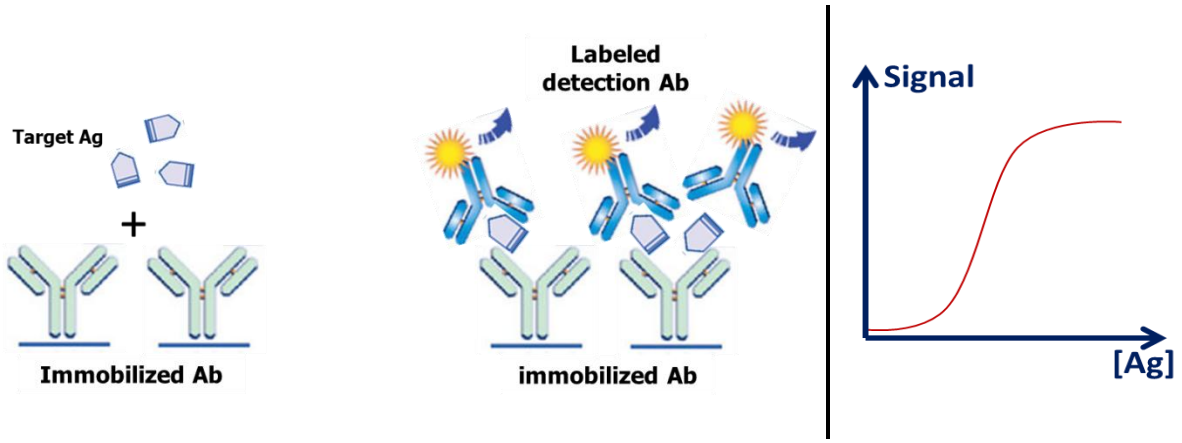

Figure I.18: Principle of non-competitive immunoassay.

The main advantage of an ELISA is related the catalytic transformation of a specific substrate in a detectable product through the enzyme conjugated to secondary Ab, yielding to amplification, i.e. a number of observable products much larger than the number of antigens to detect.In short, Figure I.19 shows some of the different possible configurations used in standard ELISA (i.e. direct or indirect ELISA).Besides, enzymatic amplification, others labelscan be used especially fluorescent dyes or gold nanoparticles. For instance, lateral flow immunoassays integrate gold nanoparticles as label to allow a visual detection. Well-known examples of lateral flow tests are home pregnancy tests. Recently, magnetic beads have also been used as labels and can be detected by optical and/or magnetic sensors [91].

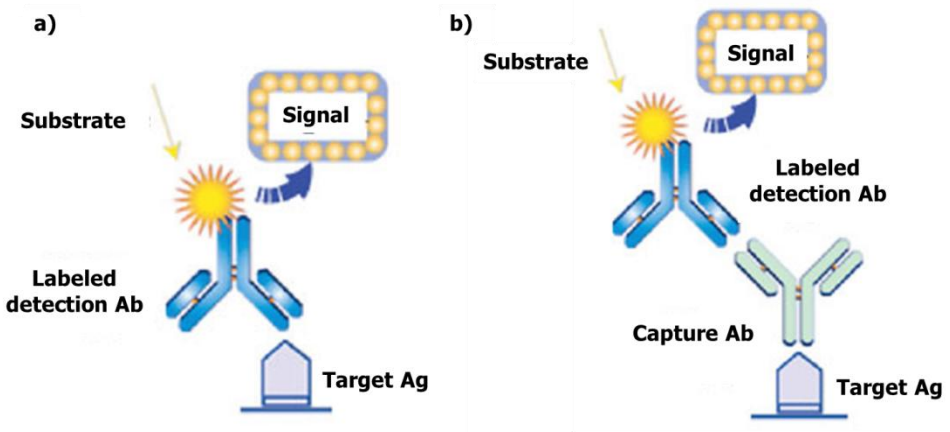

Figure I.19: Illustration of two different types of ELISA: (a) Direct ELISA, (b) Indirect ELISA (adapted from ref [92])

Heterogeneous and in particular ELISA are usually performed on conventional microtiter plates in spite of long incubation times(Here, the relevant diffusion time is the i.e. time needed to cross by diffusion the solution from the surface to the bottom of the well, i.e. a distance in the mm range. These incubation times can be shortened by minimizing the diffusion distance. For this reason, immunoassays have been implemented in microfluidic systems and new dispersed (colloidal) solid phases were explored to immobilize antibody and consequently increase the performance of immunoassays especially in terms of throughput of analysis [93].

Besides, the transposition of bioassays at microfluidic scale offers many advantages compared to conventional methods [94]:

- Increased surface-area-to-volume ratio speeds up reaction kinetics,
- Smaller dimensions reduce the consumption of expensive reagents and precious samples.
- Automated liquid-handling can improve throughput and help to minimize variability of immunoassay test.

These main advantages can potentially improve the performance and reduce costs and analysis time.

In parallel, nanoparticles and microparticles are used as immunosupport to perform immunoassay. It has been demonstrated that decreasing the immunosupport size allows to enhance the surface to volume ratio and consequently to improve the immunoassay kinetics[95]. Besides, such particlesare easily manipulated by different methods, e.g. magnetic or centrifugation. It should be mentioned that most particles integrated in microfluidic immunoassays are magnetic.

In the following section, the different methods dedicated to the manipulation of the particles in a fluid are briefly described. The purpose of this section is to give an overview of the implemented forces in these methods. Among them, however, we onlyused the magnetic forces.

3. Technical aspects of microparticles manipulation

a. On-chip microparticles manipulation

As previously mentioned, microparticles are often used as immunosupport to improve immunoassay performance. These particles exhibit different properties, in particular they can be either magnetic or non-magnetic. The method used for beads manipulation mainly dependson the beads properties.

i. Chemical and mechanical trapping of microparticles

Beads immobilization based on chemical interaction

When dealing with non-magnetic beads, several techniques have been developed to arrange beads in specific area of a chip according to their surface functionalization. The method proposed by Andersson,is based on the formation of a dot array of self-assembled beads. It relies on microcontact printing to generate patterns with desired functions (seeFigure I.20.a)[96]. Using a structured stamp, streptavidin coated-beads are assembled on the surface through the strong interaction with biotin printed on the surface (Figure I.20.b and c.). In

addition, a hydrophobic Teflon-like film (C_4F_8) defined by lithography, separates dots so as to prevent cross-contamination of liquid from each other (Figure I.20.a).

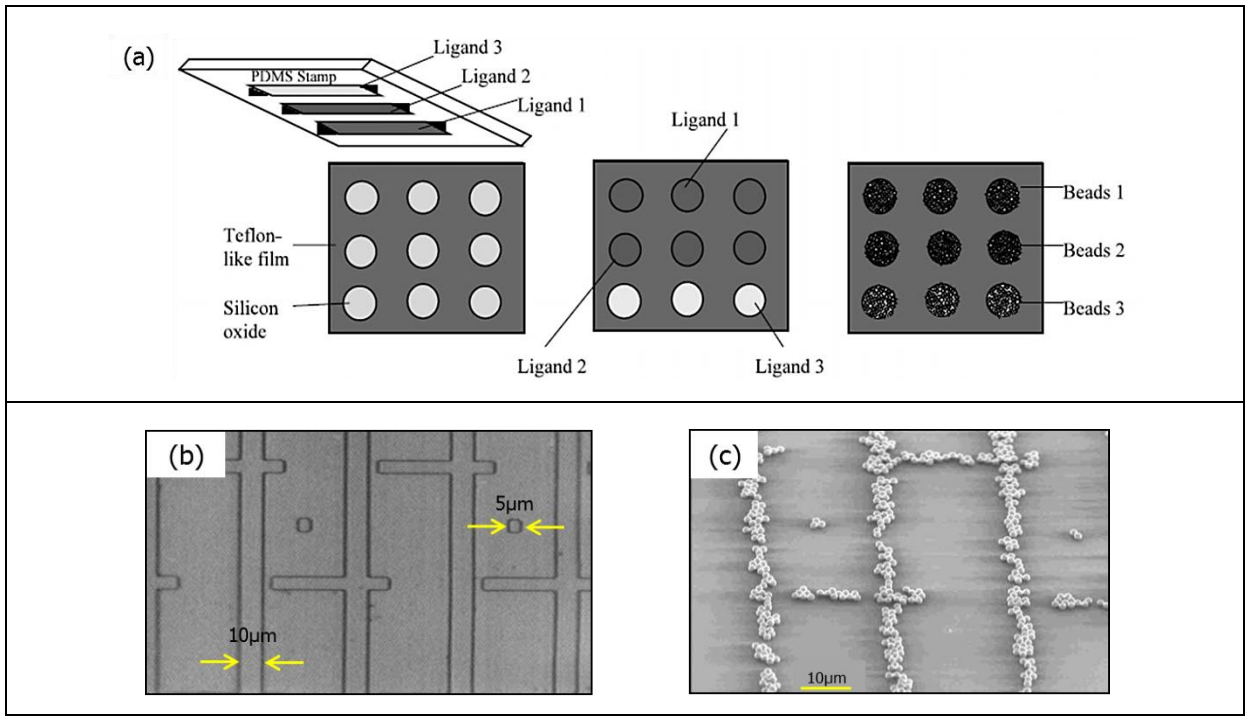

Figure I.20: (a) Conceptual depicting of the different steps involved in generating the dot array. (b) Structured stamp with features as small as 5µm is shown. (c) SEM image of the immobilized streptavidin coated-beads into a high-resolution pattern (adapted from ref [96]).

Although this technique allows an acute and efficient microparticles trapping, the main advantage of using microparticles i.e. reduces diffusion distance, is lost since the particles are immobilized on a surface, and analytes have to diffuse from the bulk of the fluid to this surface.

Mechanical trapping

In the early development of microfluidic-based immunoassay, numerous strategies have been proposed to physically retain non-magnetic beads. The main purpose is to get a physical retention of beads in order to allow the integration of all the immunoassay steps in particular the washing steps. To do it, the particles are trapped mechanically with dedicated microstructures. A chromatographic bed was fabricated on a glass substrate as part of an electroosmotically pumped microfluidic system realized by Oleschuk et al.[97]. Silanized silica beads were trapped in a cavity formed by two weirs within a simple channel and this packed-bed was used as an integrated solid-phase extraction (Figure I.21.a). Sato et al. developed an immunosorbent integrated into a glass microchip dedicated to immunoassay [98]. Polystyrene particles are immobilized within a microchannel because of a height restriction of the channel Figure I.21.b. The beads surface coated with human secretory immunoglobulin A (S-IgA) reacts with colloidal gold conjugated anti-S-IgA antibody and detected by thermal lens microscopy.

The physical retention required more specific microfabrication and do not allow the use of microparticles smaller than the restriction within channel. To overcome this limitation, Baba et al. proposed an original approach based on the trapping of antibody coated beads within a 3D photopolymerized gel [99]. The pillars are photopatterned within the microchannel and three different kinds of coated beads are mixed within one post. Each antibody is tagged with a different dye Figure I.21.c. Four to five colours may be resolved using a conventional fluorescence microscope.Again, however, in this system the characteristic diffusion distance that controls reaction kinetics is the size of the whole plug, and not the distance between particles. Relatively slow kinetics are thus expected, as compared e.g. to conventional colloid based immunoassays in the liquid state.

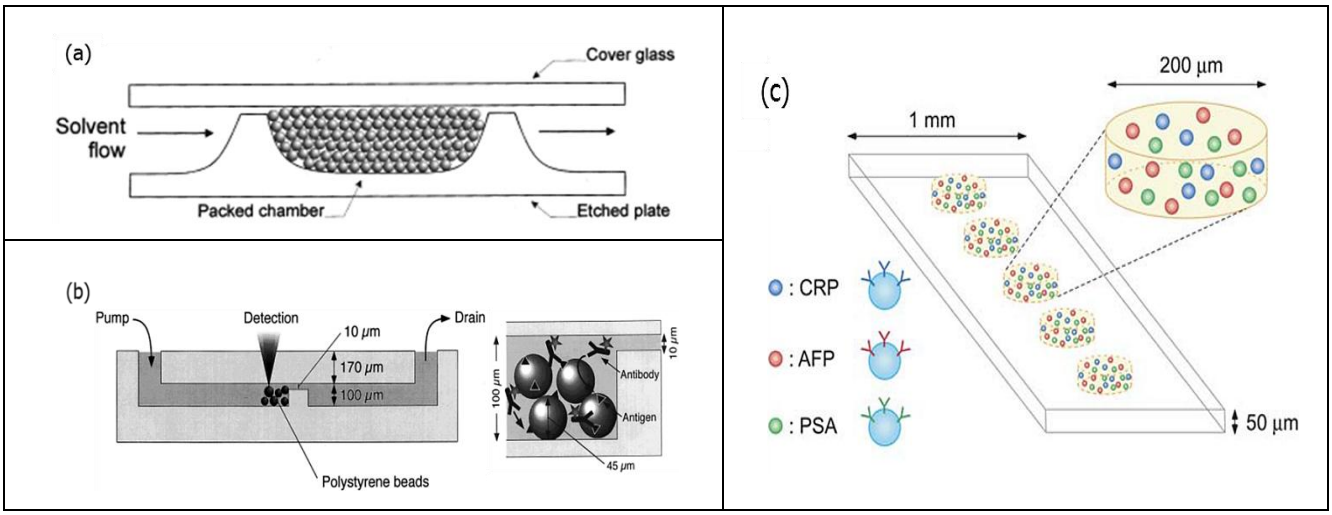

Figure I.21: (a) Schematic illustration of cross-section of packed chamber, showing the physical retention of the microbeads (adapted fromref [97]).(b) Cross-section of and schematic representation of the antigen-antibody reaction adapted from ref [98]). (c) Cross-section, depicting the immuno-pillar chip for triplex assay (adapted from ref [99]).

ii. Dynamic manipulation of microparticles

Optical tweezers

Besides these conventional approaches of mechanical trapping, more sophisticated methods have recently emerged. Among them, optical tweezersuse light to manipulate very finely microscopic objects. The radiation pressure from a focused laser beam is able to attract and hold small particles into the spot centre [100][101]. A spontaneous assembly of 1.1 µm particles in a ring formation with the use of a single-beam optical tweezers was reported by Haldar et al. [102], as shown in Figure I.22.This method does not seem adapted to develop beads-based heterogeneous immunoassay, since the immobilization of high number of beads should be difficult. Besides, optical tweezers are rather expensive systems, and multi-trap ones, in particular, require high power and high quality lasers.

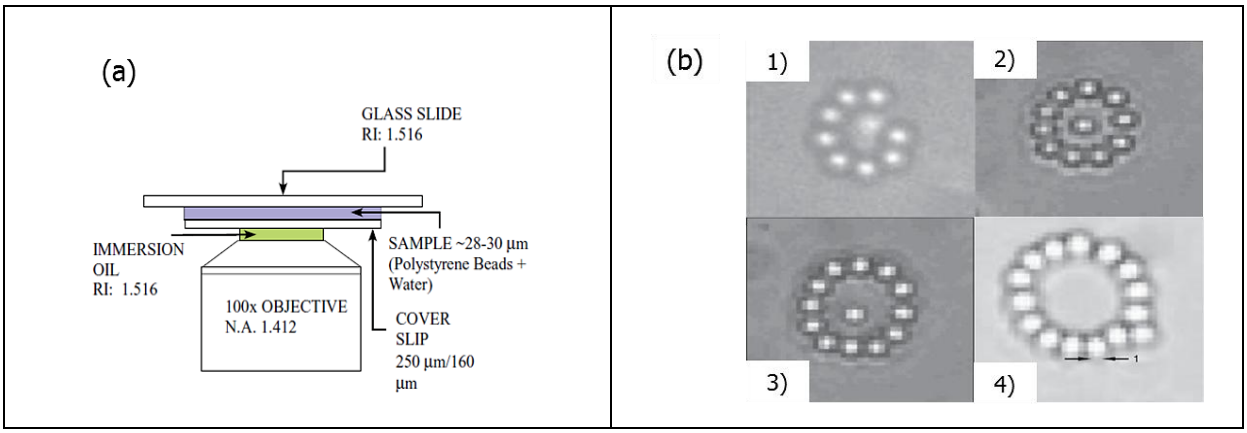

Figure I.22: (a) Illustration of the experimental setup with the sample chamber. (b) Pictures of ring-like structures of particles with (1) 8, (2) 10, (3) 12, and (4) 14 particles forming the ring (adapted from [102]).

Acoustic waves

Another strategy based on acoustic wave has been developed to immobilize microparticles in microdevice. An acoustic standing wave (ASW) builtfrom two radiations contributionsexerts forces on microparticle [103]. Using this method, Hertz et al. demonstrated the trapping of micrometre-sized beads[104]. More recently, they demonstrated the use of ultrasonic standing-wave (USW) techniques to improve the performance of latex agglutination test (LATs) because such techniques increase the interaction between particles and therefore the sensitivity of the test [105]. In continuous-flow microfluidic systems, acoustic radiation can be also used for separation, sorting and alignment. Particles alignment in continuous-flow system was demonstrated by Johanson et al.[106]. A bulk transducer and a resonance cavity are combined to generate the waves. In such system, the primary force is proportional to the acoustic frequency and to the particles volume. A pair of interdigital transducer (IDT), symmetrically arranged on opposite sides of PDMS microchannel, generate constructive interference of the surface acoustic waves, resulting in the formation of standing waves in the fluid. The latter associated with an acoustic radiation pressure act to focus particles within the channel toward node or antinodes of the standing waves, as depicted in Figure I.23.

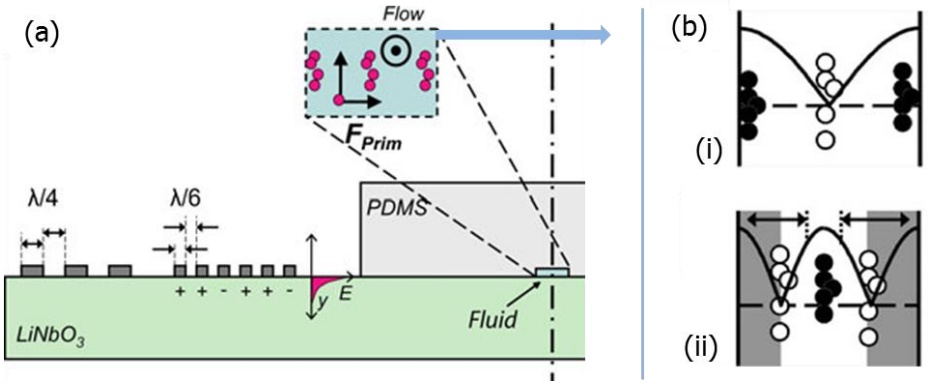

Figure I.23: (a) Cross-sectional view of the principal setup of the interdigital transducers (IDT) on the piezoelectric substrate with (λ/6), the reflector strips and (λ/4), the IDF strips. (b) Schematic representation of the

alignment of negative-θ particles (dark). (i) Alignment at the channel walls with risk of particle stick on surface and (ii) specific frequency (2/2λ), to prevent the particles sticking with the channel walls (adapted from ref [106]).

Dielectrophoresis

When a particle is subjected to a non-uniform electric field, polarized charges are induced on its surface, and form an electric dipole. The polarization of particles depends on their dielectric properties and the suspending medium. The dielectrophoretic (DEP) forces depend also on the frequency, phase and magnitude of the electric field. Polh was one of the first to explore application of the dielectrophoretic force for manipulating particles[107]. More recently, Tornay et al. established a concept where the particles can be continuously functionalized on-chip by the flow, using DEP[108]. A competitive immunosensingfor a rapid manipulation of microparticles based on negative dielectrophoresis (n-DEP) was demonstrated by Ramón-Azcón et al. [109]. In this work, the particles, via the n-DEP manipulation, are captured on the surface by the immunoreaction the assay could be then performed using fluorescent signal emitted by captured particles.

Magnetophoresis

Magnetophoresis is the motion of the particles in a liquid, induced by an inhomogeneous magnetic field. Magnetic particles and their handling are steadily gaining interest.This has lead in recent years, different approaches to incorporate magnetic structures in the microfluidic systems, Lab-on-a-Chip (LOC). This interest is mainly due to the large specific surface of the particles for chemical binding and also to the possibility of exerting relatively large force with low-cost magnets, and without significant Joule heating. In addition, the implementation of actuators such as permanent magnets is simple to integrate to the microchip. For all this reasons, magnetophoresis offers probably one of the most versatile methods for the manipulation of the particles in microfluidic systems. Magnetophoresis is one of fundamental principle used in this work and prior to discussion of our results, I will present in the following section some methods taking benefit of different physical principles for the magnetic manipulation of microparticles.

b. Magnetic microparticles concept for bioassays

Magnetic fields offer appealing tools to handle magnetic objects [110], [111]. Furthermore, in the last few years, functional magnetic nanoparticles and microparticles presenting a wide range of functionality have become off-the-shelf products [112], [113]. Therefore, magnetism has been naturally combined with microfluidics, offering the possibility to adapt bioassays on the surface of magnetic beads, trapped inside a microchannel. However, the exposure of the functionalized beads surface to a microfluidic flow for antigen capture has important consequences on the bioanalysis sensitivity [63], [65]. This is the reason why several strategies have been developed to improve the manipulation of magnetic beads using

actuators. Herein, we present some of them, classified into two types: those using electromagnets, and those using permanent magnets.

i. System using electromagnets

The group of C.HAhn pioneered the use of microelectromagnets for the separation of magnetic beads [114–116]. In such integrated magnetic beads sorters, particles may be manipulated on the length scale of the microfluidic circuit following their distinct magnetic properties. Such devices can be used, for example, in miniaturized cell sorting or in a miniaturized bio-reaction system. In the first procedure, the magnetic beads are used as a label for actuation,in the second one the same magnetic beads are used as carrier substrate[115], [117].

Rida et al. introduced an original approach based on an alternating magnetic field to perform an efficient mixing in microdevice in a view of further bioassay integration. The local alternating field allows to form stable rotating chains of ferromagnetic beads [118], [119]. The magnetic flux generated by an external electromagnet (3) is guided by a magnetic core and focused by two microstructured soft magnetic tips across a microchannel (Figure I.24). Such magnetic structures behave as a dynamic random porous medium and enhance the interaction between the magnetic beads and the fluid flow through a good mixing efficiency of two parallel flows, in a microchannel.

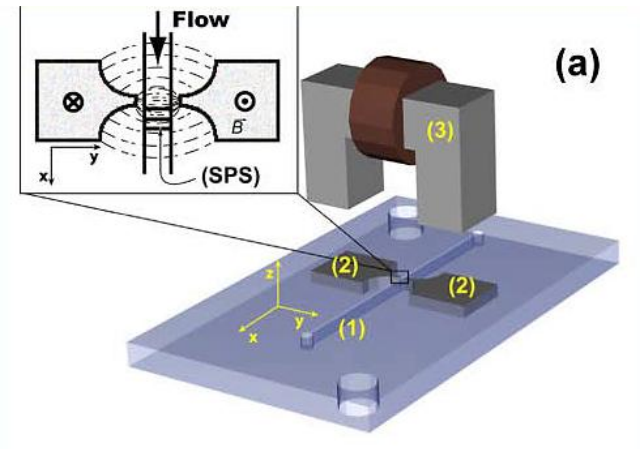

Figure I.24: Schematic view of the experimental system: (1) PMMA microfluidic channel; (2) Soft magnetic parts for magnetic field focusing; (3) Electromagnet. The insert shows a schematic view of the magnetic field distribution between the soft magnetic tips (adapted from ref [118]).

Smistrup et al. reported the functionalization of a microchannel with two types of magnetic beads using hydrodynamic focusing combined with a passive magnetic separator with arrays of soft magnetic elements [120].Needle-like tips are used as soft magnetic elements. When magnetized by an applied field, they generate high local gradients attracting magnetic beads. The system is designed to perform a selective on-chip DNA hybridization assay using two populations of beads functionalized with two kinds of probes (Figure I.25).

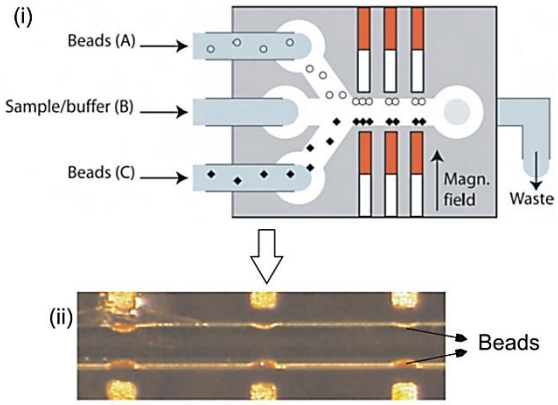

Figure I.25: (i) Schematic illustration of the microsystem and the fluid connections to the three inlets A-C. The two types of beads are introduced through inlets A and C, respectively, and separated by a buffer flow through inlet B. (ii) An optical micrograph showing a part of the microchannel in which the beads are retained in front of the magnetized nickel strip-tips (from ref[120]).

Due to the relatively low magnetic field produced by the integrated electromagnet, the manipulation of particles under flow is limited: the hydrodynamic flow in the microchannels needs to be strongly limited or the magnetic beads have to flow at a very close distance of the planar coil. To overcome this drawback, Lehman et al. proposed to combine integrated coils with a homogeneous field produced by permanent magnets to generate strong magnetic field gradients that could efficiently trap magnetic beads [121].

A similar strategy proposed by Moser et al. has been used to confine and mix functionalized magnetic beads in PDMS microchannel[122]. The goal of this system is to improve the analyte capture efficiency on functionalized beads. The system is an integrated device comprising a quadrupolar magnetic set-up and a microfluidic chip with a single channel (Figure I.26.a). The dynamic actuation of a confined plug is based on the forces exerted simultaneously by a time-varying field generated by the external electromagnet and the constant field of the two permanent magnets on top of the microchannel. Both serve to create a weak permanent bead magnetization and an asymmetric field distribution in the system. As a consequence, beads are attracted cyclically to each side of the microchannel by applying an alternating field to the poles (Figure I.26.b and c).

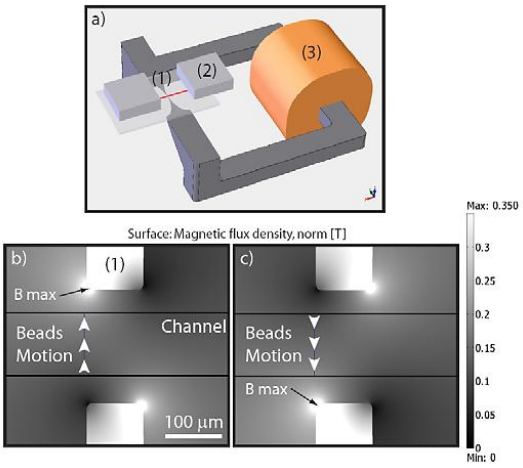

Figure I.26: (a) Schematic view of the whole system, microfluidic chip and the magnetic actuation system comprising two soft magnetic microtips (1), permanent magnets (2) and a coil (3). (b),(c) Representation of the magnetic flux density B and particles moving across the channel, following the maxima of magnetic field (adapted from ref [82]).

These papers illustrate the fact that the combination of electromagnets with permanent magnets may improve the efficiency of on-chip manipulation of magnetic beads. Indeed, Moser et al. could demonstrate the performance and potential of their approach by using a streptavidin-biotin based model assay to find out a detection limit of about $200\ pg/mL$ ($\approx 3\ pM$). Such a procedure requires the use of a reliable magneto-microfluidic platform as soft magnetic tips which are not easily implantable in a microchip. Moreover, bulkiness and heating of such systems remain problematic.

ii. System using permanent magnets

Permanent magnets, used in microfluidic applications, are usually composed of neodymium iron boron (NdFeB). Such permanent magnets enable the formation of a dense and static bead plug by magnetically trapping the magnetic beads in a microchannel, even if they are placed several millimetres away from the channel [123–125]. Hayes et al. proposed a bead-based microfluidic immunoassay using such static plug of 1-2 μm sized magnetic beads [124]. A heterogeneous immunoassay has been demonstrated with a direct interaction of fluorescein isothiocynate (FITC) using beads coated with anti-FITC Ab. First, a strong rare-earth disc magnet placed over the microchannel enables the plug formation, thereafter the beads are exposed to the flow of appropriate reagent and analyte solutions (Figure I.27). Using such magnetic particle trapping, the authors also reported complete sandwich immunoassays for the calibration of parathyroid hormone and interleukin-5, down to a few $\mu g/mL$ (2 to $5\mu g/mL$).

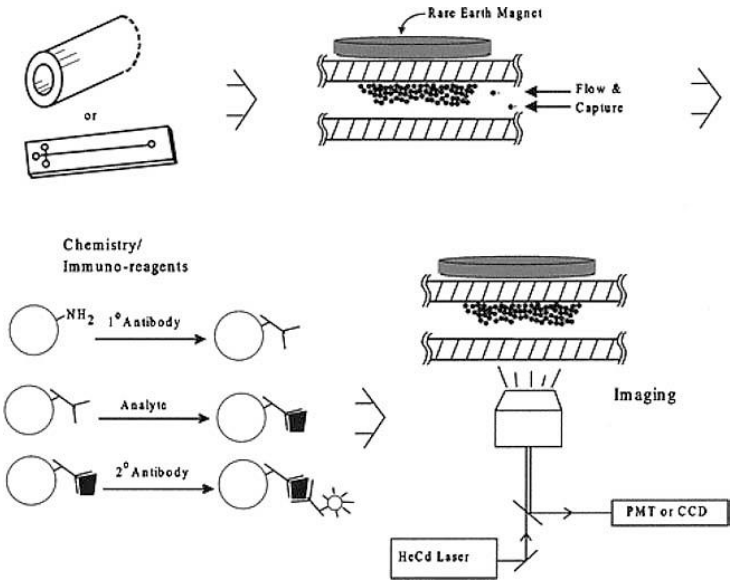

Figure I.27: Schematic representation of a flow-based micro-immuno-assay system using permanent magnets: magnetic beads are collected near a rare earth magnet to form a packed bed within a microfluidic channel. Reagents are introduced into the packed bed to perform a sandwich immunoassay, and then the bed is imaged with a fluorescence microscope (Adapted from ref [124]).

Such magnetic trappingdisplays two major disadvantages; the first one is non-homogeneous distributions of beads across the channel,leading a dramatic decrease of the capture efficiency. The second one is related to the opacity of the plug and/orto the auto fluorescence of certain particles, limiting the direct measure of fluorescence. These drawbacks limitedthe performance of the magnetic beads-based immunoassayespecially theassay sensitivity and analysis time. Base on the same magnet configuration, Zaytseva et al. proposed a microfluidic biosensor module with fluorescence detection for pathogen detection. This module can be operated under a high continuous flow to perfuse the plug through an optimized microchannel design [126].

In order to improve immunoassays, one must first enhance the efficiency of the target capture. For that purpose, several optimization strategies have been digitally simulated by Girault et al.[127]. In particular, they showed that the use of two magnets in attraction allows to forma homogeneous magnetic plug in the channel.

Bronzeau et al. adapted such a configuration and demonstrated the possibility to form successively several plugs of magnetic beads presentingvariousfunctionalization in the same microchannel with external permanent magnets [123]. Thus, such systems allow to perform simultaneously several assays by flushing a sample solution over these plugs. Molecular binding between matching antigen and antibodies occurs in continuous flow and is detected by fluorescence (Figure I.28). Even if this configuration of magnets enables a more homogeneous bead plug, the magnetic field lines are perpendicular to the flow direction leading to a poor permeation through the plug; another drawback is that the plug is not completely extended in the cross-section of the microchannel due to the attractive

configuration. Finally the direct measure by fluorescence within the magnetic plug remains limited because ofits opacity.

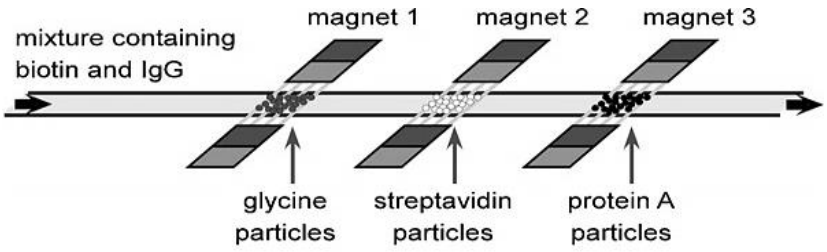

Figure I.28: Schematic representation of system: a fluorescent mixture can be flushed through the three particle plugs featuring surface coatings of glycine, streptavidin and protein A, respectively. Several assays can be performed simultaneously (adapted from ref [123]).

An original approach has been proposed by our team based on permanent magnet in repulsion with an orientation of 30°. Such configuration has been applied to develop a microdevice for the detection of pathological prion protein [1], [125]. Strong permanent magnets are used to create a magnetic field parallel to the flow with a strong gradient pointing through the channel centre. This configuration was applied to immobilize magnetic Trypsin coated beads. Under the effect of a magnetic field, these beads are self-assembled to form several open-tubular-like columns on-chip to favour liquid flow through the plug.

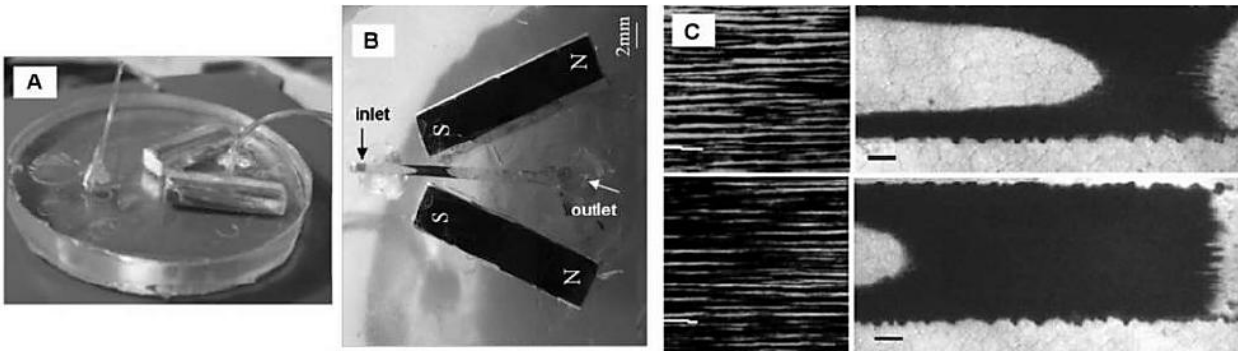

Figure I.29 : Experimental setup used for the protein digestion experiments: Picture of the PDMS chip (A). (B) Expanded view of the magnetic beads immobilized between the two magnets in the microchannel (B). Picture of the magnetic bead plug has its early and late stage of formation. The orientation of the bead arrays parallel to the channel's axis, providing a low flow resistance and uniform pore size, is visible (C).

This system taking advantage of a porous magnetic particle plug to perform a protein digestion hashigher reaction kinetics than the conventional batch reactions (i.e. accelerated 100 fold).

Lacharme et al. proposed complete on-chip immunoassays which were performed by using geometrically trapped self-assembled magnetic nanoparticle chains [128]. This original approach is based on the retention of nanoparticle chains in a microfluidic channel with periodically enlarged cross-sections (Figure I.30). In this way, nanoparticle chains strongly interact with the flow and specifically capture a low number of target molecules (down to

105), in matter of minutes. As an example, the detection of murine monoclonal antibodies was demonstratedwith a LODof 1 ng/mL. This work shows that magnetic nanoparticles chains positioned across the microchannel strongly improve the capture efficiency through a high "interaction"between the analyte flow and the magnetic beads. In addition, the gap between the chains permits a direct detection by fluorescence with a better sensitivity than the previous exampleswhere the opacity of the plug did not enabledirect fluorescence detection.

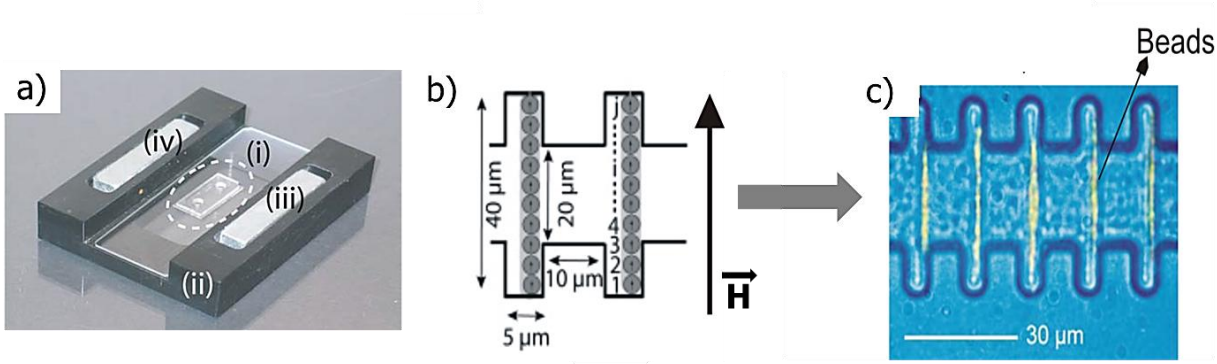

Figure I.30: (a) Schematic illustration of the system: microchannel (i), the two permanent magnets (iii) and (iv). (b) Microchannel with a periodically varying cross-section of 20 to 40µm. Magnetic beads are retained under uniform magnetic field $\vec{H}$. (c) An optical micrograph showing the coated beads (From ref [128], [129]).

Another original and elegant concept using a continuous flow method was proposed by Pamme et al.to separate magnetic from non-magnetic particles [130]. This method was termed on-chip free-flow magnetophoresis and uses an external permanent magnet placed on one side of a microfluidic chamber. Magnetic particles are dragged into the magnetic gradient field and left the chamber via one of the other outlet channels depending on their magnetic susceptibility and their size (Figure I.31.a).More recently, Peyman et al. used this concept to perform a continuous flow immunoassay (Figure I.31.b)[131]. Magnetic beads are deflected through parallel reagent streams[1]. This allows several binding and washing steps as well as detection, in the same chamber. In addition, the main advantage of this method is the complete particles-liquid interaction which means that the entire bead surface can be in contact with the sample. So as to show the feasibility of the concept, a sandwich immunoassay was performed on-chip.This system, however, displayed a relatively high detection limit. This limitation arises from the short time incubation i.e. the time during which beads are immersed in each reagent. Moreover, beads can only move in one direction. In order to get around this disadvantage, Sasso et al. proposed to add another permanent magnet to move the beads back in the buffer solution [132].

[1]The flow stayslaminar in the microfluidicdevice,reagents do not mix in the chamber.

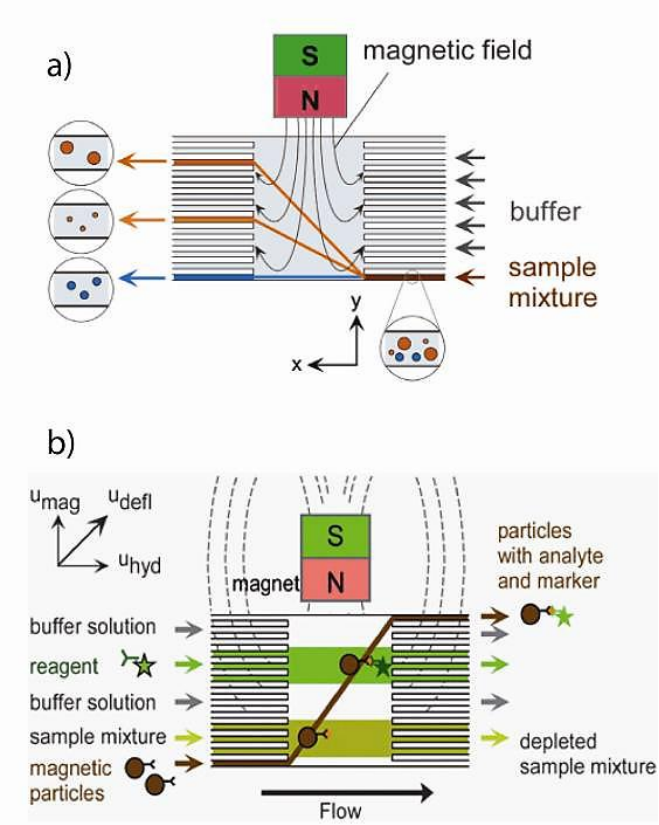

Figure I.31: (a) Concept of the free-flow magnetophoresis. A magnetic field is applied perpendicular to the direction of the liquid flow. Beads are deflected perpendicularly to the flow according to their size and magnetic susceptibility and are thus separated (adapted from ref [130]). (b) A sandwich assay is depicted schematically: deflection of magnetic beads through multi-laminar reagent streams across the reaction chamber. Binding and washing steps are consecutively performed on their surface in continuous flow (adapted from ref [131]).

In summary, it can be seen from this partial overview of the literature, that the use of magnetic particles in microfluidic systems is a very vivid and inventive field, in which numerous new concepts were proposed within a few years. This creativity also reflects, on its backside, that no ideal system was found so far, in spite of this intense creativity.

Chapter II. Integrating fluidized beds in microfluidic systems

1. Introduction

As described in the first chapter, the use of superparamagnetic particles in microfluidic systems is extremely advantageous for capture and extraction applications as it presents the benefit of a large surface-to-volume ratio, a flexible surface functionalization and exploits the magnetic properties of the microparticles that allows for easy non-contact manipulation.

Various magnetic based systems have been proposed in the past by our group (see e.g. [1]) and others (see e.g. [2], [3]) and interesting performances were reported. Earlier systems by our group involved either an immobilized matrix of large magnetic particles, or a "plug" held in place with a pair of magnets facing each other across the microchannel [1]. In the first system, the magnetic elements are large and stationary so it is limited by mass-transfer or reaction kinetics. The second approach showed interesting performances regarding biological applications but so far their hydrodynamic characteristics were not investigated in detail. We will show, that at high flow rates, a "fracture" regime occurs, inducing inhomogeneous perfusion of the plug and reduced efficiency [2], [3].

All along this chapter, we will emphasize the role of the magnetic field distribution on the resulting magnetic forces and on the bed behaviour. After a careful study of this first device generation at both magnetic and hydrodynamic level, we will present an innovative design that overcomes the above limitations. By combining measurement of flow-pressure characteristics magnetic field numerical simulations and optical observations we will show that the behaviour of this new design can be directly related to that of conventional macroscopic fluidized bed and thus offering improved reproducibility, performances and workability.

2. Magnetic microparticle transport in a microfluidic device

The fundamental forces acting on superparamagnetic microparticles in a viscous solution under an external magnetic field are magnetic$\vec{F}_{mag}$, hydrodynamic drag$\vec{F}_{drag}$, gravitational $\vec{F}_g$ and buoyancy $\vec{F}_{buo}$ forces. In general, due to the small size of themicroparticle, one assumes that $\vec{F}_g$ and $\vec{F}_{buo}$ may be neglected to describe the motion of a magnetic microparticle [133], [134].

a. Magnetic force acting on a particle

In our experiments, we focused our attentions on *MyOne* and *M-280* superparamagnetic particles from Dynabeads®. They both offer a very narrow distribution in

size with a mean diameter of 1.05 μm and 2.83 μm respectively [135]. Figure II.1 shows the magnetization curve of both particles.

Three regions may be distinguished on the magnetization curve of Dynabeads®. In the first region (a), the external magnetic field is weak and the microparticle magnetization is proportional to the applied magnetics flux density (thus satisfying the equation: $\vec{M} = \chi\vec{H}$) in contrast to the second region (b) where the relation between the magnetization of the microparticle and magnetic flux density is not linear. In the third region, for fields typically above200 mT, corresponding to the saturation region, the magnetization of the microparticle converges towards the saturation magnetization M_{sat} (Figure II.1.c).

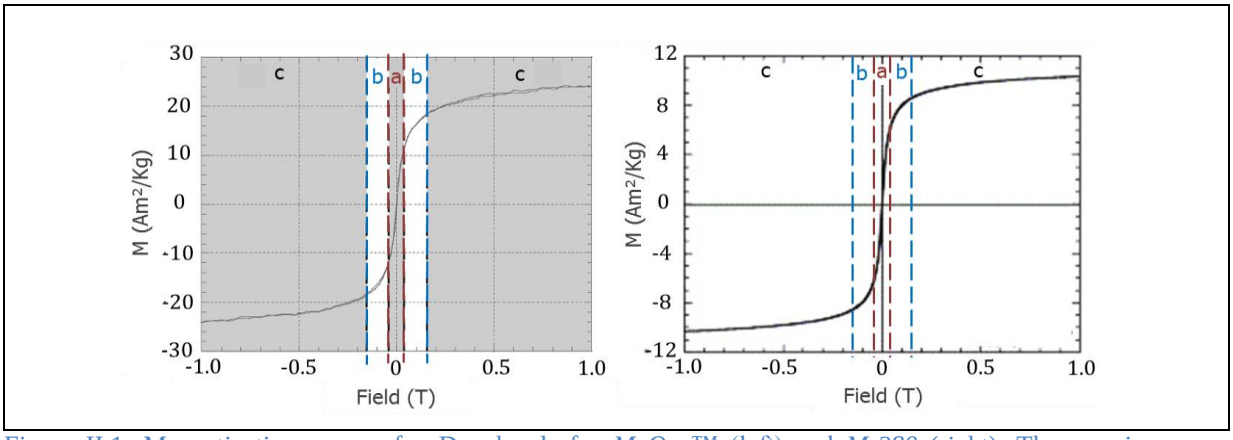

Figure II.1: Magnetization curve of a Dynabeads for *MyOne*™ (left) and *M-280* (right). Three regions are distinguishable: (a) linear and (b) nonlinear variation between the flux and the flux density B and the microparticle magnetization M, (c) saturation (constant magnetization) (adapted from ref [135]).

The characterisation of the magnetic properties of Dynabeads® particles such as *MyOne*™and*M-280*(Invitrogen) was made by Fonnum et al. [135]. The results from this paper are very useful for the understanding of microparticle magnetic behaviour. Table 1 summarizes the main physical properties of the particles used in our experiments.

Microparticle	Diameter$d_p\,(\mu m)$	Density $\rho(g/cm^3)$	Iron oxide (mg/g)	Mass susceptibility$\chi_{mass}\,(m^3/Kg)$	$M_s(KA/m)$	Volume$V_p\,(m^3)$
MyOne™	1.05	1.7	255	$81 \cdot 10^{-5}$	336	$6.06 \cdot 10^{-19}$
M-280	2.83	1.4	118	$54 \cdot 10^{-5}$	336	$1.19 \cdot 10^{-17}$

Table 1: Physical properties of the *MyOne*™ and *M-280* magnetic microparticles from Invitrogen.$\chi$is the initial magnetic susceptibility, M_s is the intrinsic spontaneous magnetization of the nanoparticles in the microparticles. (Adapted from ref [135]).

Note: From the magnetization curve of a microparticle, one can note that the slope at low field is characterized by magnetic susceptibility of the particle also called effective susceptibility χ_{eff}*. The latter takes into account of the demagnetization effect itself related to the intrinsic material susceptibility* χ_{mat}*.Indeed, in presence of a magnetic field, a demagnetization field appears and is acting to reduce the internal field inside the microparticle. This means that the effective susceptibility of one microparticle is influenced by the demagnetization factor* N_d *and therefore given by:*

$$\chi_{eff} = \frac{\chi_{mat}}{1 + N_d \chi_{mat}}$$

Equation 1

Where N_d *is equal to* $1/3$*for a perfectly spherical particle* [136].

In the linear region (a) of the magnetisation curve, for a superparamagnetic microparticle suspended in a weakly diamagnetic medium such as water, the magnetic moment can be written in the following form:

$$\vec{m} = V_p \vec{M} = V_p \, \Delta\chi \vec{H} = \frac{V_p \, \Delta\chi}{\mu_0} \vec{B}$$

Equation 2

Where($\Delta\chi = \chi_p - \chi_w$)is the difference in magnetic susceptibilities between the microparticles and the surrounding medium[2].$\vec{M}$is the microparticle magnetization and $V_p = \frac{4}{3}\pi r_p^3$ is the volume of a magnetic microparticle with a radius r_p.

The energy E_m of a point-like magnetic dipole or magnetic moment $\overrightarrow{m}$in a magnetic flux density $\vec{B}$ is given by:

$$E_m = -\mu_0\left(\vec{m}.\vec{H}\right) = -(\vec{m}.\vec{B})$$

Equation 3

The corresponding magnetic force $\vec{F}_{mag}$ is given by:

$$\vec{F}_{mag} = -\nabla(E_m) = \nabla\left(\vec{m}.\vec{B}\right) = (\nabla\vec{m}).\vec{B} + \vec{m}.\nabla\vec{B} \approx (\vec{m}.\nabla)\vec{B}$$

Equation 4

Assuming that$\overrightarrow{m}$has no spatial dependence (e.g. the bead is in the saturated state) $\vec{F}_{mag}$ is thus expressed as the product of $\overrightarrow{m}$ by the gradient of the magnetic potential energy E_m

The magnetic moment can be considered as being parallel to the field. Thus, if $\vec{m} = (m_x, 0, 0)$then$\vec{m}.\nabla = m_x\frac{\delta}{\delta x}$ and a force will be experienced on the dipole provided there is a field gradient in $\vec{B}$ in the x-direction [137], [138].

For a single superparamagnetic particle, the magnetic force can be expressed by the following integral over the volume V_p of the particle [139]:

$$\vec{F}_{mag} = \mu_0 \int_{V_p} (\vec{M}.\nabla)\vec{H}\,.dv = \mu_0\,\Delta\chi \int_{V_p} (\vec{H}.\nabla)\vec{H}\,.dv$$

Equation 5

An exact calculation of the magnetic forces acting on a bead clusters are difficult to establish in the general case. Indeed, the applied magnetic field $\vec{H}$ is not uniform in the magnetic tweezers gap and is altered by the presence of the particles. For a sufficiently large applied magnetic field, the length scale of the magnetic field gradient is the microparticle diameter, such that the integral can be considered constant over the volume of the microparticle. Literature often introduces a simplified form of this equation using an ideal magnetic point

[2] The magnetic susceptibility of the suspending medium can be neglected.

dipole approximation and the overall response of the microparticle plus water system can be approximated by $\vec{B} = \mu_0 \vec{H}$, so the Equation 4 becomes[3]:

$$\vec{F}_{mag} \approx V_p \frac{\Delta\chi}{\mu_0} (\vec{B}.\nabla)\vec{B}$$

Equation 6

In addition, provided there are no time-varying electric fields or currents in the medium, we may take advantage of the following mathematical identity: $\nabla (\vec{B}.\vec{B}) = 2\vec{B} \times (\nabla \times \vec{B}) + 2 (\vec{B}.\nabla)\vec{B}$. As there is no source of the field $\vec{B}$ in the medium[4], we can apply the Maxwell equation: $\nabla \times \vec{B} = 0$,so as to obtain the previous equation in the following form:

$$\vec{F}_{mag} \approx V_p \Delta\chi \nabla \left(\frac{\overrightarrow{B^2}}{2\mu_0} \right)$$

Equation 7

This equation shows that a magnetic field gradient is required to exert a force on a microparticle [72]. In the caseof a uniform field, the microparticle is only submitted to a torque, forcing it to align along the field direction , without any translational effect [140].

To considerthe saturation regime (region c), the magnetic moment of microparticle $\overrightarrow{m}$ is equal to $\overrightarrow{m}_{sat}$ and remains constant, the Equation 4 can be expressed as following:

$$\vec{F}_{mag} \approx (\overrightarrow{m}_{sat}.\nabla)\vec{B}$$

Equation 8

In such a case, the magnetic force acting on a saturated microparticle is directly proportional to the gradient of the magnetic flux density.

As an example, the magnetic moment of *MyOne*™ is $m_{sat} = \rho_p M_{sat} V_p = 1.78 \cdot 10^{-14}\text{Am}^2$, with the particles density $\rho_p = 1700\text{kg/m}^3$ and $M_{sat} = 20\text{Am}^2/\text{Kg}$ deduced from the magnetization curve (Figure II.1).

In most of the simulations performed in this work, the magnetic field used in our experiments typically correspond to the nonlinear regime in the magnetization curves. As a consequence,

[3]For example, when $\vec{B}$ applied in the x direction $\vec{F}_{mag,x} = \frac{V_p \Delta\chi}{\mu_0}\left(Bx\frac{\partial}{\partial x} + By\frac{\partial}{\partial y} + Bz\frac{\partial}{\partial z}\right)Bx$.

[4]There is no time-varying electric field or currents in the medium.

we did not consider any approximation concerning the magnetic susceptibility value of the particles.

b. Viscous drag force

In this project, our objective is to create a magnetic trap that is able: (i) to capture magnetic particles from a liquid suspension injected in a microfluidic channels and (ii) to generate confinement forces that can withstand the hydrodynamic drag of the liquids to be injected during the protocol step. $\vec{F}_{drag}$ arises from the viscous drag exerted by the medium on the microparticles. This force is directly related to the particle size and the flow regime given by Reynolds number R_e. (Assuming that the magnetic microparticles have a low density in the suspension, thereby the presence of multiple particles in close proximity to each other is neglected [141]).

For low Reynolds number flows($R_e \ll 1$), the drag force on a spherical microparticle of radius r_p, in a fluid moving with a relative velocity$\Delta\vec{v}$, is given by Stokes's law in the following form:

$$\vec{F}_{drag} = 6\pi\eta r_p \Delta\vec{v}$$

Equation 9

whereη is the viscosity of the surrounding medium (for water,$\eta = 8{,}9 \cdot 10^{-4} Pa.s$). As an example, the drag force on a *MyOne* magnetic bead still held in water flowing at a velocity of $1\ cm/s$ is around $\vec{F}_{drag} \simeq 0.1\ nN$.

c. Particle mobility

As above-mentioned, two forces act on a superparamagnetic microparticle in the microfluidic microchannel. The equation of motion of the particle moving in a fluid flow can be written as:

$$m\frac{\partial v}{\partial t} = \vec{F}_{mag} + \vec{F}_{drag}$$

Equation 10

In a microfluidic channel, the small length scales and the slow particle motion result in a pure laminar flow($R_e \ll 1$). For this type of flow, the inertial forces can be neglected compared to the viscous one. Under these approximations, the resulting equation of motion of the microparticle is:

$$\vec{F}_{mag} = -\vec{F}_{drag}$$

Equation 11

In this case, a simplified schematic diagram of the forces acting on the magnetic microparticle is shown in Figure II.2.

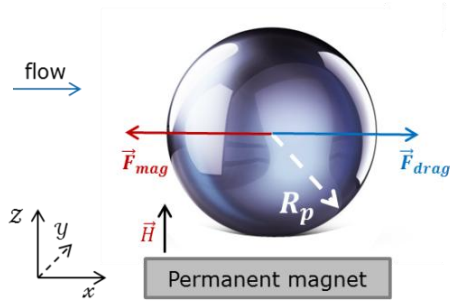

Figure II.2: Schematic illustration of the main directions of $\vec{F}_{mag}$ and $\vec{F}_{drag}$ acting on a particle with radius R_p positioned at a distance z from a surface.

Thus, equalizing Equation 7 and Equation 9 and writing $V_p = \frac{4}{3}\pi r_p^3$,gives the microparticle velocity relative to the carrier fluid as:

$$\Delta\vec{v} \approx \frac{r_p^2 \Delta\chi}{9\mu_0\eta}\nabla\left(\overrightarrow{B^2}\right) \approx \frac{\xi}{2\mu_0}\nabla\left(\overrightarrow{B^2}\right)$$

Equation 12

With $\xi \approx \frac{V_p \Delta\chi}{6\pi\eta r_p}$

Equation 13

ξ *is* called "magnetophoretic mobility" of the particle. This parameter describes how manipulable a magnetic microparticle is. Generally speaking, one can note that magnetic microparticles have much greater magnetophoretic mobility than nanoparticles.

3. Magnetic microparticle motion within a plug

The above-mentioned basic concepts of magnetism and hydrodynamic are needed to understand how the magnetic microparticles behave along a microfluidic channel when subjected to an external magnetic field.

In the following, we will investigate the hydrodynamic response of an ensemble of microparticles confined as a plug in a channel. For this purpose, the experimental study was compared to simulations of the main forces acting on microparticles in a microfluidic system.

Firstly, we will describe the experimental set-up and the procedure used to capture the microparticles. Subsequently, the simulations results and the microparticle behaviour during the capture step are discussed. Finally, the hydrodynamic response of different types of plugs will be presented and discussed.

a. Microchip design: 1st generation

The concept of the microchip design is based on a system previously developed by our group, that allows for the formation of a dynamic plug in between a single pair of permanent magnets [142]. A picture of the microchip is shown in Figure II.3. It consists in a single microfluidic microchannel, which is 1 mm wide by 250 μm high and 2 cm long including an inlet and an outlet. This microchip is fabricated using soft lithography and rapid prototyping with PDMS technology. Briefly, a SU-8 master is fabricated through photolithography on silicon substrates. After casting and curing, the PDMS microchannelswerebonded on a PDMS-coated ($\sim$500 μm) glass substrateusing an Oxygen plasma bonding method. Teflon[5] tubes are then connected at the inlet and outlet of microchannel in order to inject and collect the different solutions. The inlet may be connected to a syringe pumps or to another pressure-driven controller.

In order to secure the microfluidic system against leakage, we used Upchurch connectors between the microchip and the other microfluidic accessories, due to their ability to withstand very high pressures.

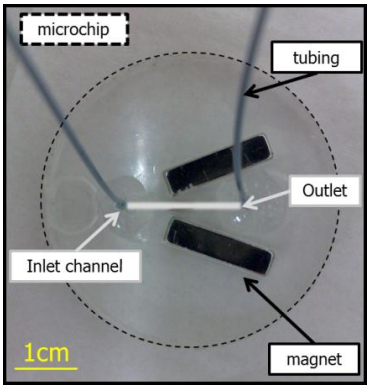

Figure II.3: PDMS chip with the microchannel between two permanent magnets connected to the rest of microfluidic system by two inlet-outlet silicone tubing.

To generate a magnetic trap, two NdFeB permanent magnets[6] are inserted on both sides of the PDMS chip in close vicinity of the microchannel ($< 500\ \mu m$). Each magnet

[5] Named PTFE (Polytetrafluoroethylene), $-(-CF_2-CF_2-)_n-$
[6] Neodymium Iron Boron magnets are from Chen Yang Technologies (Finsing, Germany).

forms an angle of 30° relative to the microchannel axis. Both magnets are positioned in a repulsive configuration and are polarized in the longest dimension[7] with a magnetic remanence of 1.3 Tesla. This particular geometry generates a magnetic trap located in between the two magnets where magnetic microparticles can be captured. The accumulation of particles leads to the formation of a magnetic plug that fills the whole microchannel section. The performances of this magnetic plug design for the capture were partially investigated by N. Minc and more recently by A. Le Nel. In particular, it was demonstrated that such a magnetic systemcould be applied to enzymatic digestion on-chip as previously demonstrated [1], [125]. Nevertheless, no careful investigation of hydrodynamic properties of the magnetic plug was reported so far. The objective of the present study is to provide a clear understanding of the particle behaviour in the plug which is crucial to enhance the capture efficiency of static and dynamic plug during the immunoextraction.

In order to undertake a hydrodynamic study of the plug in different conditions, we decided to use a simplified and more integrated version of the device as shown in Figure II.4. Our motivation was mainly to reduce the fabrication process constraints. In this configuration, the microchannel is a square capillary in borosilicate glass[8] mounted on a homemade copper holder that is used to adjust the height of the capillary. The glass tube is directly connected to PolyEtherEtherKetone(PEEK) tubing using Upchurch connectors. This device allows changing the microchannel geometries or the positioning of the magnets relative to the microchannel without affecting the rest of the microfluidic platform. In order to investigate the influence of the magnetic field on particles, the distance between the magnet and the capture area in the microchannel has to be precisely controlled. Two parameters were modified in this regard: (i) the distance between the magnet and the channel wall, (ii) the magnet thickness relative to the capillary one. For that, the precise tuning of each magnet position relative to the capillary can be easily carried out with two independent linear translation stages along y-axis.

[7] A dimension of the magnet is 4x4x16mm^3.
[8] The borosilicate glass capillaries are from VITROTUBES™.

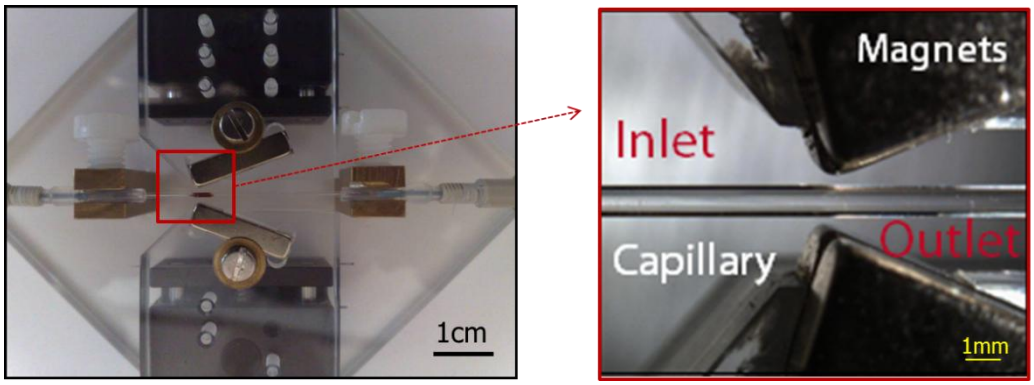

Figure II.4: (a) photograph of the magnetic system with a square-section glass capillary ($0.5\ x\ 50x\ 0.5\ mm^3$) and the two linear translation stages along y-axis serving to fine-tune the magnets position relative to the capillary. (b) Enlarged view of the interest area in the magnetic system taken with transmission stereomicroscope.

b. Microparticle capture principle

The first important step of an assay protocol is the capture of the microparticles in a defined area within the microchannel. During this step, all the microparticles have to be extracted from the surrounding medium. The optimisation of the trapping efficiency is critical as the amount of particles will directly influence the behaviour of the plug and its capture capacity (i.e. the specific surface) for a subsequent assay. The microparticle trapped in a microchannel was monitored by microscope imaging.

Figure II.5 shows time sequence of images thatillustrates the different stages of the magnetic microparticles capture and finally their assembly into a dense plug. Here, a suspension of superparamagnetic microparticles ($0.5\ mg$ of Dynabeads®), with a $1.05\ m$diameter is injected in the device. When passing in between the two magnets, the particles are deviated by the magnetic field gradient from the flow direction towards the microchannel sides then forming two distinct plugs. Gradually, the microparticles invade the whole volume between the two magnets thus causing the creation of a dense plug which grows in the flow direction.

In this experiment, the injection is performed using a MAESFLOas a pressure regulator. The difference of pressure between the inlet and outlet is kept constant during the whole experiment ($50\ mbar$). This value was already found to be the optimum to get an efficient trapping while minimizing the microparticle settling in the tubing during the injection. Obviously, the injection time varies according to the experimental conditions. The microparticles were trapped at an initial flow rate of $2\ mL/h$. During that time, the flow rate value progressively decreases down to attain $0.3\ mL/h$. As the plug is growing, the amount of free space in the capture area decreases thus leading to an increase of the hydrodynamic resistance.

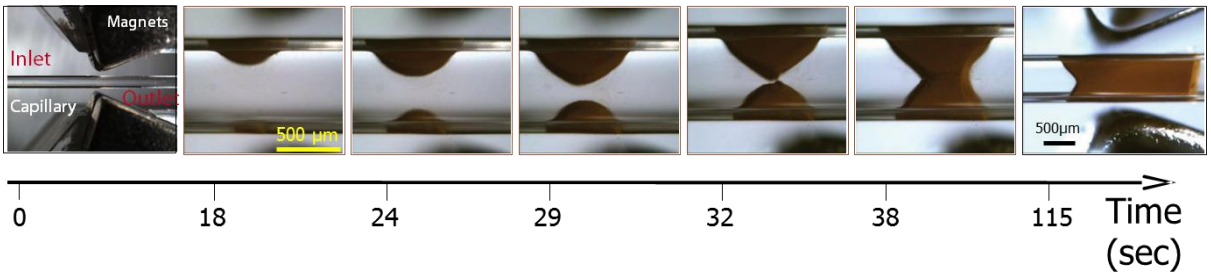

Figure II.5: Formation of a dense plug between the two permanent magnets. The sequence of photographs shows the arrangement of the magnetic microparticles at different stage of the plug formation.

c. Structure of the magnetic plug

In the first part of the chapter, we introduced some aspects of magnetism theory showing how a magnetic field may be used to manipulate magnetic microparticles. As we have already mentioned, magnetic microparticles are made up of iron oxide nanoparticles and, due to their small size (about 10 nm diameter), they exhibit superparamagnetic properties. In presence of a magnetic field, the magnetic moment of an iron oxide grain within the microparticle aligns along the external magnetic field leading to a global particle magnetization in the same direction. One of the most interesting properties of superparamagnetic microparticles is their ability to form chains and clusters in presence of magnetic field due to the magnetic dipole interaction between the moments induced in the microparticles [143]. These dipole interactions lead to an instantaneous self-organisation into columns of a suspension of superparamagnetic microparticles in the field direction. Conversely, when removing the magnetic field, the particles lose their magnetization and disassembly takes place. As the plug cohesion collapses, the microparticles can be flushed out of the channel.

The device configuration enables the creation of a magnetic field parallel to the flow with a strong gradient between the two permanent magnets whereby the microparticles self-organize into columns parallel to the magnetic field i.e. parallel to the midline of the microchannel (see Figure II.6.a). This configuration is favourable to liquid flow through system pores oriented along the liquid flow. The distance between the columns is maintained by dipole-dipole repulsion a reduced hydrodynamic flow resistance which is favourable for permeation into the plug (see Figure II.6.b).

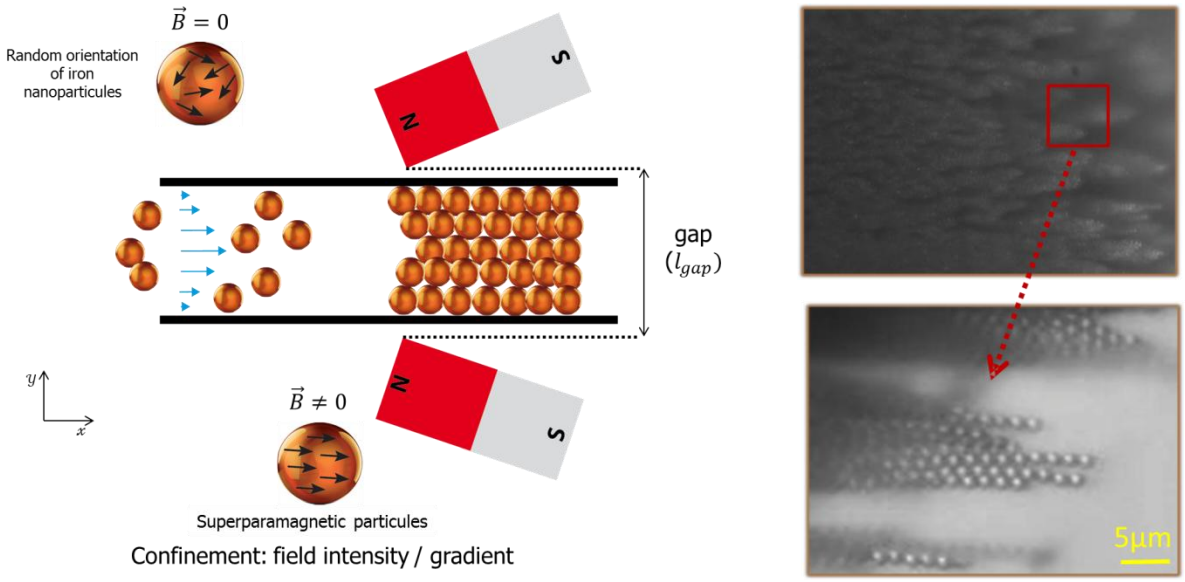

Figure II.6: (a) Schematic view of the formation of the plug. Each magnet forms an angle α of 30° relative to the microchannel axis (the geometry of the channel: 1 mm wide by 250 μm high and 2 cm long) and the gap length, l_{gap} is the space in between them, equals to 2 mm. The microparticles self-organized into columns in the presence of an external magnetic field. (b) The picture on the right shows the structure of plug at its end and the picture on the left is an expended view, showing the columns oriented in the direction of the field.

N. Minc et al. investigated different shapes of the microchannel as well as orientations of the magnets. Their motivation was to provide a strong gradient field to maintain the plug stability even at high flow rate and a magnetic field oriented parallel to the flow. To reach this goal, they found that the best confinement and plug homogeneity were obtained when arranging the magnets in a repulsive conformation, with the polarisation making a small angle (30°) with the microchannel axis [144].

d. Forces acting on a magnetic bead in a flow

Finite Element Method simulation (FEM) was carried out using Comsolmultiphysics 4.1 (3D) to investigate the spatial distribution of the magnetic field in the channel. Our objective is to provide a spatial force distribution along the microchannel. As discussed above, the force acting on superparamagnetic microparticles was calculated according to: $\vec{F}_{mag} \approx V_p \frac{\Delta\chi}{\mu_0} (\vec{B}.\nabla)\vec{B}$(Equation 6).

Figure II.7.a shows the magnetic field intensity (colour map) and its orientation (black arrows), in a plane oriented perpendicularly to the z-axis and aligned along the centre of the microchannel. The x-axis corresponds to the microchannel centre, while the y-axis is aligned along the gap in between the magnets. As can be seen, the magnetic field in the channel, between the magnets is not homogeneous, even if the repulsion arrangement produces a strong x-component of $\vec{B}$ in the center of the channel. The microparticles experience a spatially varying force-field.

The plug picture given in Figure II.7.b is in good agreement with the simulations.

- The front edgeof the plug is curved under the influence of the magnetic field intensity distribution and shows a profile very similar to the one observed in figure 7a.
- The particle density in the plugs follows the intensity distribution of the magnetic field: the most packed areas being located on the edges of microchannel, where the magnetic field is the strongest.

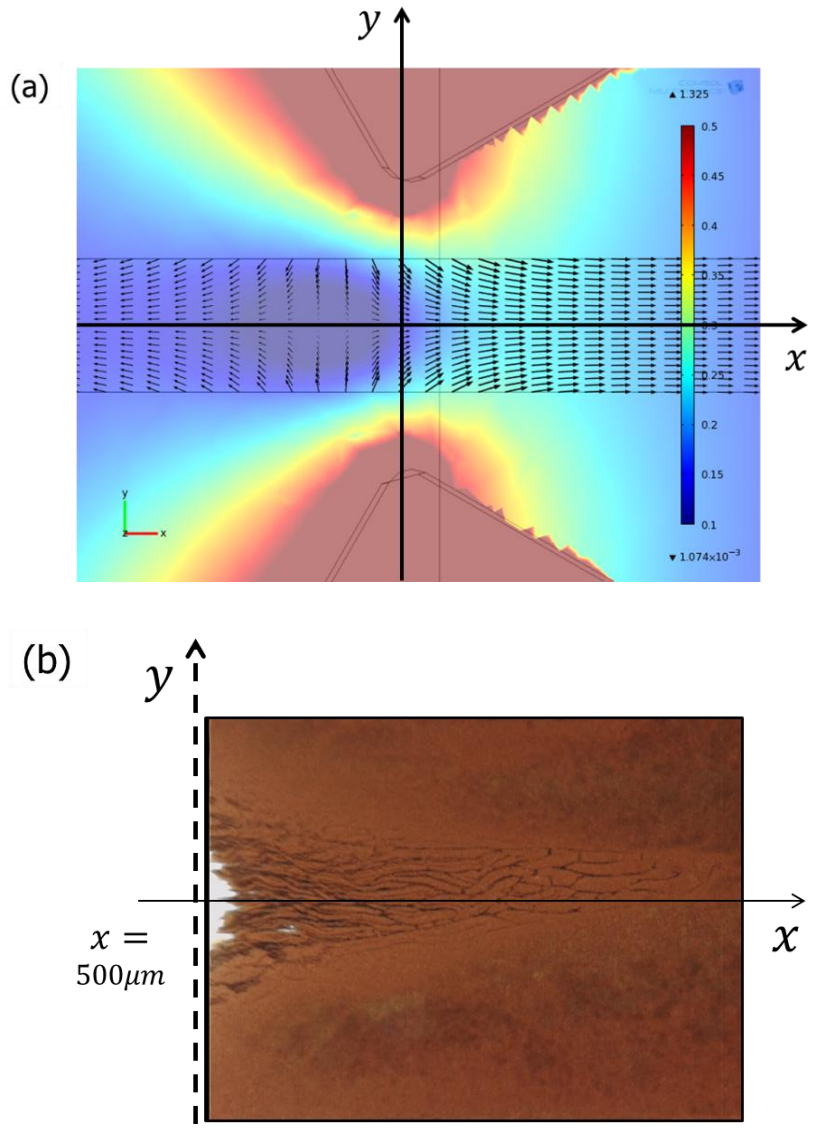

Figure II.7: (a) 3D simulation of the magnetic field intensity (Tesla) created by two permanent magnets around the channel. (b) Picture of a magnetic plug located at $x = 500\ \mu m$.

For a more accurate investigation of the forces experienced by the particle, we calculated the magnetic interaction energy between the particles and the field at several locations in the channel. For this purpose, we first searched out an equation to fit with the magnetization curve of *MyOne*. This equation allows to calculate the magnetic moment for any magnetic field intensity ($\vec{m} = \chi.\vec{B}$) and finally the magnetic energy ($E_m = -(\vec{m}.\vec{B})$).

Figure II.8 illustrates the spatial evolution of the magnetic energy for a single particle in the microchannel, along the x-axis. The energy distribution shows a minimum energy level in between the magnets. In this region, the magnetic force thus reaches a maximum which corresponds to a potential confinement region for the particles. Indeed, this result is in fairly good agreement with the experimental observations that show that the position of the magnetic plug matches the expected confinement region. Locally, the magnetic force overcomes the hydrodynamic drag and stabilizes the particles location. Due to the magnetic field symmetry imposed by the location and repulsive orientation of the magnets, at a given x position along the microchannel, we can observe:

- a minimum field intensity value is found in the centre of the channel (point A).
- a magnetic force intensity which increases when getting close to each magnet (point B and B').

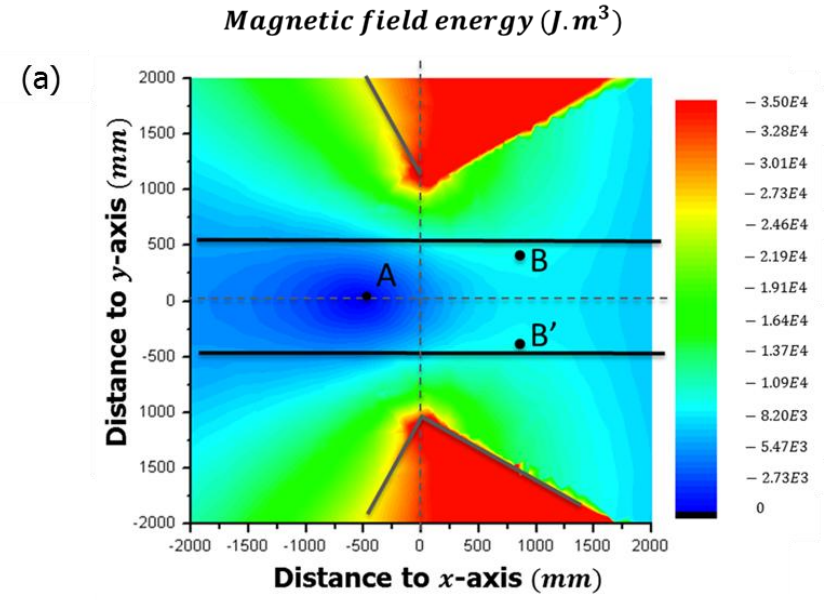

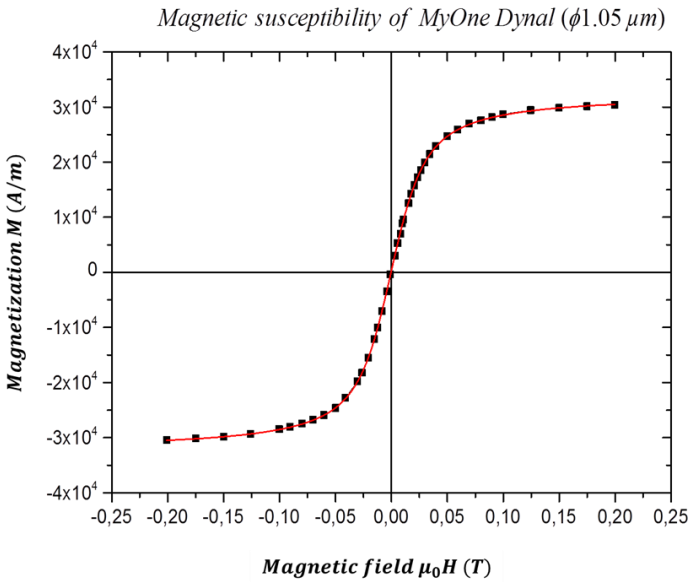

Fit Equation: Langevin formalism

$$y = C\ [\coth(x \cdot x_c) - \frac{1}{x \cdot x_c}]$$

	Value	Standard error
Magnetization	$x_c = \left\{\frac{\mu_0 \mathrm{mH}}{\mathrm{KT}}\right\}$	83.03
	$C\ (= \mathrm{M})$	$3.24 \cdot 10^4$
Adj. *R*-Square	0.999	

Figure II.8: (a) Evolution of the magnetic energy for a single particle in the centre of the microchannel. Points A and B represent the minimum and the maximum energy level, respectively. (b) Plot of the magnetic susceptibility of the *MyOne*[145], [146].

Microscopic visualization of the magnetic microparticles during the early stage of the plug formation also confirms this simulation results and clearly indicates the presence of two confinement regions near the edges of the magnets. At first, the injected microparticles are randomly dispersed in the microchannel. Once the microparticles are close to a channel area in between the permanent magnets, they are easily deviated in the y-direction by the magnetic force and trapped close to the magnet on the channel walls (Figure II.10). At this place, the magnetic force intensity is maximal, as predicted by the simulations.

Figure II.9 represents the plots of magnetic field intensity versus distance. These results corroborate the microscopic observations of the plug.

- Plot a is simulated with $x\ [-0.5; 0.5] \cdot 10^4$ and $y = 0\ \mu m$. As a result, B_y (component of the magnetic field on y-axis) remains zero on channel x-axis while B_x is zero at the origin increasing to a maximum at the points (0, -0.5) and (0.5, 0). The magnetic force changes sign
- Plot b is simulated with $x\ [-0.5; 0.5] \cdot 10^4$ and $y = 250\ \mu m$. We can notice that B_y attains is maximum value at the point (0, 250) which allows to deviate the particles toward the magnets.
- Plot c is simulated with $x = 50\ \mu m$ and $y\ [-500; 500]$. In this case, B_y is zero at the origin increasing to a maximum at the points (0, 500) and (0, -500) while B_x slightly increase close to the channel sidewalls.

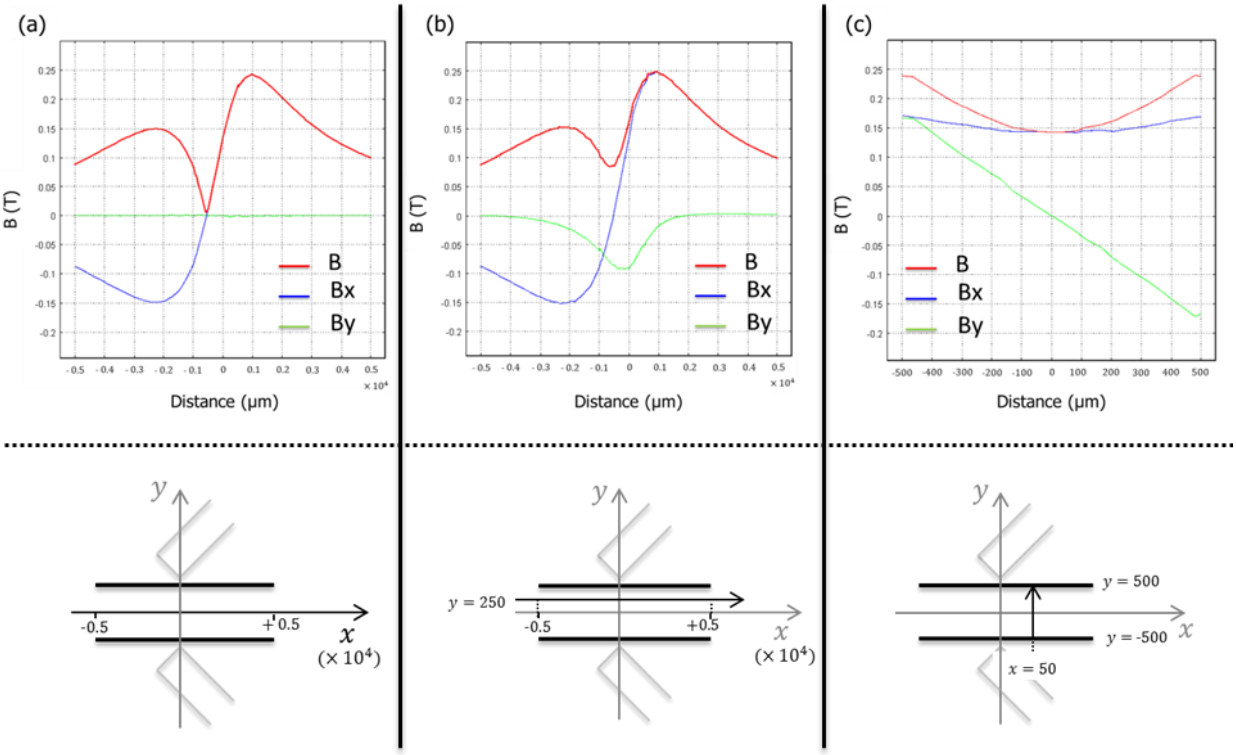

Figure II.9: Plot of the magnetic field intensity versus distance: (a) in direction of the channel at $y = 0$, (b) in the direction of the channel at $y = 250\ \mu m$ and (c) in the cross-section of the channel at $x = 50\ \mu m$. The origin of the coordinate being the intersection of the channel axis with the perpendicular joining the nearest ends of the two magnets to the channel.

Numerical simulations using the FEM allowed a precise study of the magnetic field produced by the permanents magnets, its distribution according to the configuration and the location of the magnets relative to the channel. Thus, the magnetic force distribution determines wherethe magnetic particles may be attracted in the channel. All these simulations were corroborated by the microscopic imaging of the plug during its formation and might explain the weaknesses of plug during the perfusion.

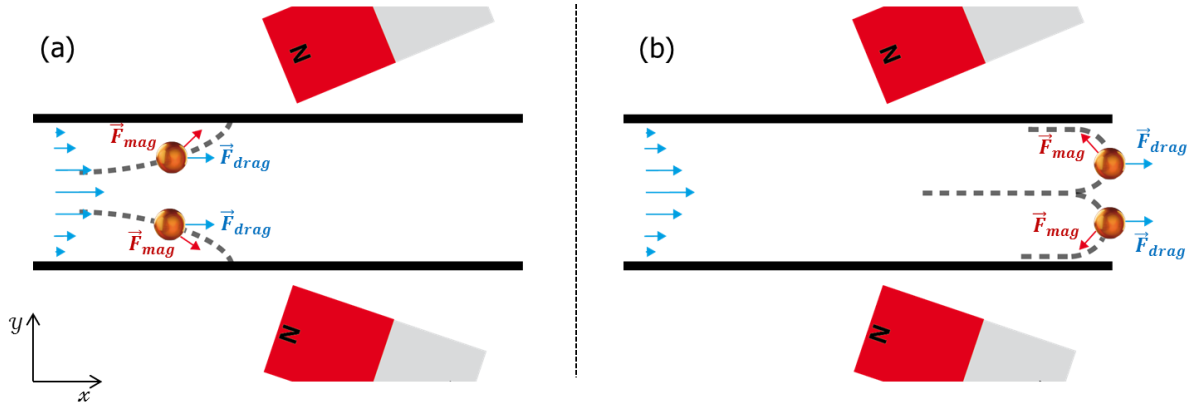

Figure II.10: (a) The microparticles are deviated by the magnetic force and retained on the channel walls. (b) Downstream of the magnets $\vec{F}_{mag}$ becomes negative and can deviate the particles towards the magnets.

The magnetic field intensity increases linearly in the y-direction due to the symmetric field configuration (Figure II.11). As a result, the magnetic force on the particles decreases to attain its lowest value in the channel x-axis where the flow velocity should reach its maximum value (see Figure II.9.a). The microparticles are weakly held up and the viscous drag force acting on them may easily exceed the magnetic force when the flow rate increases. In short, the microparticles are carried away as long as the drag force is higher than the magnetic force. The particle path depends on its location whether it is in or out the magnetic trap area.

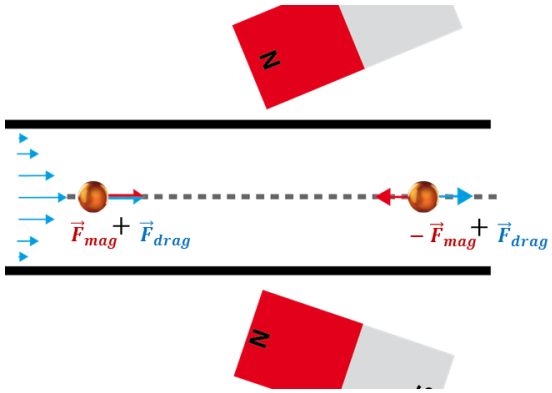

Figure II.11: Schematic illustration of the forces acting on the particles around the magnets ($\vec{F}_{mag}$ and $\vec{F}_{drag}$). The particles close to the middle of the channel experience a weak $\vec{F}_{mag,y}$ (in y-direction) due to the symmetric field. At upstream end of the permanent magnets, $\vec{F}_{mag,x}$ and $\vec{F}_{drag,x}$ are positive, whereas at downstream, $\vec{F}_{mag,x}$ becomes negative and has to overcome the $\vec{F}_{drag}$ to retain the particles.

e. Hydrodynamic behaviour of the plug

In this section, we propose a detailed hydrodynamic study of the plug, combining measurements of flow-pressure characteristics and microscopic observations.

i. Experimental procedure

The microfluidic set-up is depicted in Figure II.12. We investigated the hydrodynamic response of the plug to an applied pressure. For this purpose, we chose to control the fluid flow in the microchannel by using a pressure-driven flow controller, the MAESFLO that uses a pneumatic pressurization of reservoirs.

This system allows a dynamic control of the pressure in the reservoir and thus provides a good stability and with short response times, typically around 100 ms. More details about the pressure controller running are given in appendix (3). The MAESFLO software enables a full and independent control of the pressure in the inlet and outlet as well as real time flow rate monitoring in the microfluidic system, thanks to FLOWELL sensors integrated at upstream and downstream of the chip. Both sensors can measure positive and negative flow rates (according the flow direction) ranging between 0 and $\pm 7\ \mu L/min$ and between 0 and

$\pm$ 50 $\mu L/min$ respectively (1% flow rate accuracy). In our experiments, we used 0 to 1 bar or 0 to 25 $mbar$ pressure regulator (1% pressure accuracy). The inlet of the chip is connected to two reservoirs via a rotary valve. All connections were made in PEEK[9]tubing's in order to prevent any pressure oscillations.

Two different types of carboxylic acid (COOH-) coated superparamagnetic microparticles manufactured by Invitrogen (Dynabeads®) have been used to characterize the system: particle diameters was 1.05 μm (*MyOne*^{TM})[10] and 2.8 μm (*M-270*)[11] respectively. These microparticles were chosen due to their surface charge (i.e. a high negative net charge at neutral pH) which minimizes uncontrolled aggregation by electrostatic repulsion.

Microparticle suspensions were washed according to the manufacturer's specification and were then suspended in phosphate buffer saline (PBS) with 0.1% bovine serum albumin (BSA) to avoid the microparticles aggregation. Suspensions, with a 2 mg/mL solid content, were used for these experiments. Optical microscopy was used to visualize the colloidal suspension during the experiment and track the trajectory and streams of particles in the magnetic plug.

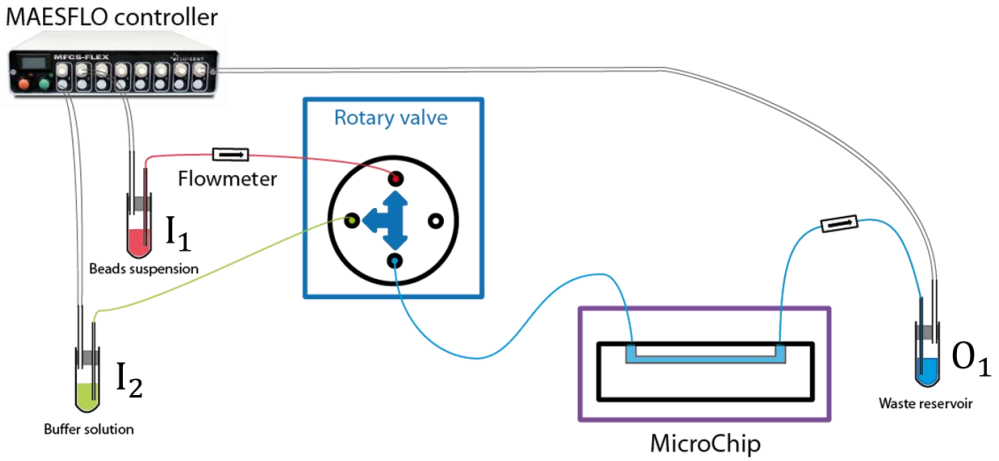

Figure II.12: Schematic set-up of microfluidic device, both flowmeters are used to measure the flow rate, one varying from 0 to 7 $\mu L/min$, placed before the microchip and the other varying from 0 to 50 $\mu L/min$, and placed after the microchip.

Before starting an experiment, the waste reservoir is prefilled with buffer solution. The system is then filled with buffer and rinsed while applying a 1 bar pressure to remove the bubbles trapped in the microchannel that would in the best case, induce instabilities during the pressure/flow measurements or in the worst case, damage the magnetic plug by pulling away the particles from the magnetic trap. I_1 and I_2 reservoirs are refilled with a microparticles

[9]Material exhibiting an excellent rigidity and chemical resistance.
[10]http://tools.invitrogen.com/content/sfs/manuals/650%2011_12(rev006).pdf
[11]http://tools.invitrogen.com/content/sfs/manuals/143%2005D_06D%20Dynamicroparticles%20M720%20Carboxylic%20Acid(rev004).pdf

suspension and a buffer solution, respectively (see Figure II.12). By applying a large pressure range in the microfluidic system via I_2 reservoir, we check that the system is free of bubbles and leaks, in monitoring the pressure and the flow rate stability. After this preliminary step, the microfluidic system remains closed during the whole experiment. The microparticle suspension is injected at a pressure around $50\ mbar$. Subsequent to plug formation, the rotary valve is switched to the I_2 reservoir.

The hydrodynamic characteristics of the plug can be studied through the monitoring of pressure vs. flow behaviour and observing the system using a transmission stereomicroscope.

ii. Hydrodynamic characterization of the plug

The following experiments were chosen to illustrate the hydrodynamic behaviour of plug (microparticles bed). Among the available experimental parameters, we investigated the influence of the microparticles amount, their diameter and the gap length on the plug.

Particle bed behaviour

Herein, the hydrodynamic plug behaviour was investigated using a plug made of$1\ mg$ of $\emptyset\ 1.05 \mu m$ microparticles. The experiment has been performed in a PDMS microchannel of $1\ mm$ wide by $250\ \mu m$ high and $2\ cm$ long with a fixed gap length of $2\ mm$.

The hydrodynamic response of the microfluidic system in presence of the plug is shown in Figure II.13. This response is given by the downstream flow rate measure when an upstream pressure is applied. This result, coupled with an optical observation, reveals three plug regimes which can be separately considered in this order:

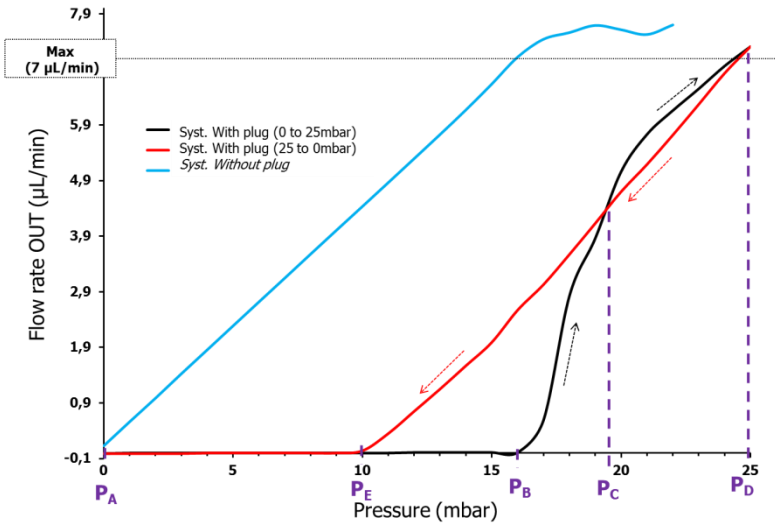

Figure II.13: Curves representing the flow rate ($\mu L/h$) vs. the pressure ($mbar$) in a PDMS chip for 1 mg of trapped $\emptyset\ 1.05\ \mu m$*MyOne* particles. The gap between magnets was set to $2\ mm$.The pressure increase was set to 1 mbar every minute. The blue curve is the reference of system (the maximum level of the sensor is $7\ \mu L/min$). The black curve is the behaviour of the plug when the pressure is gradually increased and conversely for the red curve.

(i) Packed-bed: when first increasing the pressure from zero (point A) up to 16 $mbar$, no measurable flow rate could be detected by the sensor. Optical observations only show that the whole magnetic plug remains in a packed-bed regime, but it is gradually shifted downstream in the magnetic trap. We believe that in this regime, the plug behaves as a packed and porous material with a high hydrodynamic resistance only allowing liquid to flow through by percolation.

(ii) Expanded-bed: when the pressure exceeds the threshold setting of 16 $mbar$ (point B), a dramatic change in the slope is observed. The pressure is then sufficiently high to counterbalance the hydrodynamic resistance of the plug. At this stage, a fracture occurs within the plug and propagates along the x-axis of the plug, causing the bed to expand in volume as the particles move away from each other, although they are still confined in the plug.

(iii) Fluidized-bed: At 20 $mbar$ (point C), a kink is observed, beyond which the flow rate increases linearly with the applied pressure. We can notice, during this regime that the slope of the curve is the same than that of the reference curve (hydrodynamic response of the system without plug). This means that the plug introduces a constant pressure drop, which seems to be independent from the flow rate. The bed is said to be fluidized and will exhibit fluidic behaviour.

The backward path (DEA) is obtained by gradually decreasing the pressure (see red curve). The flow rate decreases linearly with the pressure, remaining parallel to the reference curve and causes the narrowing of bed. When point E is reached, the pressure is too low initiate particle in flux and the bed closes up. It is interesting to notice that pressure at point E is significantly lower than the pressure at point B (16 $mbar$ compared to 10 $mbar$). This clearly means a hysteretic behaviour of the plug. In an attempt to understand the origin of the observed hysteresis, we investigated the influence of the microparticle amount involved in the plug

It is important to mention that, in the fluidized regime, the plug density is not homogeneous. Indeed, as can be seen on Figure II.15, a “fracture” is created in the centre of the channel. This is mainly due to the non-uniformity of the magnetic field (see Figure II.8). This mechanism occurs in the centre of the channel, where the magnetic confinement forces are minimal. In this region the pressure is sufficient to overcome the cohesive forces within the plug. The fracture propagates along the plug. When reaching the rear edge of the plug, the fluid flows in the channel that was created. The flow rate increases suddenly in the device. It is important to notice that, even if it is influenced by the flow rate, the size of the fracture remains very small as compared to the size of the bed and only a small fraction of particles are involved in the fluidisation process.

Obviously this fracture behaves as an opened microchannel through which the liquid is free to flow while ensuring the circulation of the microparticles throughout the plug as long as the

dragging force is stronger than the magnetic one (see Figure II.14). However, at the rear edge of plug, the flow rate decreases and the flow is deflected to the y-direction, the particles are not anymore located on the x-axis. They will undergo the magnetic force which diverts them towards the plug in the channel walls vicinity.

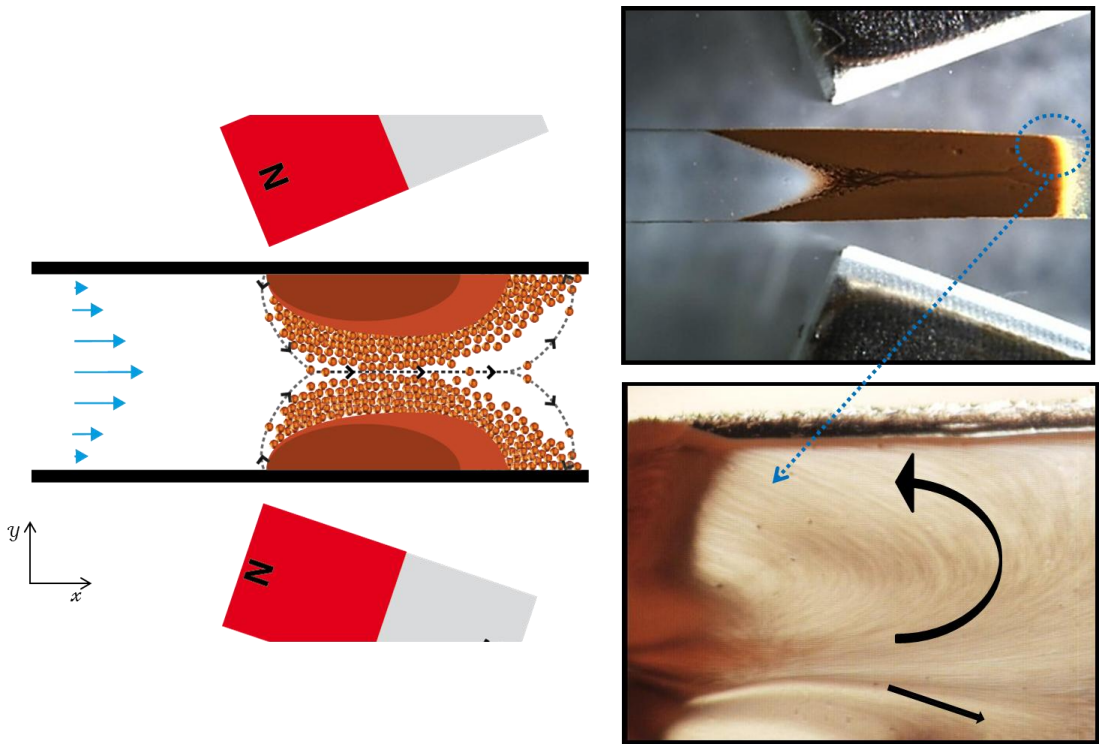

Figure II.14: (a) Microparticle motion within the plug. The areas with different packings are represented by different colour. (b) Plug picture shows the microparticles recirculation.

Influence of microparticle amount

In the following case, the plug is formed from 0.5 mg of particles. The response of the plug is illustrated in Figure II.15. The shape of the curve is substantially the same than previously obtained from 1 mg of particles. As expected, the pressure threshold (8 vs. 16 $mbar$) is shifted down because of a lower particle amount. We observe in this case a more constricted hysteretic loop which could be explained in two different ways:

(i) At high flow rates (3 $\mu L/min$), the plug expands beyond the magnetic trap. As a result, all the microparticles, out of this area, detach from the plug and are dragged away by the liquid. Experimentally, the plug size cannot exceed 3 mm length in packed-bed regime which corresponds to 0.3 mg *of particles*, otherwise a part of particles located at the edge of the plug are gradually dragged away during the fluidized-bed regime. For this reason, the released amount of microparticles is very low compared to the 1 mg plug containing

(ii) Secondly, the microparticles self-reorganize during each regime and form a less packed bed than the original one after flow stoppage. This means that the plug is less resistant to the flow, which shifts down the threshold pressure.

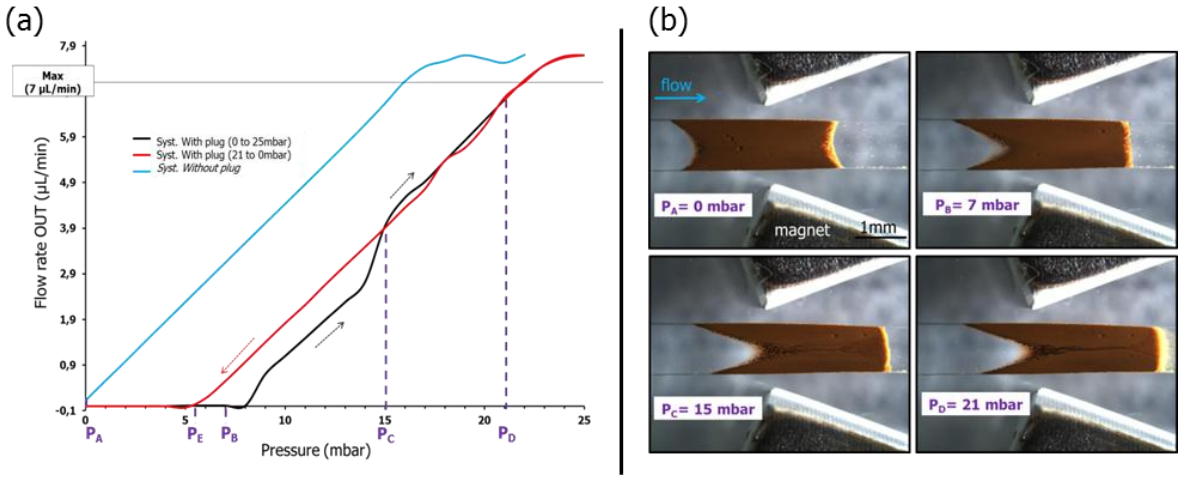

Figure II.15: (a) Plot representing the flow rate ($\mu L/min$) vs. the pressure ($mbar$) in a PDMS chip for 0.5 mg of trapped $\emptyset$ 1.05 $\mu mMyOne$ particles. The blue curve is the reference of system. The black curve is the behaviour of the plug when the pressure is gradually increased and conversely for the red curve. (b) Plug behaviour at different applied pressures.

Influence of the gap between the magnets

As expected from numerical simulations of the magnetic field distribution, shortening the gap length induces an increase of both the intensity and gradient of the magnetic field, thus leading to higher confinement forces and a more efficient particle trapping (see Figure II.16).

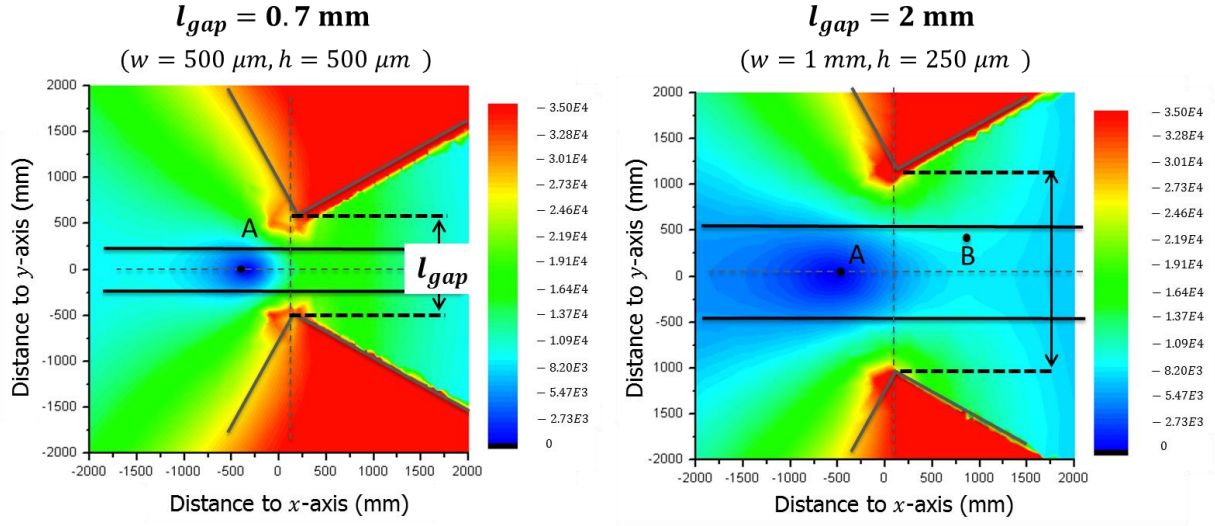

Figure II.16: Magnetic field intensity (T) as reveal by simulation for gaps of 0.7 $mm$and 2 mm.$w$and$l$ are the width and the height channel.

In the following, we performed the same experiment than previously described using a 0.7 mm gap and 0.25 mg of ∅ 1.05 μm microparticles. The particle amount involved in this experiment was chosen accordingly to the observations done in the previous paragraph (0,3 mg of particle has been identified as a threshold value to avoid particle loss in the range of pressure investigated).

*Note: Both microchips exhibit a same volume for a same channel length (*0.75 mm^3*)*

The hydrodynamic response of this plug is shown in Figure II.17. We observe a very similar behaviour as presented before. Nevertheless, above the threshold pressure (10 $mbar$); the plug switches directly to a fully fluidized regimewith a linear dependence of the flow rate as a function of the applied pressure. This value is close to the one found in the previous experiment (Figure II.15). This result show clearly the influence of the magnetic field intensity: although the particles amount is only half of that used previously, the confinement forces are sufficient to keep the pressure threshold almost constant.

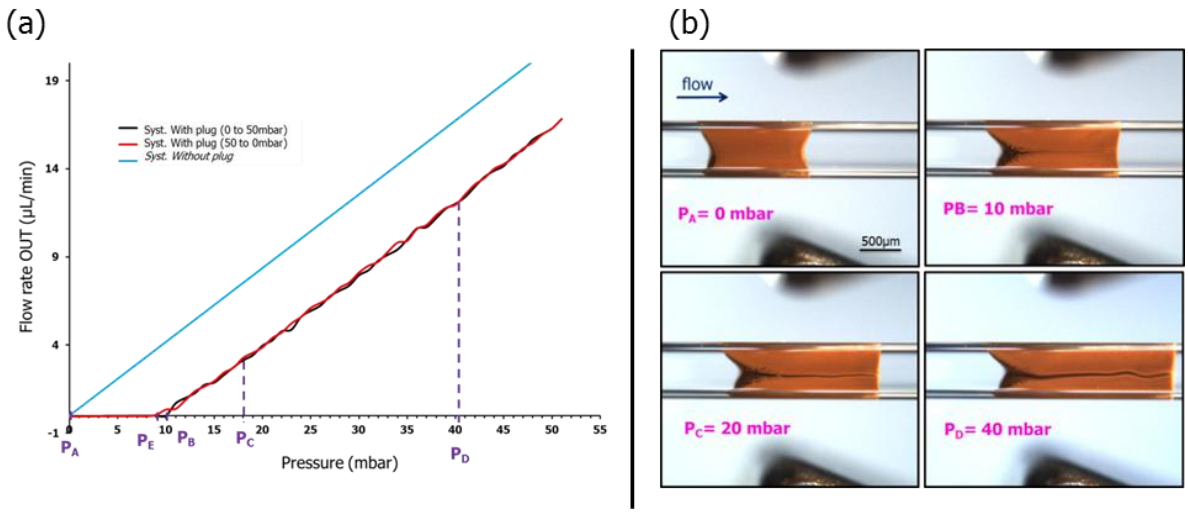

Figure II.17: (a) Plot showing the evolution of flow rate out vs. the pressure for an amount of microparticles of 0.25 mg (∅ 1.05 μm). (b) Plug aspects at different applied pressures.

Influence of the microparticle size

The last parameter to be investigated was the microparticle size. We focused our attention in the comparison between ∅ 1.05 μm*(MyOne)* and ∅ 2.8 μm*(M-270)* particles. The Figure II.18 shows the hydrodynamic characterization of a 0.25 mg plug composed of ∅ 2.8 μm particles. The experiment was carried out in a 500 μm glass capillary with a gap of 700 µm. We observe in the plot that the threshold pressure is shifted down to 4 $mbar$. This result can be easily explained: On one hand, *M-270*particles (even if they are bigger) exhibit a magnetization similar to that of *MyOne* particles. On the other hand, *M-270*particles are much sensitive to drag forces as their diameter is almost 3 times higher than for *Myone* particles. *M-270*particle have thus larger magnetophoretic mobility. In addition, due to their lower mass

magnetization than *MyOne*, they areless sensitive to magnetic confinement forces and that the plug offers a lower resistance against the flow [135].

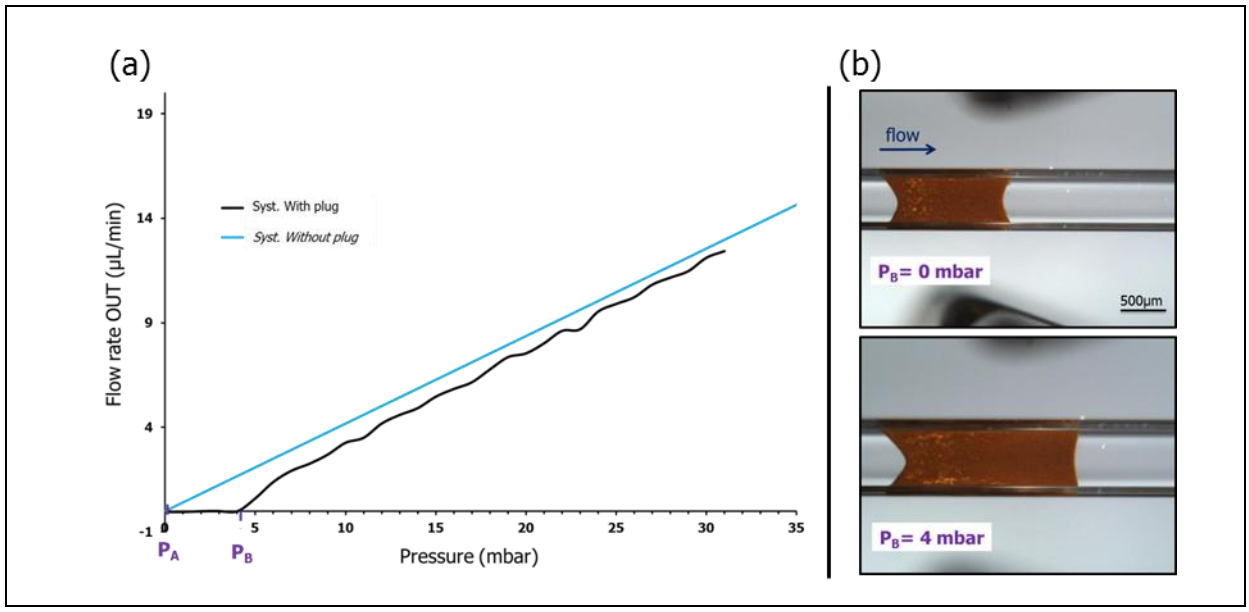

Figure II.18: (a) Hydrodynamic response of a plug containing 0.25 mg of *M-280 particles*. (b) Plug aspects at different applied pressures.

f. Conclusion

We have seen that none of the experimental parameters that were investigated in this study could have a significant influence on the plug behaviour, in particular, on the creation of a fracture in the fluidized regime. As shown through numerical simulations, the geometry of the device is characterized by symmetry axis in the centre of the microchannel. Whereas the magnetic confinement force exerted by the two magnets is strong enough to trap microparticles and to maintain the plug stability while the liquid is flowing, this geometry induces an inhomogeneity of the magnetic force, with minimum values along the microchannel x-axis. In addition to the parabolic profile of the flow velocity in the channel which induces a maximum drag force along the channel x-axis, this magnetic field inhomogeneity is also responsible for the formation of the observed fracture.

4. Second device generation: towards an integrated fluidized bed

a. Motivation

Both the concepts of packed and fluidized bed are commonly used in chemical engineering operations. They are widely involved in industry for mixing solid particles with gases or liquids to obtain vigorous agitation of the solids in contact with the fluid. This process enhances the fluid-solid contact per unit bed volume to achieve a high level of intermixing (e.g. as fluidized bed reactor, or fluidized bed combustion…etc.) causing rapid mass and heat transfer, and particularly in the case of fluidized bed increasing reaction efficiency and kinetics [147], [148].

Compared to packed bed, fluidized bed offers clear advantages:

(i) higher mixing efficiency and temperature homogeneity.

(ii) bed plugging and channeling are usually minimized due to the movement of the solids.

(iii) operating conditions require lower pressure drops and allow higher flow rates.

(iv) the systems provide a low interparticle diffusion resistance.

Due to these advantages fluidized beds have extensive industrial applications as compared to packed beds. Originally, fluidized beds were developed for catalytic cracking in the petroleum industry (a fluidized bed of catalytic particles was generated to obtain that intimate contact with the fluid). Nowadays, they become a versatile fluid-solid intermixing device in a broad range of applications for chemical, biochemical and even metallurgical industries.

The objective of this paragraph is to show that the concept of fluidized bed can be integrated within microfluidic devices and might solve most of the limitations that were pointed out for the first device design. We will first focus our attention on the general concepts of conventional fluidized bed using gravity as a confinement force and discuss the effects of downscaling on fluidization. Then, we will introduce the working principle of the magnetic based system. We have developed and present a careful study of its hydrodynamic behavior and magnetic characteristics. We will finally conclude by discussing the integration and the operating conditions in microfluidic devices.

b. Fluidized bed: some basics

A typical packed bed is a vertical cylindrical column that is filled with a suitable packing material. In such device, a liquid is injected upwards through the packed bed. The

transition between packed and fluidized bed relies on the competition between viscosity and gravity. Indeed, when the fluid drag force is equal to the bed weight, the particles no longer stay in contact with each other: this corresponds to the point of incipient fluidization (or fluidization point). At this point, taking into account the whole particle bed, the drag force exerted on the particles, matches the bed pressure drop (gradient) induced by the gravity.

As the fluid flow increases, the fluidized bed expands vertically while the pressure drop remains substantially constant. During this process, the bed porosity (or the fractional void volume) increases with the bed size thus locally reducing the viscosity effects in the bed. A new equilibrium point is found when the hydrodynamic drag forces along the expanded bed equal the bed net weight.

Figure II.19 shows that three regimes can be distinguished: i) Packed bed: it corresponds to a solid substance bed, where particles are kept at close packing by gravity force. ii) Fluidized bed: an injection of the pressurized fluid through the solid is sufficient to lift particles and the bed reaches a steady state in which the flow resistance equilibrates gravity. iii) Finally, when the drag force of the fluid exceeds gravity even at vanishing density, particles escape and the bed is progressively destroyed.

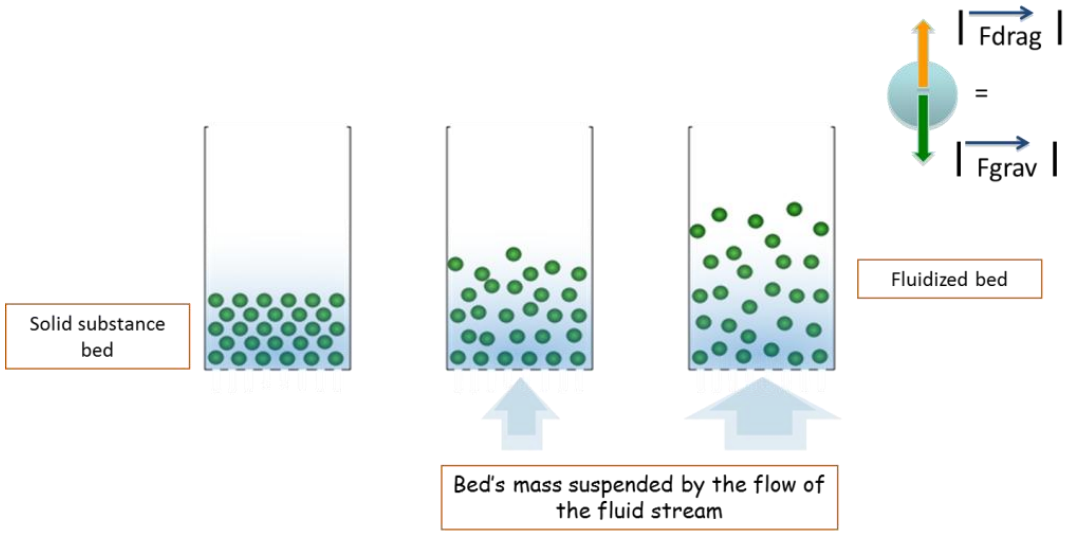

Figure II.19: Schematic representation of process of fluidized bed.

c. Influence of the bed porosity on the fluid flow

The fluid flow through the bed is Q (m^3/s) and the bed cross sectional areais A (m^2). The superficial velocity corresponding to an empty tube configuration U_0 is thus given by:

$$U_0 = \frac{Q}{A}$$

Equation 14

The presence of particles within the bed will reduce the area available for the fluid flow. The velocity within the bed *U*, also called interstitial velocity, is thus higher than U_0. Its value depends on the volume fraction of particles C occupying the bed and more exactly on the free space also named voids available in the bed for the liquid to flow through. The void fraction is called porosity ε. We thus have the following relation:

$$\varepsilon + C = 1$$

Equation 15

To consider the porosity as an isotropic property of the bed, we can define the interstitial velocity *U* as:

$$U = \frac{U_0}{\varepsilon}$$

Equation 16

Clearly, the resistance to fluid flow through a porous medium is related to the amount of particle present or porosity. We thus have to consider the potential energy losses from the fluid due to viscous drag.

In opened channels, Reynolds number Re can be used to describe the balance between viscosity and inertia:

$$Re = \frac{l\rho_f U_0}{\eta} = \frac{lU_0}{\nu}$$

Equation 17

where$l$ is a characteristic dimension of the system, η is the dynamic viscosity of the fluid, ρ_f, the density of the fluid(kg/m^3)andνs the kinematic viscosity of the fluid (m^2/s).

In porous medium, we will rather consider the modified Reynolds Re^*numberto determine the flow regime of the fluid in a bed:

$$Re^* = \frac{\rho_f U_0}{(1-\varepsilon)\eta S_v} = \frac{U_0}{(1-\varepsilon)\nu S_v}$$

Equation 18

whereS_v is the specific surface area per unit volume that is defined as the ratio of the cross section area of the particle divided by its volume. Taking into account a particle with a diameterd_p, we obtain:

$$S_v = \frac{\pi {d_p}^2}{4/3\pi {d_p}^3} = \frac{6}{d_p}$$

Equation 19

Conceptually this number still represents the balance between inertial and viscous forces. It provides a way to assess the conditions where the inertial effects become predominant in a porous media.

Conventionally, the applied thresholdRe^* value, indicating a significant level of turbulence level is 2 whereas level of turbulence for the fluid flow number Re is around 2000[149].

d. Darcy's law: pressure drop across the bed

The Darcy's law is used to describe the pressure drop ΔPacross a bed as a function of the flow rate dV/dt. It considers a simple model taking into account the geometrical and viscous parameters that influences the flow resistance across the bed:

$$\frac{\Delta P}{L} = \frac{\eta}{k}\frac{dV}{dt}\frac{1}{A}$$

Equation 20

where$k(m^2)$ is defined as the permeability of the bed for a volume $V(m^3)$ of fluid flowing across the bed in a time $t(s)$ and L is the length of the bed.

The Kozeny-Carman equation is usually preferred to describe particle beds. It derives from the Hagen-Poiseuille equation and is used to describe the bed porosity: it considers the bed as a porous medium composed of a defined$N$ number of circular channels in parallel having a radius r and a length $L$where laminar flow takes place. Using this model, the Kozeny-Carman equation gives the evolution of the pressure drop as a function of the fluid velocity

$$\frac{\Delta P}{L} = \eta\left[\frac{K(1-\varepsilon)^2 {S_v}^2}{\varepsilon^3}\right]U_0 = \eta\left[\frac{K(1-\varepsilon)^2 {S_v}^2}{\varepsilon^3}\right]\frac{dV}{dt}\frac{1}{A}$$

Equation 21

where$K$ is the Kozeny constant.

Note: In many instances the Kozeny constant as a value close to 5 (experimental observation) but one has to remind that $K = f(\varepsilon)$.

The permeability k can be written as following

$$k = \eta \left[\frac{\varepsilon^3}{K(1-\varepsilon)^2 {S_v}^2} \right] U_0$$

Note: In our case, since the particles spontaneously organise into 1D chains in parallel to each other, S_v can be better expressed as $S_v = 4/d_p$, that is more appropriate to describe magnetic chains.

Equation 22

This equation shows that the permeability *k*is dependent of the bed porosity and the specific surface area within the bed. Indeed the viscous drag forces on the particles in the bed scale up with the bed surface area thus causing the permeability to decrease. One can note that the Kozeny-Carman equation is a subset of the Darcy's law.

Using the definition ofS_v, it is possible to provide a version of the equation in terms of particle size

$$\frac{\Delta P}{L} = \eta \left[\frac{36K(1-\varepsilon)^2}{\varepsilon^2 {d_p}^2} \right] U_0$$

Equation 23

Note: This equation assumes a homogeneous and well defined size for the particles in the bed. In order to consider the size distribution of particles,d_p must be replaced by the Sauter diameter d_{Sv} in the last equation.

As an illustration, using 2.8 μm particle in water with a fluid flow $U_0 = 1\, mm/s$, and a porosity $\varepsilon = 0.5$, we obtain $Re^* \approx 10^{-3}$. This value gives a confirmation that all the experiments described in this manuscript satisfy$Re^* < 2$. This clearly means that the viscosity effects are still predominating and the Darcy's and Kozeny Carman laws can be used to describe our system.

Note: For devices where $Re^* > 2$, Carman and Ergun correlation may be considered instead of Kozeny-Carman equation [149–151].

e. Pressure-flow relationship in fluidized bed: Minimum fluidization velocity

In conventional fluidized bed devices, gravity is used to counterbalance the drag forces induced by the liquid flow and maintain the bed stability. The Figure II.20 shows the typical pressure flow dependence in such system.

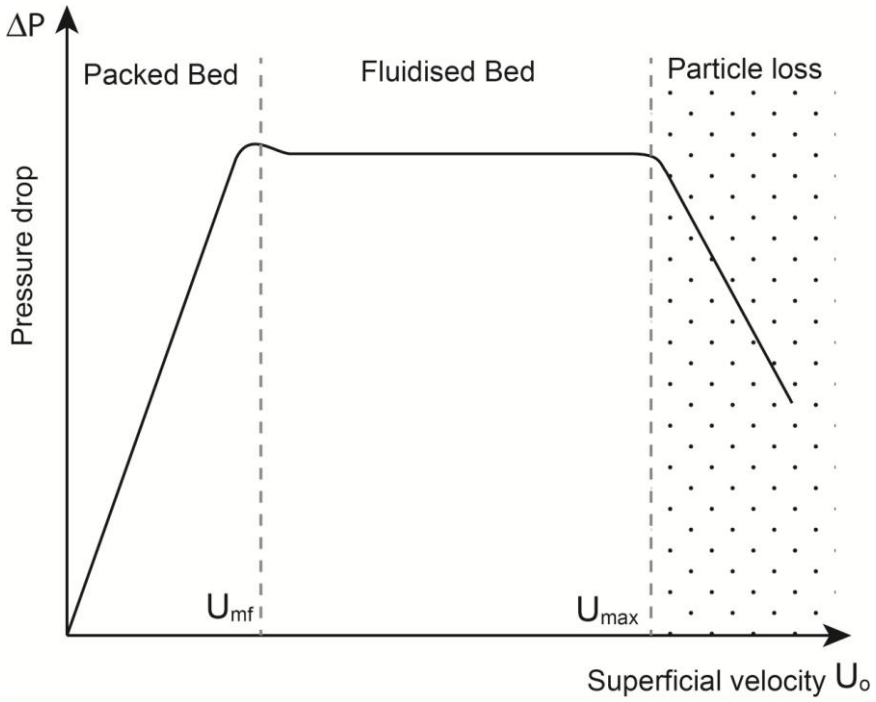

Figure II.20: Typical pressure-flow behaviour in a gravity based fluidized bed

As mentioned before, three different regimes can be distinguished. Below a certain velocity, the bed is in a packed state. In this regime, the flow velocity is not sufficient to lift particles. At low Reynolds, the pressure drop across the bed is given by the Kozeny-Carman equation, as both L and ε are fixed, the pressure drop increases linearly with U_0. In other words, the pressure drop is imposed by the hydrodynamic resistance of the packed bed which behaves as a porous stable material.

When the superficial velocity reaches the minimum fluidisation velocity U_{mf}, the drag forces exerted on the particles are sufficient to counterbalance the gravity forces. As a consequence, the pressure drop created by the bed can be related to weight of the bed solid content. The upward force on the bed owing to the pressure is $F_b = A\,\Delta P$. The total volume of particles can be writtenas a function of the proportion of particles presentin the bed$V = (1-\varepsilon)AL$. Taking into account the upward buoyant force $F_b = \rho_f(1-\varepsilon)AL$ and the downward gravitational force is $F_g = \rho_p(1-\varepsilon)AL$, it is thus possible to write:

$$\Delta P = (1-\varepsilon)\left(\rho_p - \rho_f\right)Lg$$

Equation 24

where$\rho_p$and ρ_f are the particle density and the fluid density respectively and g is the gravitational acceleration.

At the point of incipient fluidization, the drag force equals the bed weight. Combining the latter equation with Darcy's law, it is thus possible to write:

$$U_{mf} = \frac{k}{\eta}(1-\varepsilon)(\rho_p - \rho_f)g$$

Equation 25

where U_{mf} is the minimum fluidizing velocity. It is important to notice that U_{mf} is a superficial velocity (velocity out of the bed) and not an interstitial velocity (within the bed).

Finally, for velocities above the threshold value U_{max}, gravity is not sufficient to counterbalance the fluid drag force and the particles are swept from the container. As the void fraction increases, the pressure drop decreases and the bed ceases to exist.

f. Magnetically assisted fluidized bed

As described just before, the concept of fluidized bed brings intriguing advantages in comparison with the first device generation presented in the first part of this chapter. Indeed, as it offers a homogeneous distribution and circulation of particles in the bed it should solve the efficiency issues that we pointed out in the first part of this chapter. From that point of view, such systems would be appropriate to extraction or capture processes in microfluidic devices.

Whereas many examples of packed bed have been reported in literature for microfluidics applications [95], [98], [152]and original strategies were proposed in literature to improve particle mobility [122], [131]. The integration of the concept of fluidized bed in miniaturized devices was not reported yet, to our knowledge.

Indeed when scaling down the dimensions of a fluidized bed device below the millimeter length scale, and thus the dimensions of the particles down to a few micrometers, it turns out that gravity is no longer sufficient to ensure bed stability. Indeed whereas the hydrodynamic drag forces scale with the radius r_p of particles, the gravity force scaleswith r_p^3. This causes a significant dependence of gravity, driven fluidized beds on particle volume.

As anumerical example, the calculation of gravity force experienced by a 4.5 μm magnetic particle (e.g. Dynal) in a vertical liquid flow of 1 mm/s mean velocity is:

$$|\overrightarrow{F_g}| = \frac{4}{3}\pi r_p^3 \rho_p \, g = 9{,}7.10^{-15} N$$

The drag force induced on the same particle is given by the Stockes equation:

$$|\overrightarrow{F_d}| = 6\pi\eta r_p \vec{v} = 4{,}24.10^{-11}\ N$$

This result shows clearly that gravity forces are not sufficient (three decades lower) to compensate for the fluid drag and that, even in the case of magnetic particles, the material density is too low to compensate the low particle volume.

As mentioned in the first part of this chapter, the use of magnetic microparticles gives the opportunity to access to higher handling forces, typically around $10^{-11}\,N$ that would sufficient to ensure particles confinement in device.

In the first device generation presented in this chapter, magnetic forces were successfully used to confine particles in a microchannel with flow rates up to $2\,mL/h$. However, we showed that the device design was inducing spatial inhomogeneity in the magnetic field distribution and thus in the particle distribution.

In order to compensate for these limitations and to mimic conventional gravity based fluidized beds, we proposed a new device concept as described inFigure II.21.

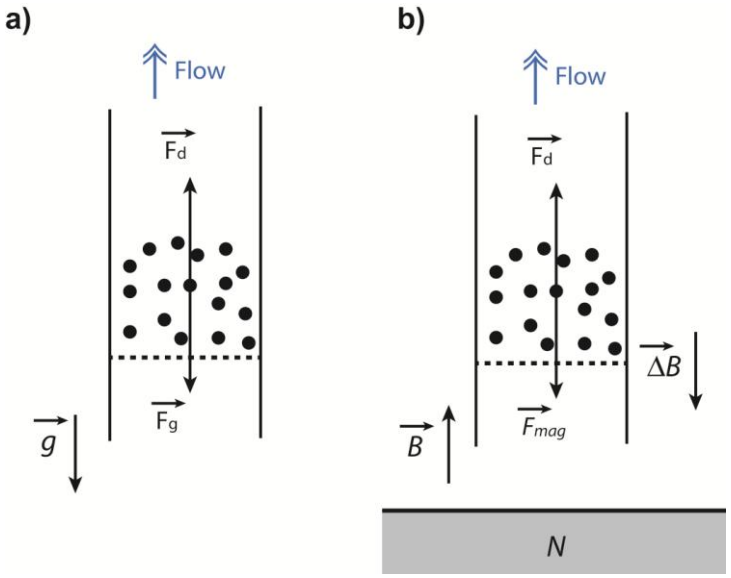

Figure II.21: a) Illustration of a conventional fluidized bed system: downward gravitational forces are involved to stabilize the bed and compensate for drag force. b) Magnetically based fluidized bed: gravitational forces are replaced by magnetic forces.

In our approach a magnetic force is used to mimic the influence of gravitational forces: the magnetic field orientation is homogeneous in the channel but a magnetic field gradient is generated downward for instance using a permanent magnet.

Permanent magnets are advantageous as they offer high magnetic field intensity value. However, it is important for the lateral dimensions of the magnet to be significantly higher than the size of the channel so that the lateral component of the magnetic forces is close to 0. In this system, magnetic forces compete with drag forces to keep particles confined in the channel.

This approach is quite different from strategies that use magnetic confinement using multipolar magnets or coils [122], [131] that have shown to significantly improve particle mobility but that still remain limited in terms of particle content.

Note: As explained before, a balance must be found between magnetic forces and drag forces. All the results that will be described in this paragraph were obtained with 2.8 µm superparamagnetic particles from Dynal.

g. Minimum fluidisation velocity

In this new system, the Kazeny-Carman equations that describe the pressure drop across the bed according to the superficial flow velocity U_0, to the bed porosity ε and length L remain valid.

However, it is obvious that the equations giving the minimum fluidising velocity U_{mf} are not applicable to our system as we have now to consider the sum the magnetic forces induced on each particle instead of gravity. We thus have to develop our own set of equations:

As described previously, the magnetic force applied on a particle can be written as following:

$$\vec{F}_{mag} \approx V_p \frac{\Delta\chi}{\mu_0} (\vec{B}.\nabla)\vec{B}$$

Equation 26

To consider the whole bed, and assuming that the magnetic field intensity is a function of the distance l to the magnet, we can write:

$$\vec{F}_{mag} \approx \int_0^L N_l V_p \frac{\Delta\chi}{\mu_0} (\vec{B}.\nabla)\vec{B}$$

Equation 27

whereN_l is total number of particles in an elementary volume defined as

$$N_l = A_{x=l} dl$$

$A_{x=l}$being the cross section area of the bed at a distance $x = l$ from the inlet.

*Note: Interactions between particles are neglected in*Equation 7.

Assumingthat the porosity ε is homogeneous all along a fluidized bed with a section area $(A = f(l) = A_{x=l})$, N_l can be written as a function of :

$$N_l = \frac{(1-\varepsilon)\, dl\, A_{x=l}}{V_p}$$

Equation 28

We thus obtain the simplified equation for the elementary magnetic force on a single particle

$$d\vec{F}_{mag} = N_l V_p \frac{\Delta\chi}{\mu_0}(\vec{B}.\nabla)\vec{B}$$

Equation 29.a

By integrating $d\vec{F}_{mag}$on the whole bed volume of length L, we obtain the total magnetic force on the bed:

$$d\vec{F}_{mag} = \frac{\Delta\chi}{\mu_0}(1-\varepsilon)\int_0^L A_{x=l}(\vec{B}.\nabla)\vec{B}\cdot dl$$

Equation 29.b

The resulting pressure is $\Delta P_{mag} = \frac{\|\vec{F}_{mag}\|}{A_{x=L}}$

Equation 29.c

An estimation of the incipient fluidization velocity can be written as:

$$U_{mf} = \frac{k}{\eta}\frac{\Delta P_{mag}}{L}$$

Equation 30

5. Microchip based fluidized bed

The investigations done in the first part of this chapter have enabled to understand more deeply the behaviour of the plug and have shown that the magnetic field homogeneity is critical to ensure a uniform particle recirculation throughout the plug body.

It seems that the concept of fluidized bed offers intriguing performances for the implementation of beads capture device and may solve the problems of particle recirculation homogeneity that we pointed out. In this paragraph, we will propose an innovative strategy that combines magnetic forces and microfluidic channels to implement a miniaturized fluidized bed. We will first focus our attention on the influence of the magnetic flied distribution and microchannel geometry. Finally, we will propose a quantitative investigation of the bed behaviour.

One of the main motivations is to generate a homogeneous magnetic field distribution in the device. As we suggested before, a single magnet aligned along the main channel axis might provide an efficient solution. In such configuration, the magnet generates a uniform magnetic field parallel to the channel midline (x-axis) thus avoiding the drawbacks that were encountered with two magnets placed on both sides of the channel.

Based on this assumption, we investigated the creation of fluidized beds in several microchannel designs. The first geometry is shown in Figure II.22. It consists in a 2 cm long channel with a constant 100 μm height. The channel composed of part that linearly widens from 50 μm up to 1 mmlike a wedge and then by a straight channel.

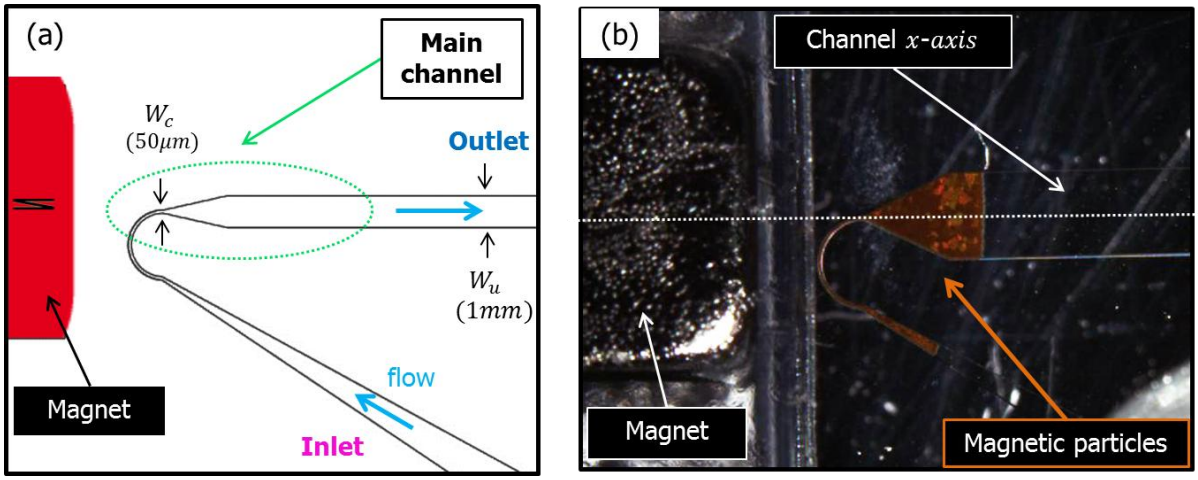

Figure II.22: (a) General approach allowing a uniform magnetic field in the cross-sections of the channel. (b) Picture of the microchip containing magnetic particles (plug).

Dynal ∅ 2.8 μm particles were introduced in the device through a 50 μm curved injection channel. As shown in Figure II.22, the microparticles are confined in the channel portions that are located close to the magnet. The straight shape of rear edge of the bed confirms the uniformity of the magnetic field in the channel cross-section.

The investigations of the device hydrodynamic behaviour are illustrated in Figure II.23. The first image shows the bed in the packed state, for $P = 0\, mbar$. When injecting a buffer solution (PBS/BSA) at a constant pressure of 50 $mbar$, the bed switches to a fluidized regime. A fluid flow is observed in the centre of the bed together with a particle influx. This first result is the first demonstration of fluidisation. However, careful observations revealed that only the microparticles located nearby the channel midline are able to move freely, while the others are still packed on the channel sidewalls. Fluidisation occurs only in the centre in a region that gradually widens from 50 μm (channel inlet) up to 500 μm at the rear bed edge.

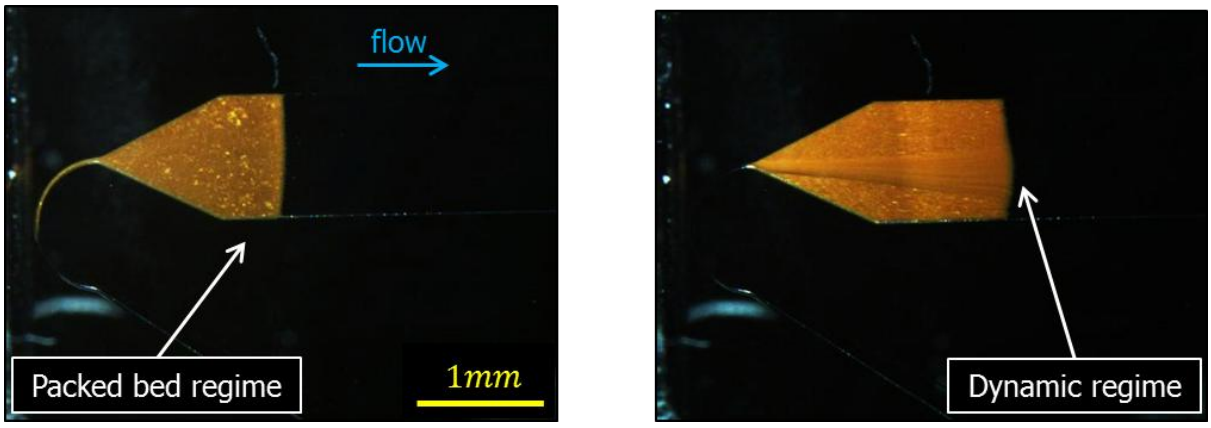

Figure II.23: Optical images showing the plug in packed and dynamic regime ($P = 68\,mbar, Q = 14\,\mu L/min$).

Knowing that the microparticle motion requires the drag force overcomes the magnetic force, the obtained results might be explained by taking into account both the flow velocity profile and the cohesive forces between particles in the bed.

The flow enters the bed through the injection channel that has a very the narrow size ($50\,\mu m$). The flow velocity in this region of the channel is sufficient to counterbalance magnetic forces. Fluidisation occurs in the injection area but due to the cohesive force of the bed, the spreading of the flow field is restricted in the centre part of the bed. This can explain why only the microparticles located nearby the channel midline are able to move in the bed, while the others are still packed on the channel sidewalls. A fracture is thus created in the centre of the bed allowing the fluid to flow through. In this region, these particles are dragged to the rear edge of the bed and finally they move back via the sidewalls because of the magnetic forces.

Based on these observations, we search out solutions to distribute more uniformly the flow in the channel cross-section. For that purpose, we investigated several designs of microfluidic manifolds. This approach relies on the integration of branching structures that provide a high number of fluid injection sources along the channel cross section. Inspired by the work of Murray and al. (Murray's Law gives the relationship between the diameter of the parent vessel and the optimum diameters of the daughter vessels) [153], [154]. We investigated several manifold designs.Figure II.24 and Figure II.25 shows two examples of them.

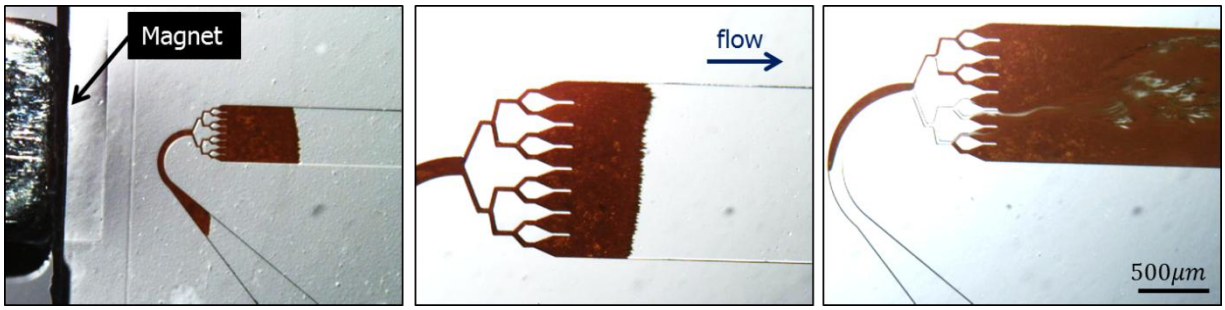

Figure II.24: Microfluidic manifold designed according to biomimetic rule. Plug pictures in packed bed and dynamic regime.

The flow resistance and the pressure distribution are then the same at every daughter vessel in the branching hierarchy. The injection of microparticles in such structure unbalances the channel which led to the liquid to flow preferentially in the branching with a lower resistivity. It results in that the plug is not uniformly perfused (see picture on the right).

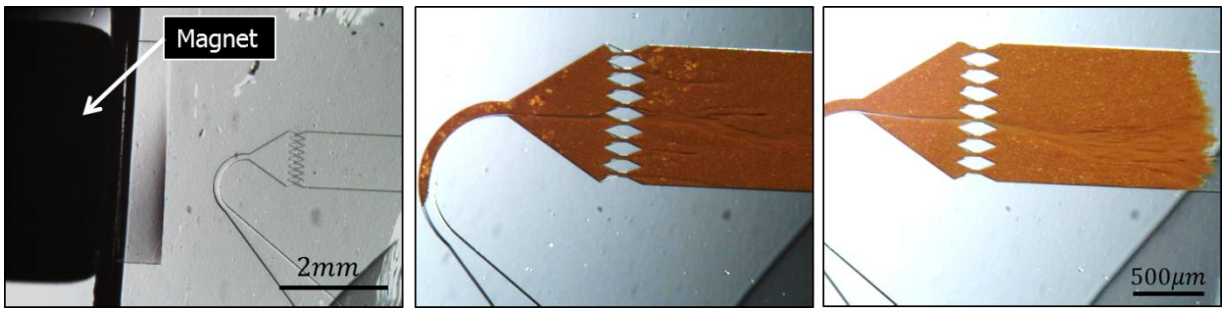

Figure II.25: Microchip made of strictures along the cross-section of the channel.

Unfortunately, none of these devices could provide a uniform distribution of the flow. Even if the hydrodynamic resistance in each injection channel is the same, the liquid flows preferentially in one of the injection channel due to the presence of the microparticles, thus creating a fracture in the bed.

We think that the cohesive forces in the bed induce a flow resistance which significantly higher than those of each injection channel. As a consequence once fluidisation occurs in one of the branches, the system tends to minimize its energy and the fluid follows the fracture that was created.

In conclusion, even if we succeeded to get a homogeneous magnetic field, the problem of the flow uniformity into the plug was still persistent. As we previously observed, the sudden changes of the channel width, give rise to a non-uniform distribution of the velocity flow profile and only a portion of the bedundergoes fluidisation (see Figure II.23).

In order to limit the influence of the cohesive forces in the bed and to benefit from the largest fluidisation area, we decided to design a wedge-shaped microchannel i.e. a channel exhibiting a gradual widening. We built the channel geometry on the base of the experimental results, we gathered with the former designs in particular the one presented in Figure II.22. The channel geometry was defined according to the dimension and shape of the observed fluidization region. We will further see that this approach enables to obtain a wider zone with flow velocities sufficient to lift particles i.e. larger than the minimum fluidization velocity.

The final microchip design is presented in Figure II.26. The core part of the device is a $21\,mm$ long and $50\,\mu m$ deep channel with lateral dimensions that linearly widen from $100\,\mu m$ up to $2\,mm$. Three inlets have been integrated in order to keep some flexibility for

different applications,I_1, I_2, I_3 are used as fluidic inlets and the O_1 as the outlet. To generate a magnetic trap, NdFeB[12] permanent magnet was placed close to the channel. This one creates high field strength parallel to main channel x-axis. As the magnetic field intensity decays along the channel, high magnetic field gradients are thus generated. These gradients are required to increase the magnetic force acting on the particles which induces their confinement. The distance between the chip and the magnet is 2 mm. The latter is magnetized in the longest dimension and exhibits a remanent magnetic field of 1.47 Tesla.

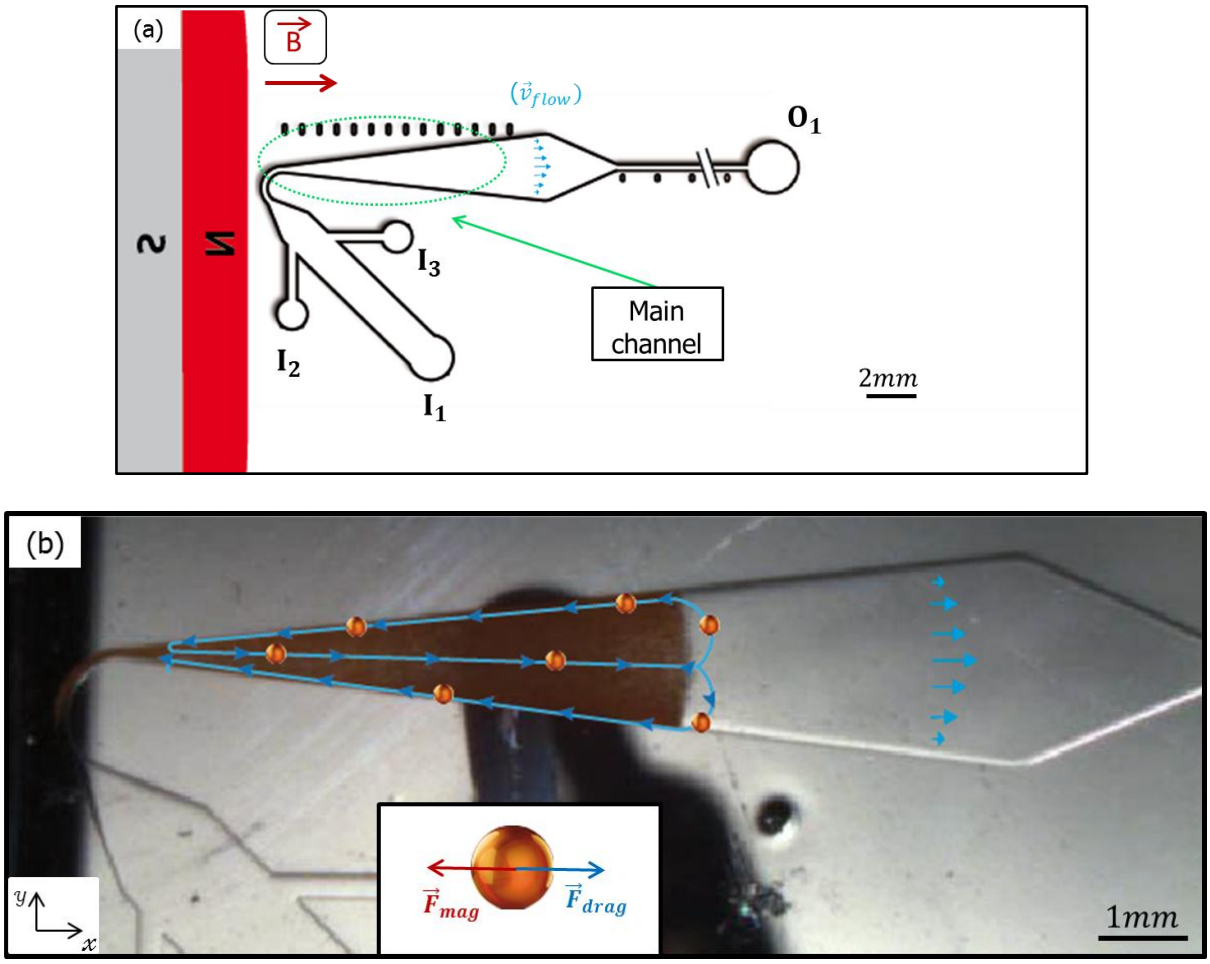

Figure II.26: (a) A permanent magnet is placed directly in front of the main channel (perpendicularly and closest to the channel at around 2 mm). (b)Recirculation paths of the magnetic particles within the plug during the fluidized bed regime.

The first preliminary tests with this geometry showed indeed a uniform fluidisation of the bed thus providing a confirmation of our hypothesis regarding the flow distribution. This device has been used to carry out all the further investigations dealing with the hydrodynamic aspect of the bed.

[12]Magnet dimensions: 30x20x20 mm, N50 (Chen yang Technologies).

6. Spatial magnetic field distribution

3D COMSOL simulations were performed to investigate the magnetic field intensity in the bed and the corresponding magnetic forces on the particles. The device geometry was defined according to the design shown in Figure II.26. The permanent magnetization of the magnet was set to $B_r = 1{,}47\ T (H \simeq 1170\ kA.m^{-1})$ according to manufacturer's datasheet.

Figure II.27shows several 3D and 2D images showing both the magnetic field intensity and orientation in the bed area. The maximum $|\vec{B}| \simeq 0{,}7\ T$ values are obtained close to the channel entrance.

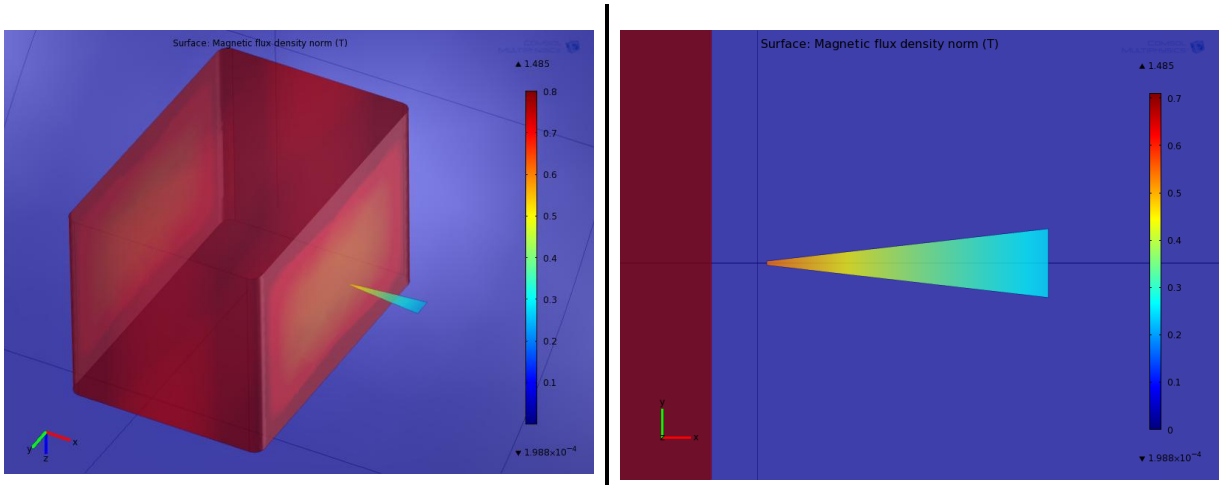

Figure II.27: Magnetic field intensity generated by a permanent magnet. 3D simulation (Left picture) and 2D simulation (right picture).

Along the x-axis, the magnetic field intensity decreases smoothly down to $|\vec{B}| \simeq 0{,}1\ T$ at $2\ mm$ from the bed entrance. In Figure II.28, simulations show a uniform magnetic field orientation along the x-axis only (magnetic field $\vec{B}$ is indicate by red arrows).

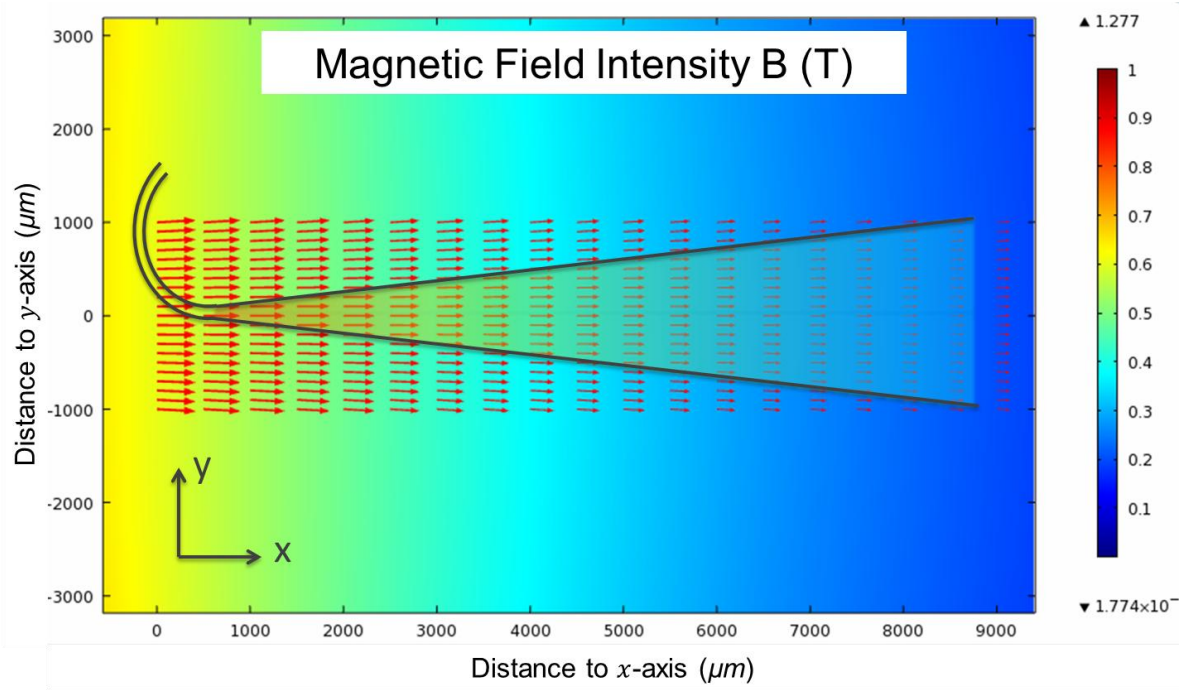

Figure II.28: Top views of the channel intensity and orientation.

We performed quantitative investigations of the magnetic field intensity $|\vec{B}|$ and its x and y components B_x and B_y in the main channel: along the x-axis (i.e. along the flow direction), the magnetic field component in the y-axis is almost null thus causing $\vec{B} \equiv \vec{B}_x$. (Figure II.29). The field intensity decreases almost linearly from $0.7\,T$ down to $0.36\,T$ from $x = 0$ up to $x = 1\,mm$.

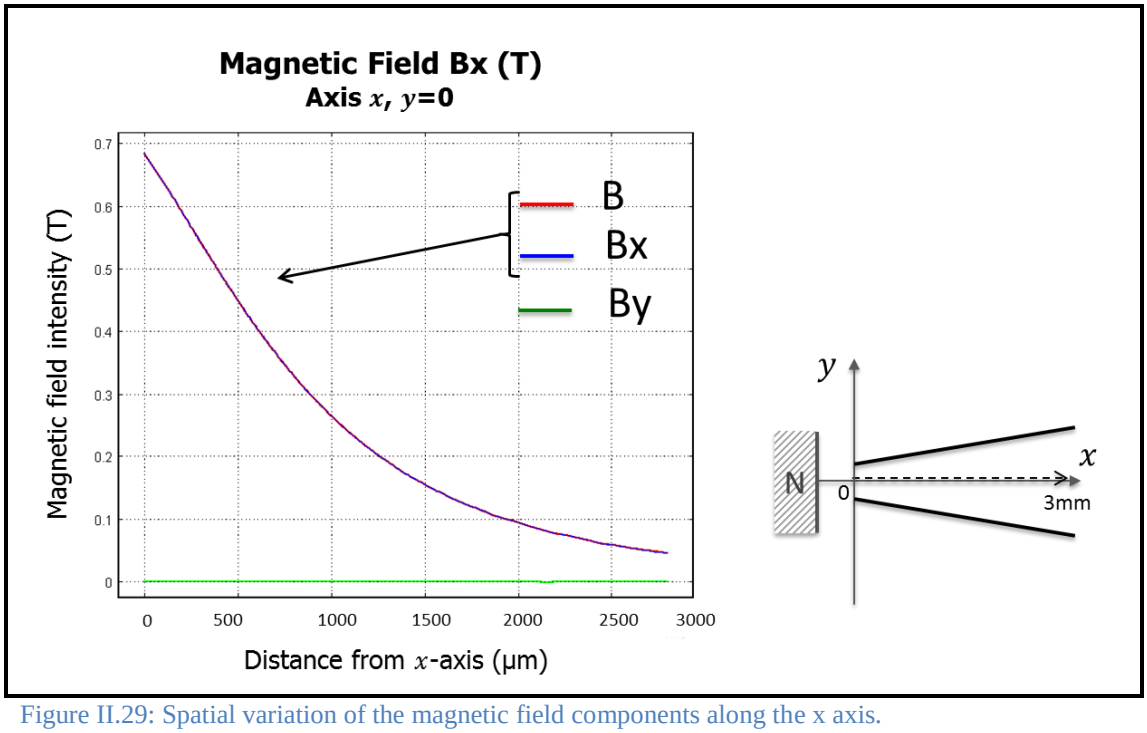

Figure II.29: Spatial variation of the magnetic field components along the x axis.

Figure II.30 shows the magnetic fields component along the y-axis (i.e. perpendicularly to the flow direction) at$x = 2.5\ mm$. As can be seen, even if a slight variation of $\vec{B}$ is observed in the transverse direction, $\vec{B}_y$remains negligible in all the bed area and the condition $\vec{B} \cong \vec{B}_x$ is still valid. These two observations are very important as they show i) that a magnetic field gradient (and thus a force) is generated in the device ii) that this gradient is mainly oriented in the same direction as the magnet field i.e. along the x-axis.

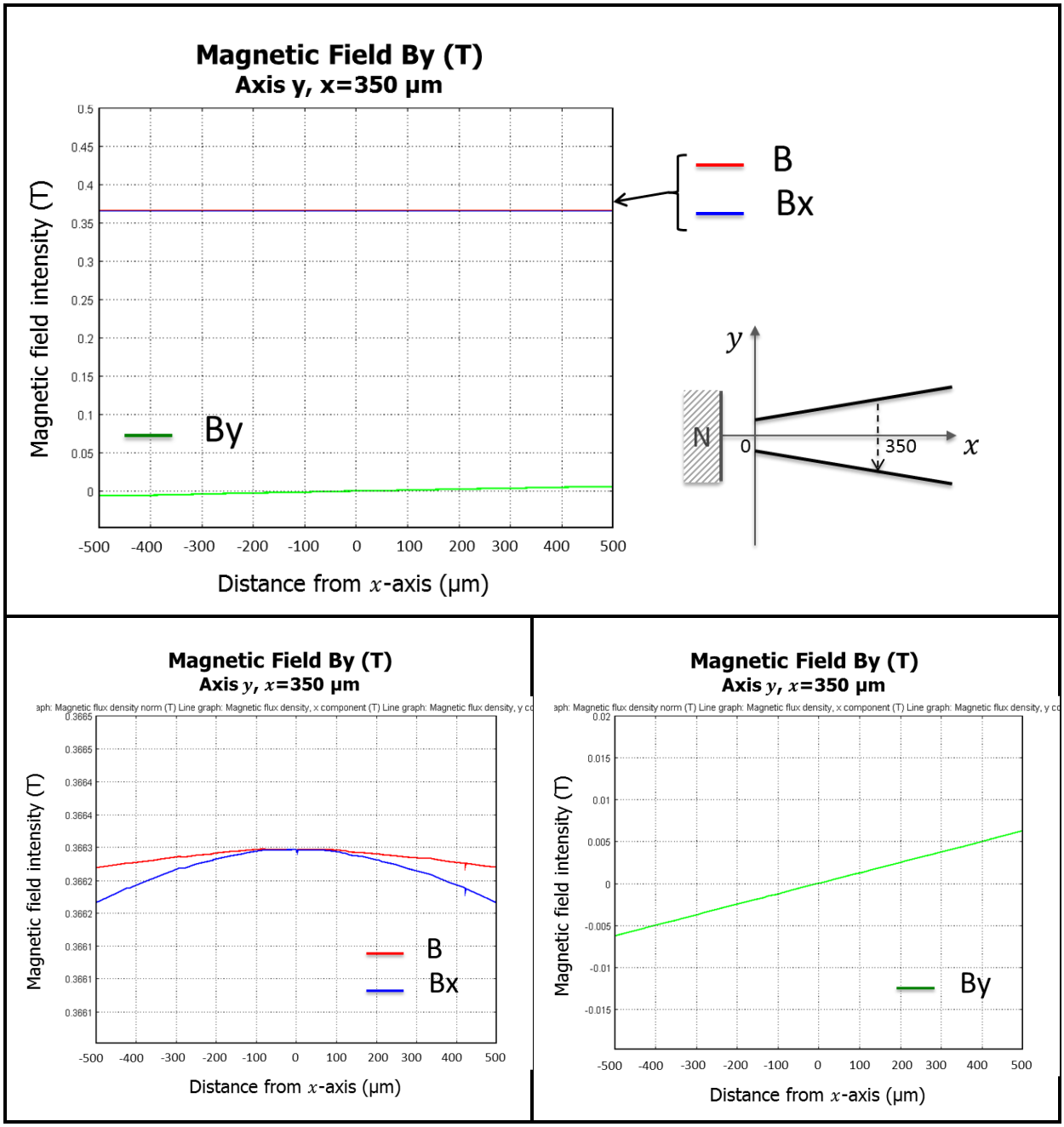

Figure II.30: Spatial variation of the magnetic field components along the y axis, at $x = 2.5\ mm$ (distance to the channel entrance). In the bottom images, the magnetic field intensity scale was modified to provide more details on (b) B,B_x and (c) B_y.

The question of the force intensity variation on a particle in the channel still needs to be addressed. For that purpose, the magnetic interaction energy of the particles was calculated from COMSOL simulations. We first search out an equation to fit with the magnetization curve($\vec{m} = \chi \vec{B}$) of Dynal $\emptyset$ 2.8 μm particles (Figure II.31)[145], [146].

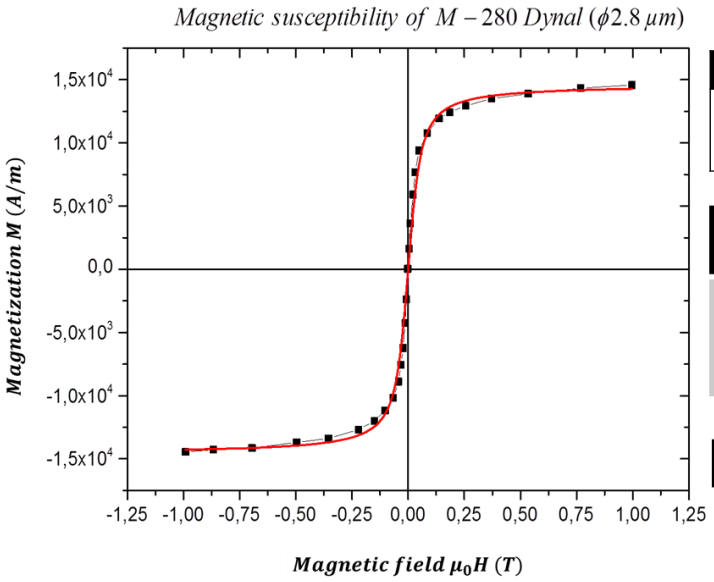

Fit Equation: Langevin formalism

$$y = C\ [\coth(x \cdot x_c) - \frac{1}{x \cdot x_c}]$$

	Value	Standard error
Magnetization	$x_c = \left\{\frac{\mu_0 \mathrm{mH}}{\mathrm{KT}}\right\}$	45
	$C\ (= \mathrm{M})$	$1.46 \cdot 10^4$
Adj. *R*-Square	0.994	

Figure II.31: Magnetisation curve of M-*280* Dynabeads and corresponding fitting parameters.

The magnetic energy distribution U_m was then obtained from the simulation dataset using the following equation $E_m = -(\vec{m}.\vec{B})$. The Figure II.32 shows a 2D plot of E_m. The main channel design was overlaid on the graph for a better understanding.

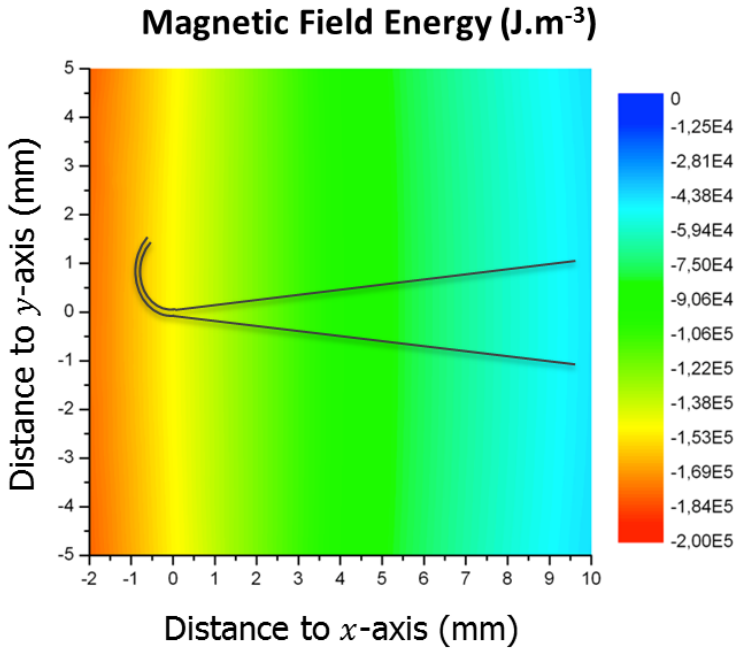

Figure II.32: 2D spatial distribution of the magnetic field energy in the main channel

As expected, the spatial variations of the energy in the y-axis is negligible and only a dependence of E_m as a function of the distance to the magnet is observed. Interestingly, the calculations show moderated variations of E_m in the main channel along the x-axis: E_m is

maximum at the channel entrance ($x = 0$, close to the magnet) and decreases only by a factor 2 at $x = 7\ mm$.

We finally investigated the magnetic forces acting on *M-280* Dynabeads. Results were obtained by extracting the magnetic field intensity $|\vec{B}|$variation along the x-axis (Figure II.33).

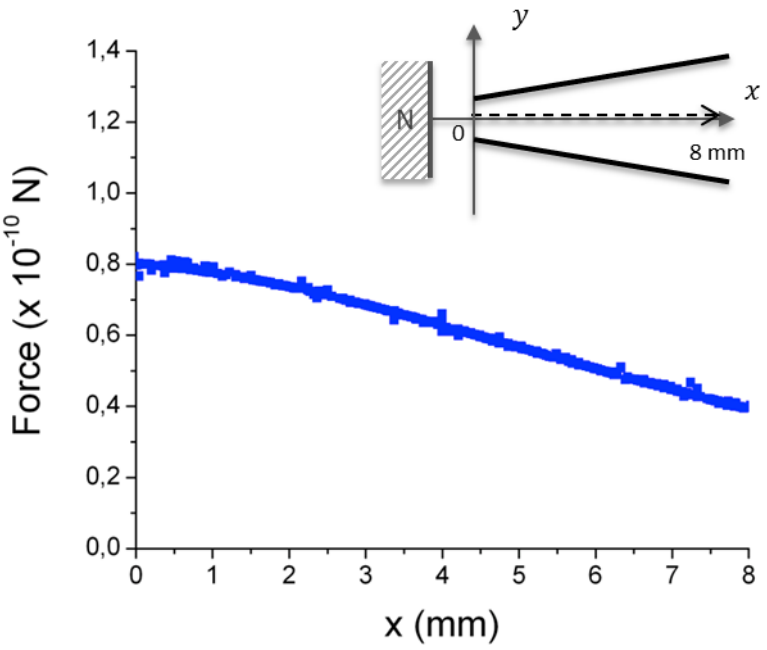

Figure II.33: Spatial variation of the magnetic force on *M-280* Dynabeads (superparamagnetic particles) along the x-axis.

The force acting on a single particle is almost constant from$x = 0$to $x = 1\ mm$, $F_{1-P} \sim F_0 = 80\ pN$. The force then decreases linearly from $x_0 = 1\ mm$ to $x = 8\ mm$ according to $F_{1-P} \sim \frac{F_0}{2} \frac{x - x_0}{\Delta l}$($\Delta l$, bed length). This result is important as it shows that, even if a constant magnetic force cannot be obtained in the microfluidic device, the use of a large permanent magnet provides high force intensity values with limited variation in space.

Of course, the force values have to be compared to the hydrodynamic drag forces exerted by the fluid and it will be addressed in the next paragraph.

Taking into account the wedge profile of the channel, we can write $A_{x=l} = H\ l\ \frac{W}{L}$ where W and L are the dimensions of the plug measured experimentally.

The equation 29.b can be written as:

$$\vec{F}_{mag} = \frac{(1-\varepsilon)}{V_P}\int_0^L F_{1-P}(x=l)\,A_{x=l}\,dl$$

Equation 31

Where $F_{1-P} = V_p \frac{\Delta\chi}{\mu_0}(\vec{B}.\nabla)\vec{B}$, the force acting on a single particlelocated at $x = l$

Then using the empirical form found for the magnetic force on a particle, we get:

$$\vec{F}_{mag} = \frac{(1-\varepsilon)}{V_P}\frac{H\,W}{L}\frac{F_0}{2}\int_0^{x_0} 2l\,dl \int_{x_0}^{L} l\,(2-\frac{l-x_0}{\Delta l})\,dl$$

Equation 32

$(x_0 = 1\,mm)$

Finally, we can extract ΔP from the latter equation

$$\Delta P_{mag} = \frac{(1-\varepsilon)}{V_P}\frac{F_0}{2L}\left\{L^2\left(1+\frac{x_0}{2\Delta l}\right)-\frac{L^3}{3\Delta L}-\frac{x_0^3}{6\Delta l}\right\}$$

Equation 33

which leads to pressure $\Delta P_{mag} = 21\,mbar$ when using the dimensions of the plug $W = 1.28\,mm$ and $L = 5.45\,mm$ at the threshold flow rate of initial bed fluidization $Q = 3\,\mu L/min$ (Table 2). This estimate correctly matches the gap pressure induced by the magnetic fluidized bed $\sim 20\,mbar$ as observed experimentally.

7. Fluid flow and particle distribution in magnetic fluidized beds

a. Microparticle capture

Figure II.34 depicts the microfluidic system used to investigate the hydrodynamic behaviour of the plug. A pressure-driven flow is established through the chip as explained for the first chip generation with the MAESFLO controller. The pressure is applied on the reservoir connected to I_1 and the flow rate is measured downstream in between $O_1$and the waste reservoir. Before starting an experiment, the whole system is filled by applying 1 bar pressure on the waste reservoir prefilled with buffer. Once the system is bubble-free,I_2andI_3 inletsare closed via electromagnetic valves. The system is then ready for the injection of the microparticles *(*Dynabeads*M-270, Ø* 2.8 *m).*

The injection step was improved throughout the experiments to control precisely microparticle amount. The details of the operating procedure will be discussed in chapter 3.

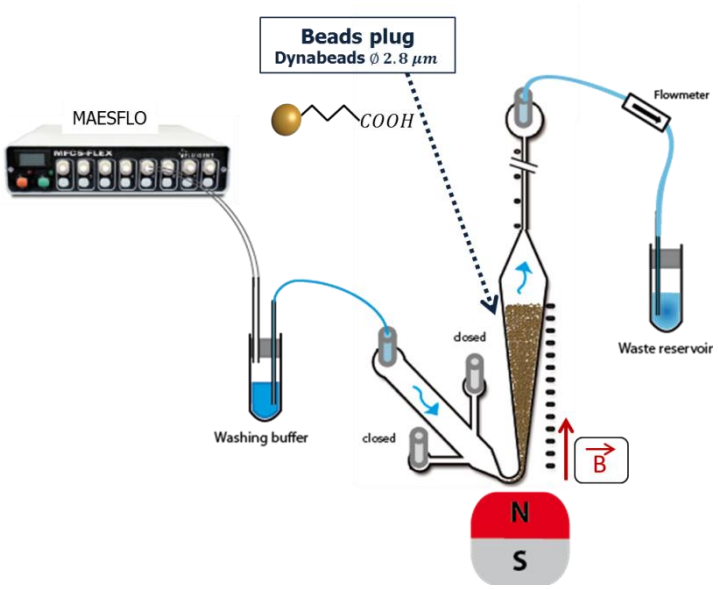

Figure II.34: Schematic representation of the magnetic microfluidic fluidized bed device

Figure II.35 shows a picture of the plug in its initial state right after particles injection.

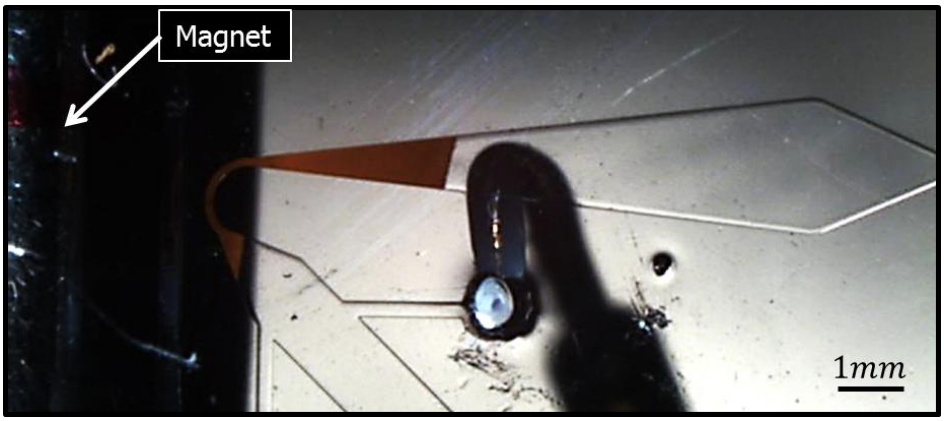

Figure II.35: plug picture after the microparticles injection. The plug is in packed bed regime.

Note: In order to perform a rigorous comparison between the results presented in this chapter and those of literature (referring to gravity driven fluidized beds), two comments have to be done regarding the operating conditions of our experiments:

i) In most experiments performed in this section, the bed was controlled through a pressure regulation mode using the MAESFLO system. Whereas most results reported in literature are done using flow regulators, the possibility to tune precisely the pressure appears as an advantage in microfluidic devices as they provide more accurate and reliable measurements as compared to conventional flow control systems (e.g. syringe pumps.). In most cases, the latter systems offer longer response time and, since often introduce hysteresis effects.

ii) The pressure drop reported in all the graphs is the difference of pressure between the inlet and outlet of the whole microfluidic setups including tubing and flow sensors. Whereas conventional curves reported in literature provide data about the bed only, we have to take into account the additional hydrodynamic resistances. A more detailed discussion of the influence of these additional resistances on the bed behaviour is proposed in the last paragraph of this chapter.

b. Pressure drop in the magnetic bed

Figure II.36 shows a typical pressure vs. flow curve obtained with the selected device design. The blue curve shows the evolution of the flow rate in an empty device i.e. where no particles were introduced. As expected, we observe a linear dependence of the flow with pressure thus showing that the device behaves as a simple fluidic resistance.

The black and red curves were obtained after introducing $50\ \mu g$ of *M-270 Dynabeads* in the system. The pressure vs. flow dependence of the corresponding bed was monitored in the $0 - 100\ mbar$ range. Starting from $0\ mbar$, the pressure was first increased at a constant rate of $1\ mbar/min$ (black curve). For pressure ranging from 0 up to $P = 90\ mbar$, the flow rate value remains below the sensitivity of the sensors meaning a very high hydrodynamic resistance of the plug. As confirmed by optical observations (Figure II.37), the bed is in the packed state: the pressure applied in the system is too low to compensate for magnetic forces and lift particles.

When reaching the pressure threshold$P_B = 90\ mbar$, the bed expands suddenly causing a significant increase of the flow rate up to $3\ \mu L/min$. This is the point of incipient fluidization. Above this threshold value the bed remains in the fluidized regime.

Note: For pressure higher than $110\ mbar$ *(results not shown) particles are dragged away from the channel and the fluidized bed progressively ceases to exist.*

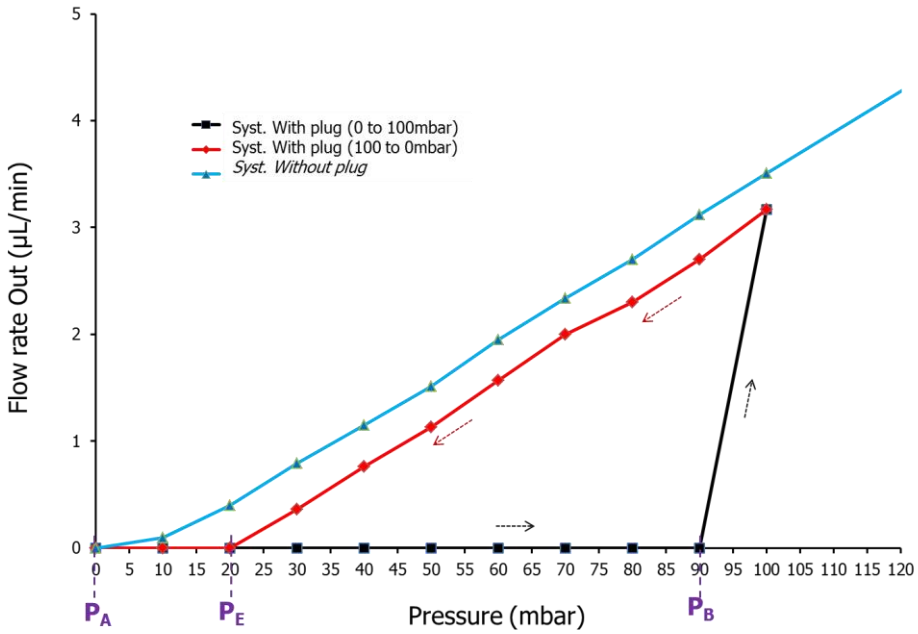

Figure II.36: Variation of the flow rate versus the pressure for a magnetic plug of 50 μg of *M-270.*

The pressure was then switched back from 100mbar down to zero at a constant rate of 1 $mbar/min$. During this process, the flow rate decreases linearly down to 0 at $P_E = 20\ mbar$. Optical observations revealed that the bed length was decreasing together with flow rate and switching back to the packed state when reaching P_E. It is very interesting to notice that all along this process, the slope of the red and blue curve are almost identical.

This behaviour can be explained according to the general description of fluidized bed that was done previously. Indeed, we mentioned that the pressure drop ΔP on a fluidized bed can be directly associated to the net force applied on the particles. In the case of gravity based beds, this force is constant, thus giving rise to a constant pressure drop across the bed.

In our case, taking into account the whole microfluidic system, the total pressure drop can be described as the sum of both the contributions of the bed itself and of the hydrodynamic resistance of the channels (given by the blue curve). This observation suggests that the pressure offset induced by the bed in the fluidized regime is almost constant. In other words, the net magnetic force induced on the particle is not significantly affected by the flow rate in the bed($\Delta p \simeq P_E$). This result is slightly in contradiction with the magnetic force calculations, which suggest that the net magnetic force on the bed should depend on the bed length. Unfortunately, a more quantitative analysis is difficult to establish.

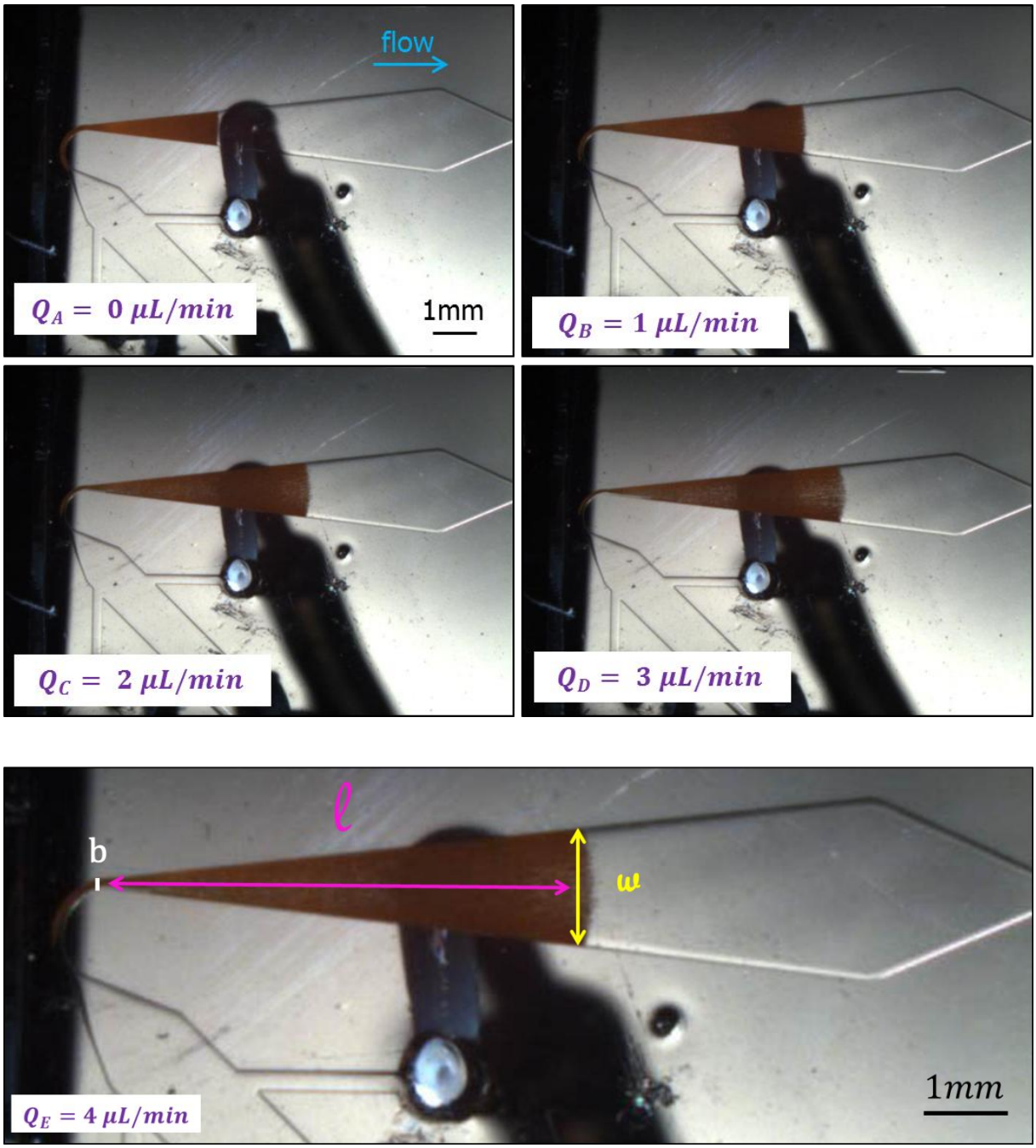

Figure II.37: Pictures of the hydrodynamic response of the plug at different flow rates. Parameters ℓ and w are the plug length and width, respectively. The constant parameter b is the curved channel width.

c. Pressure vs. flow rate hysteresis

The bed behaviour shows a clear hysteresis between increasing and decreasing pressure results. As mentioned above, the pressure drop induced by the fluidized bed can be related to the magnetic forces applied on the particles. However, the differences between the two thresholds pressures P_E and P_B is not obvious. We believe that this behaviour can be explained by the fact that when increasing pressure for the first time particles have to rearrange before fluidisation. In this process, the pressure applied in the system has to

overcome the cohesive forces between particles causing an additional pressure drop. Thus, a lower pressure drop is observed. The same behaviour can be found in gravity based fluidized bed as described in the book: Fundamentals of Particle Technology[149].

This hypothesis is strengthened by the results of Figure II.38 showing the pressure-flow curve obtained by repeating the measurement in the same bed by using a flow rate controller. Interestingly, we observed that the minimum pressure drop giving rise to fluidisation is found around $\Delta p \simeq P_E \simeq 20\, mbar$ and is thus significantly lower than the previous value. This result suggests that the minimum fluidisation pressure is affected by the bed history.

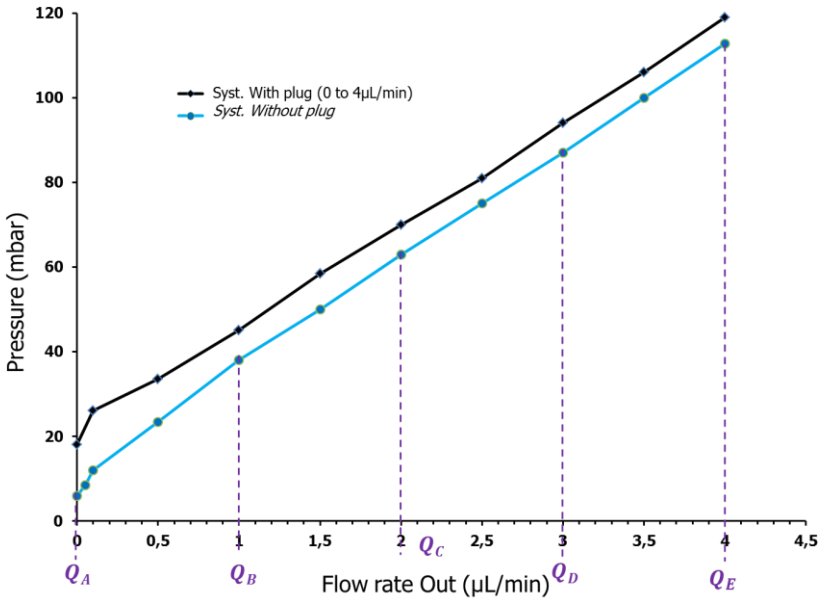

Figure II.38: Third activation of the fluidization process on the previous plug. The black curve shows its hydrodynamic response when a flow rate is set.

Conventional fluidized beds are driven by flow rate control, however, in our case, the system was controlled through pressure regulation for the hydrodynamic plug behaviour investigations and will be controlled through a flow rate regulation for the immunoextractions (chapter 3).

An analogy can be done between the minimum fluidisation velocity and we can define the minimum fluidisation pressure$\Delta p_{mf} \simeq P_E \simeq 20\, mbar$.

d. Flow distribution in the fluidized bed

We investigated the flow distribution and particle motion in the fluidized bed. As illustrated in Figure II.39, a flow of particles downwards is observed in the centre of the channel. In this region, the flow rate is sufficient to compensate magnetic forces and to drag particles together with the liquid flow. However, we clearly distinguish on the channel sides, recirculation flows that bring particles back to the channel entrance. This behaviour, called

spouting is also observed conventional fluidized bed and can be related to the channel geometry and to the flow field distribution that is induced in the bed. For that purpose, COMSOL simulations were performed to investigate the flow profile in a wedge shaped channel. The flow rate was set to 3 $\mu L/min$ according to the maximum flow rate measured in our experiments.

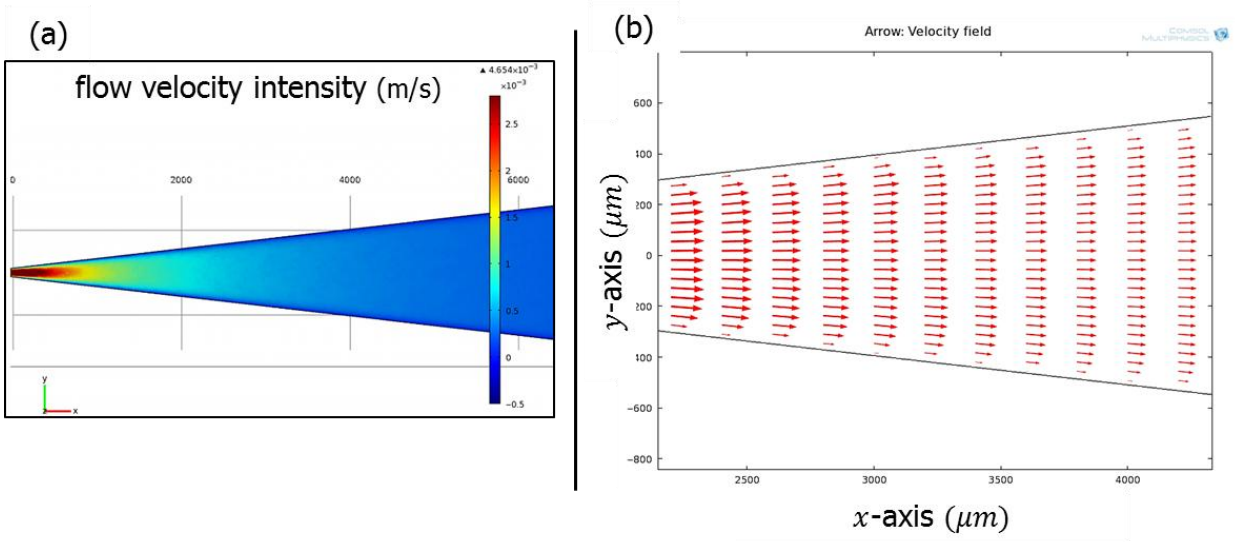

Figure II.39: 3D simulations of the flow distribution in a wedge shaped channel. The flow rate was set to 3 $\mu L/min$. (a) The images indicate the flow velocity intensity (m/s) and (b) spatial distribution. ($x$and$y$ scales in μm)

Quite obviously, as the channel enlarges, the flow velocity decreases along the x-axis (from 4.6 mm/s down to 0.5 mm/s at $x = 3\ mm$). It is interesting to notice that the flow velocity profile is almost flat across the channel i.e. in the y-direction. It decreases significantly only when getting close to the wall due to the no slip boundary condition. This observation is also confirmed by the optical observation that shows a flat shape of the particle bed extremity. (The drag force is uniform in along the y-axis).

Based on these observations, we can propose the following explanation: Whereas the flow velocity in the centre of the channel is sufficient to drag particles (i.e. $U > U_{mf}$), it decreases close to the channel's wall below the minimum flow velocity value. In the latter case, the magnetic force is thus sufficient to attract particles and to create an upwards recirculation flow towards the channel inlet. Two mechanisms are thus taking place simultaneously: i) the homogeneous flow velocity in the channel provides a homogeneous particle fluidisation; ii) an additional particle recirculation is induced from the rear edge of the bed backward to the channel entrance.

e. Bed expansion and porosity

As the liquid flows through the bed, the hydrodynamic drag force compensates the magnetic force and leads to bed expansion and fluidization

Under different magnetic plug regimes, we have estimated the volume occupied by a given amount of functionalized beads ($50\ \mu g$) as a function of the applied flow rate. Figure II.37 shows a picture of the plug of magnetic plug in the main channel at a flow rate of $4\ \mu L/min$, in this situation, the magnetic plug is in a fluidized regime. Parameters L and w are the plug length and width, respectively. These are measured at each flow rate and enable to estimate the apparent volume of the plug. The constant parameters b and h are respectively the curved channel width and the microchip height.

The apparent volume of the plug at different flow rates was measured using the Image J software. The plug porosity given by$\varepsilon = 1 - V_p/V_{plug}$ was then calculated with the volume of the whole particles $V_p = 0.037\ mm^3$.

Flow rate ($\mu L/min$)	Plug width $w(mm)$	Length of plug $\ell(mm)$	**Volume of the plug**V_{plug} (mm^3)	**Porosity**ε(%)
0	0,752	2,942	0,063	41
0,5	0,979	4,073	0,110	66
1	1,051	4,496	0,129	71
1,5	1,145	4,820	0,150	75
2	1,178	5,061	0,162	77
2,5	1,239	5,310	0,178	79
3	1,280	5,451	0,188	80
3,5	1,294	5,619	0,196	81
4	1,316	5,824	0,206	82

Table 2: Characteristic parameters of the plug at different set flow rates.

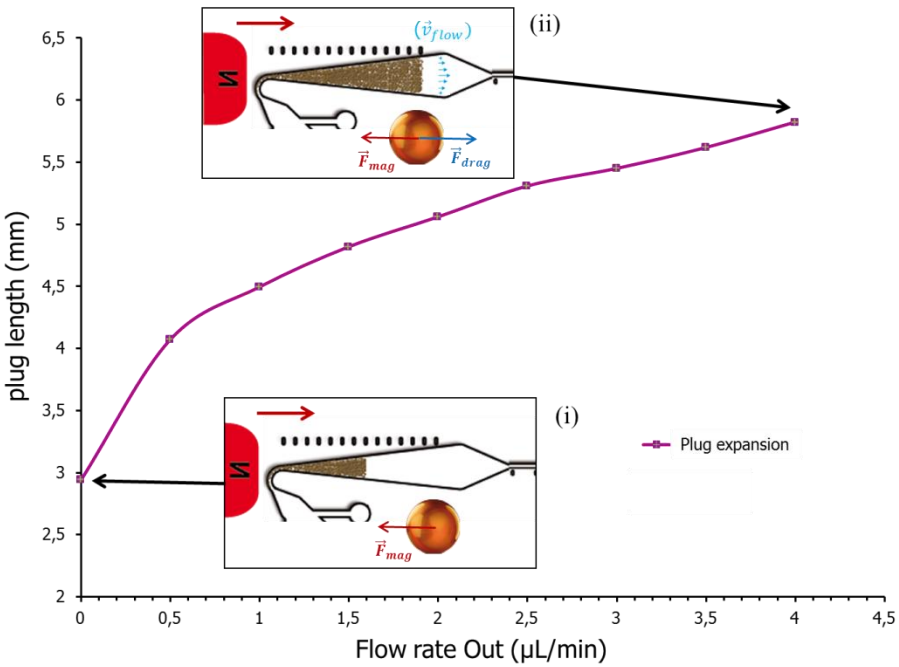

Figure II.40: Variation of the plug length versus the flow rate with a schematic view of a packed bead of *M-280* within PDMS chip in two different regimes (i) Below the minimum fluidisation pressure, the particles are compacted into a dense and static bed. (ii) Above this threshold, fluidisation takes place: the bed expands when increasing the flow rate.

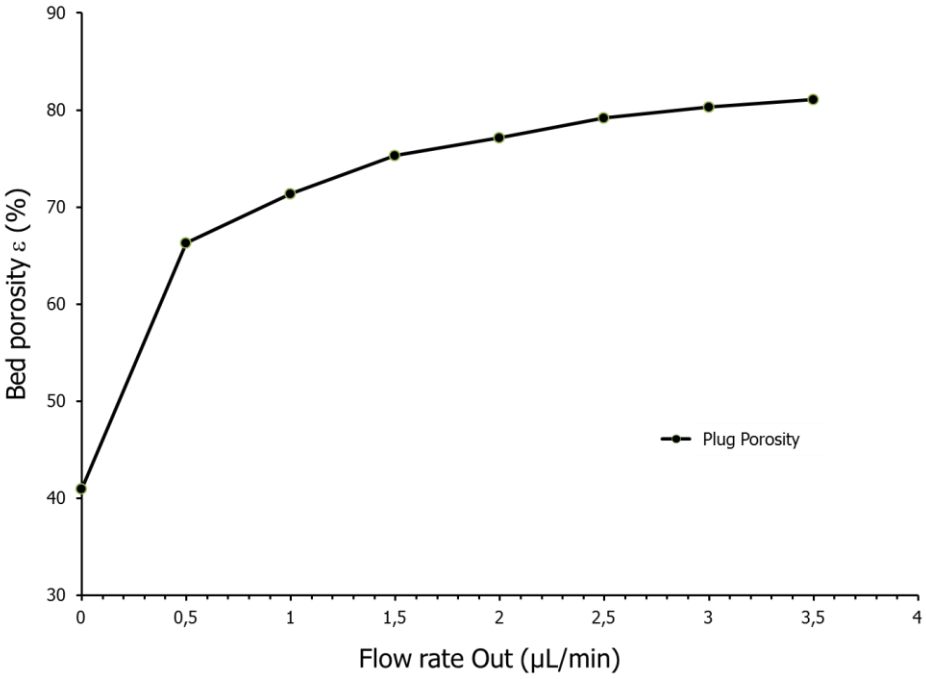

Figure II.41: Plug porosity versus the applied flow rate (see the corresponding values in Table 2).

We can notice that the plug porosity is twice time larger when the plug is in fluidized bed regime. Slightly above 4 $\mu L/min$, the microparticles can no longer be retained in the bed.

f. Fluidized bed activation: control of the fluid resistance

The fluidized bed activation is an important step that has to be carefully controlled to prevent any loss of microparticles during the process. While a minimum pressure has to be applied to initiate fluidisation, the fluid velocity in the bed must stay below the maximum fluidisation velocity. In this paragraph we propose practical and robust solutions to keep the bed in the appropriate operating conditions.

The fluidic resistance in microchannel is governed by a set of equations whose solutions are well known [12], [36]. In the pressure driven flow, the flow rate Q $(m^3.s^{-1})$within a microchannel is defined by

$$Q = \frac{\Delta P}{R}$$

Equation 34

where$\Delta P(Pa)$ is the pressure difference for driving the flow between an inlet and outlet, and R is the channel resistance$(Pa.s.m^{-3})$. For a circular geometry the resistance can be calculated by

$$R = \frac{128\,\eta\,L}{\pi\,{d_h}^4}$$

Equation 35

Where η is the fluidic viscosity, L is the channel length(m), and d_h is the channel diameter.We can note that high pressure drops are needed to drive flow in small microchannel $(R \infty \frac{1}{{d_h}^4})$. It is therefore important to prevent possible leakage in the microfluidic device by first sealing irreversibly the PDMS microchip and secondly by using suitable connectors that could withstand high pressures. The typical Upchurch©[13] connectors used in our microfluidic device could withstand pressure of 5 psi $(\sim 340\ bar)$ which well above our needs.

In our experiment, the pressure drop is created by applying a pressure at the inlet (I_1) using the MAESFLO controller and opening the outlet to atmospheric pressure (see Figure II.42). The controller regulates the pressure within the microfluidic device via a controlled leak. The connection between the buffer reservoir (pressurized) and the microchip inlet (I_1) is made by using a PEEK tubings with an inner diameter of $250\ \mu m$. The same tubes are used between the microchip outlet (O_1) via the sensor and the waste reservoir (P_{atm}). This PEEK tubes avoid the backpressure within the microfluidic system through their strong rigidity.

[13]Upchurch Scientific, IDEX Health & Science.

The strategy consistsininserting an additional fluidic resistance (R_2) in the microfluidic device outlet. This output resistance should be significantly higher than the plug resistance so that the flow rate within the device is mainly governed byR_2. At a pressure giving rise to fluidisation, R_2 must be high enough to keep the flow velocity belowU_{max} .

In order to estimate this resistance value, the maximum flow rate providing a stable fluidized bed was monitored experimentally. We found a flow rate slightly exceeding 4 $\mu L/min$. To ensure to keep in the microparticles confined, we calculated R_2 in order to get of 3.73 $\mu L/min$ flow rate when an applied pressure of 100 $mbar$ that we know is sufficient to initiate the fluidisation. To do so, a PEEK tube of 8 cm long and an inner diameter of 65 $\mu m$was used as resistanceR_2($1.61 \cdot 10^{+14} Pa.s.m^{-3}$).

In order to define precisely the plug resistance, one must first calculate the resistance of the entire tubing'sR_{peek} and sensorR_s. Subsequently, the resistance of the microfluidic system can be then deduced experimentally by measuring with $R_{0p}$and without the bed R_p(see Figure II.42). Once the plug is formed within the microchip, its resistance $R_p$is also deduced by difference with the system resistance.

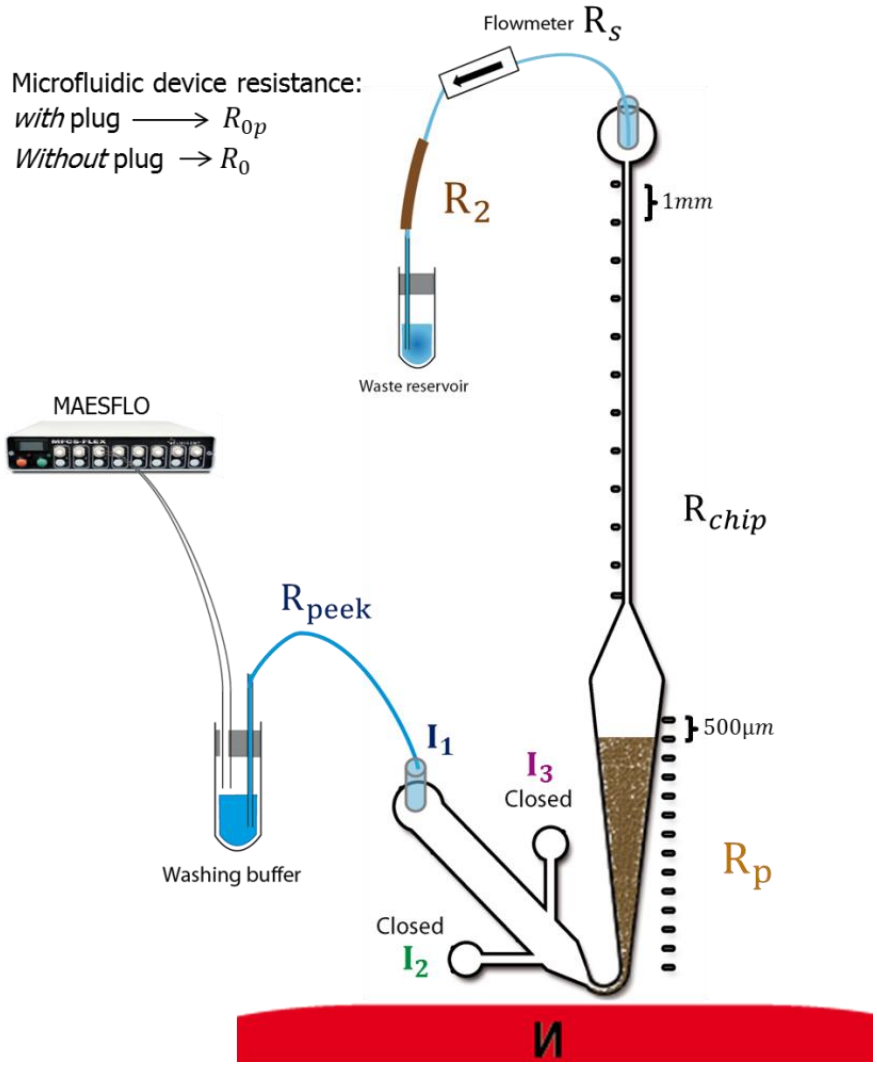

Figure II.42: Schematic summary of the different resistances constituting the microfluidic system.R_p, plug resistance;R_{peek}, tubes resistance; R_s, sensor resistance; R_{chip}, microchannel resistance and R_2, the output resistance.

The entire resistance of the microfluidic circuit is composed of resistance in series and can be given as

$$R_{0p} = R_0 + R_p$$

Equation 36

Where $R_0 = R_2 + R_s + R_{peek} + R_{chip}$ with R_{chip} is the microchannel resistance.

The Table 3 summarises the component resistances present in the microfluidic system. The whole resistances were calculated by taking the fluidic viscosity of the water ($\eta = 8.90 \cdot 10^{-4}\ Pa.s$).

components		Diameter $d_h(\mu m)$	Length $l(cm)$	**Resistance**$(Pa.s.m^{-3})$	Resistance (%)
Sensor	$\boldsymbol{R_s}$	150	3	$2.12 \cdot 10^{+12}$	1
PEEK Tubes (blue)	$\boldsymbol{R_{peek}}$	250	41	$3.76 \cdot 10^{+12}$	1.8
PEEK Tubes (beige)	$\boldsymbol{R_2}$	65	8	$1.61 \cdot 10^{+14}$	76
Microchip	$\boldsymbol{R_{chip}}$	/	/	$2.38 \cdot 10^{+13}$	11

Table 3: Resistance values and their proportions in the microfluidic system.

The resistance of the microfluidic system with or without plug is summed up in the Table 4, i.e.(R_0) or(R_{0p}), respectively. These resistances are given for different set flow rates. Then, the plug resistance can be defined for each case.

		Microchip *without plug*		Microchip *including plug*		Plug
Flow rate $(Q)(\mu L.min^{-1})$	$Q(m^3.s^{-1})(\text{x}10^{-11})$	Pressure $(\Delta P)(mbar)$	$\boldsymbol{R_0}(Pa.s.m^{-3})$	Pressure $(\Delta P)(mbar)$	$\boldsymbol{R_{0p}}(Pa.s.m^{-3})$	$\boldsymbol{R_p}$ $= R_{0p}$ $- R_0(Pa.s.m^{-3})$
1	1.67	38	$2.28 \cdot 10^{+14}$	45	$2.70 \cdot 10^{+14}$	$4.20 \cdot 10^{+13}$
3	5	87	$1.74 \cdot 10^{+14}$	94	$1.88 \cdot 10^{+14}$	$1 \cdot 14 \cdot 10^{+13}$
4	6.67	113	$1.69 \cdot 10^{+14}$	119	$1.74 \cdot 10^{+14}$	$9.45 \cdot 10^{+12}$

Table 4: Resistances of the whole system with or without plug (R_0 orR_{0p}) and the plug resistance at different applied flow rates.

We can note that the plug resistance is not constant and decreases when increasing the flow rate. This behaviour confirms the previous results obtained when we investigated the hydrodynamic response of the plug. The average resistance of each component is given in Table 5

Resistance	R $(Pa.s.m^{-3})$	Resistance (%)
R_0	$1.90 \cdot 10^{+14}$	90
R_{0p}	$2.12 \cdot 10^{+14}$	100
R_p	$2.18 \cdot 10^{+13}$	10

Table 5: Average resistances of entire system with or without plug (R_0 orR_{0p}) and of the plug R_p.

The plug resistance represents only 10% of the total resistance of the microfluidic system and is practically equal to the microchip resistance.

As an experimental validation, we tested several output resistances$R_i < R_2$ and monitored the plug behaviour. The Figure II.43 shows the hydrodynamic response of the system using one of them ($R = 5.74 \cdot 10^{10}\ Pa.s.m^{-3}$).

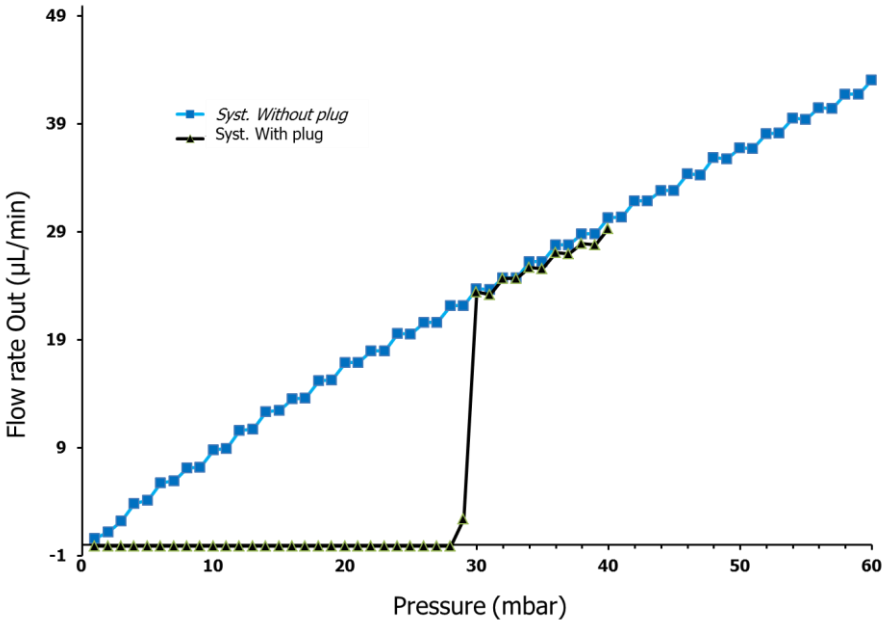

Figure II.43: Hydrodynamic response of a system with (black curve) and without plug (blue curve). A PEEK tube with a mean diameter of 500 μm and 10 cm length played the role of R_2.

We observed that the hydrodynamic response curve of the plug becomes similar to the one of the system without plug. However, the microscopic observations showed that the plug is entirely swept up when the flow rate jump occurs. This confirms that $R_2$is the minimal resistance that hasto be used in our microfluidic system to activate the fluidisation process while keeping the particles confined.

g. Balance between magnetic and drag forces

Based on the COMSOL simulations of the flow velocity distribution in the bed, we investigated the evolution of the drag force $\overrightarrow{F_d}$ in the bed and compared it with magnetic forces that we calculated previously. The calculation of $\overrightarrow{F_d}$ was done using the Stockes equation: $F_d = 6\pi\eta r_p v$.

Where is the viscosity of the liquid, r the particle radius and v is the flow velocity which was calculated taking into account a homogeneous porosity ε in the bed.

Two different flow rates were investigated: 3 $\mu L/min$ and 5 $\mu L/min$. Whereas the first value led to a stable regime for the fluidized bed, the latter caused particle loss in our experiments thus corresponding to a regime where the bed ceases to exist.

The magnetic force curve obtained previously war overlaid for comparison.

Note: In the case of a 3 $\mu L/min$ *flow rate, the velocities were corrected taking into account the porosity of the bed (around 80%).*

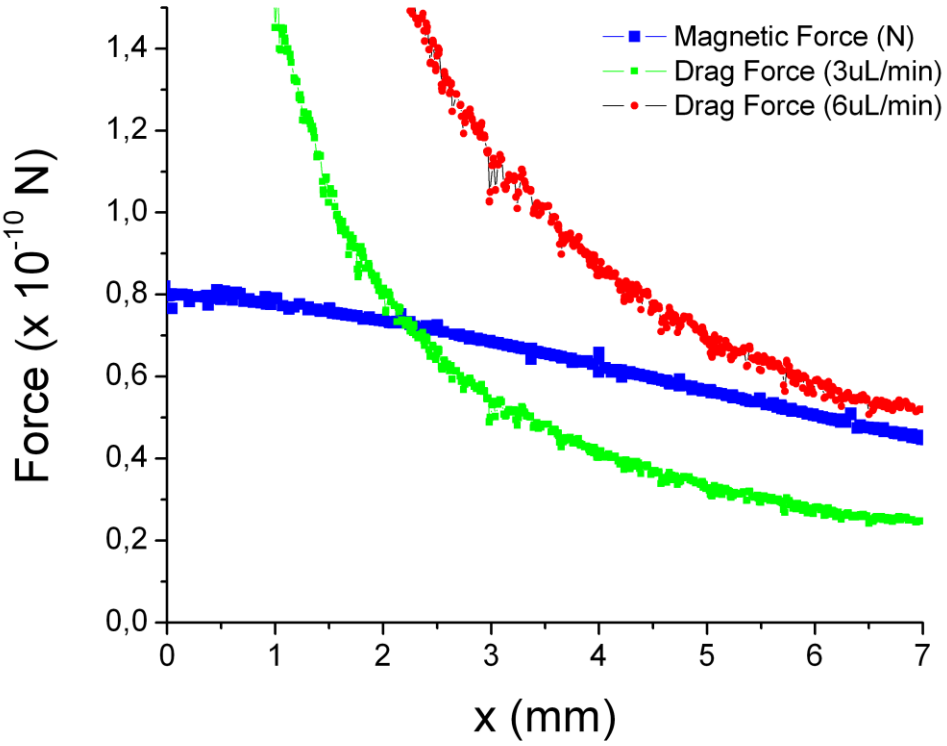

Figure II.44: Comparison of the magnetic (blue curve) and fluid drag forces for *M-280*. Two flow rates were investigated 3 $\mu L/min$ (green) and 5 $\mu L/min$ (red).

Both simulations seem to be in good agreement as the calculated forces are in the same range of values, typically comprised between $10^{-10} \sim 10^{-11}\ N$.

For a 3 $\mu L/min$ flow rate, the two curves crosses at $x = 2\ mm$:
this means that for $x < 2\ mm$, the particles are dragged by the fluid thus inducing fluidization. For $x > 2\ mm$, magnetic forces become preponderant. They attract the particles that were dragged beyond this distance and thus maintain the stability of the fluidized bed. According to this description, it thus tempting to assimilate the coordinate where $F_{drag} = F_{mag}$ to the position of the rear edge of the bed i.e. to the L value. This hypothesis is currently under investigation.

However when increasing the flow rate up to 5 $\mu L/min$, we observe that the hydrodynamic drag forces remain higher than the magnetic force, independently from the distance to the magnet. This result is in good agreement with experimental observations that show bed dismantlement. This is an additional validation of the model.

8. Conclusion

We have designed and fabricated an integrated system for the confinement and handling of superparamagnetic beads in a microfluidic device. This innovative system uses magnetic forces instead of gravity to activate the fluidization process. To our knowledge, this approach has never been reported yet in microfluidics.

The integration and operating conditions of the system have been optimized to provide a reliable and robust microfluidic platform. We also proposed numerical simulations to describe the different bed regimes and anticipate the influence of the magnetic field distribution on the particle behaviour and bed parameters (porosity, length).

Experimental observations of the fluidized bed show a homogeneous and stable distribution of the particles in the magnetic trap. These results suggest potential improvements of the efficiency of the analyte capture and release in a plug with well controlled porosity. The next chapter will emphasize this point through the investigation of on-chip immunoextraction.

Chapter III. On-chip immunoextraction

1. Introduction

Several attempts to increase the efficiency of the target capture byimproving "interactions" between the sample and the magnetic beads have shown the advantages of using permanent magnets to formdense and static magnetic plug[122], [123], [155], [156]. In particular, it was demonstrated that, in the absence of diffusion limitation, an increase of the surface to volume ratio enabled a significant improvement in the capture kinetics. In this context, the fluidized magnetic bed that we developed appears as a valuable candidate for its integration as a dynamic immunosupport in a microdevice. The use of such dynamic bed offers clear improvement in particle mixing and makes the whole bead surface available for target immunocapture.

The integration of different types of bioassay, such as enzymatic digestion or sandwich immunoassay, based on this dynamic magnetic plug could be considered. As a first proof of concept we have been interested in the development of an immunoextraction support for Alzheimer biomarkers. Alzheimer disease (AD) is one of the most common age related neurodegenerative disorders. It has a slow evolution, without clinically clear symptoms for often more than 10 years. No cure for the disease's damage exists, but intense research on the development of neuroprotective drugs should provide efficient treatments in the near future. It is thus critical to diagnose Alzheimer disease at very early stages. For such predictive diagnosis, the current approach relying on the analysis of a lumbar puncture of cerebrospinal fluid (CSF) is not possible, since this is a highly technical, relatively expensive act, not fully exempt of risk. In the frame of a European Project (NADINE Project – FP7), we have been interested in performing AD early diagnosis directly on blood. However the concentration of the relevant AD biomarkers in blood is ultralow and it is challenging to detect such biomarkers while avoiding any invasive tests[157]. It is thus essential to be able to extract and concentrate these biomarkers prior to their analysis.

After the first step of dynamic plug development and physical characterization, described in the previous chapter, the second aim of our work was to evaluate the possibility to perform an efficient immunoextraction using such dynamic magnetic plug. The potential of microfluidic fluidized-bed system forsolid phase immunoextraction was first investigated using model compounds (Fluorescently-labeled IgG), the extraction being based on the interaction between antibody-coated beads and target antigens.

In particular, the objective was to provide an easy-to-handle device dedicated to biomarkers immunoextraction combined with a precise control of the injected volumes. We first present off-chip investigations to evaluate and improve the protocol of target capture and elution. Thereafter, the microfluidic platform used to perform the control and the manipulation of the different and its integration into the microfluidic device will be presented. Thirdly, the studies carried out on the microfluidic elution process itself will be discussed in

order to evaluate the influence of the hydrodynamic behaviour of the plug on the detection sensitivity. Finally, preliminary results of microfluidic immunoextraction obtained with such fluidized bed-based device will be presented and discussed.

2. Model compounds Ab/Ag

We started working with a model Antibody/Antigen (Ab/Ag)capture as an early proof of concept. The fluidized bed-based immunoextraction was performed using Dynabeads® as immunosupport for the capture of labelled IgG.Unlike the particles used in chapter 2, these superparamagnetic microparticles are coated with antibodies (Ab) covalently immobilized onto their surface. Even if the final aim of this work is to deal with biomarkers, we have first evaluated the potential of this immunosupport using a fluorescent anti-IgG / IgG system. As large choice of functionalized microparticles is available on the market andthis strategy avoids i) the initial step of beads functionalizationii) the biomarkers fluorescent labelling step that is usually quite complex. The Dynabeads are "ready-to-use", exhibit a defined surface chemistry tuned to limit beadsaggregation and non-specific binding. On the other hand, the microparticles have uniform size and properties (density, diameter and iron content, surface chemistry) thus improving the homogeneity and stability of the bed.

3. Off-chip Ag capture and elution

a. Off-chip characterisation and optimisation of the protocol

The immunoextraction principle can be briefly described as follows. First the sample of interest mixed with the affinity support under conditions in which the analyte will bind strongly to the immobilized antibody. This is usually performed at pH and ionic strength that mimic physiological conditions. Because of the specificity of the Ag/Ab interaction, other compounds in the sample should have weak or no binding to the immunosupport and most of them should be washed off from the immunosupport in one (or multiple) subsequent washing steps. Then, an elution buffer is applied to dissociate Ag/Ab complex. This elution step commonly involves either changing the pH and/or buffer composition of the mobile phase. The eluted analytes can thus be detected or collected for further use.

Besidesthe immunoextraction protocol employing magnetic microparticles (considered here as immunosupport) consists in a series of the microparticles handling steps, as shown in Figure III.1.

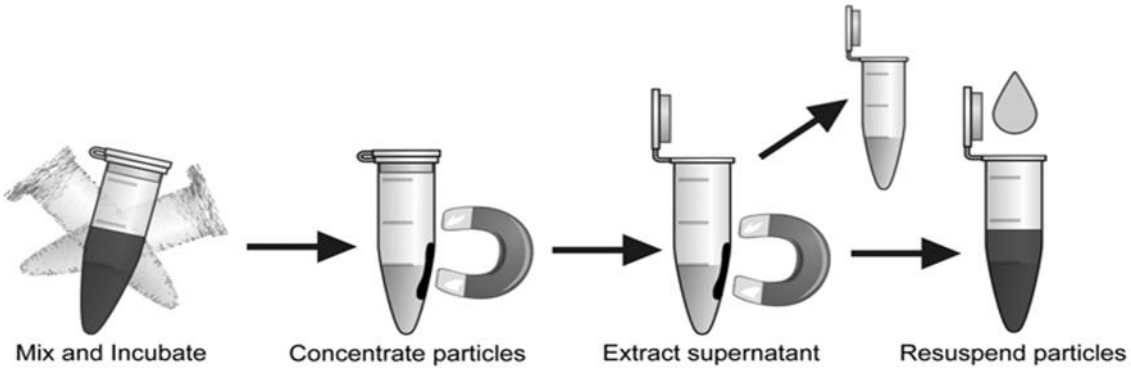

Figure III.1 : Procedural sequence for magnetic microparticle-based bioanalysis. After the extraction of the supernatant the process is repeated to wash the target-microparticle complexes.

First, microparticles are mixed with the sample and the mixture is incubated. The microparticles-target complexes are then concentrated with an external permanent magnet attracting them onto the tube walls. Once the magnetic separation is achieved, the supernatant is sucked up using a pipette and the target-microparticle complexes are resuspended in the medium in a subsequent step for washing. This washing step was repeated to recover the unbound Ag molecules, and other unwanted molecules eventually contained in the initial sample. Finally, an elution buffer is added to release the bound targets, which are now contained in the supernatant. Fluorescence measurements were performed on the supernatant.

As previously mentioned, the model Ab/Ag immunoextraction was first tested off-chip in order to optimize the whole immunoextraction process before its integration on-chip. A short description of the immunoextraction conditions is given below; further details are reported in the specific material and methods section. In our experiments, the immunoextraction was performed using $2.8\,\mu m$Dynabeads grafted with sheep IgG targeting rabbit IgG[2]. These experiments were carried out in PBS containing 0.1% BSA to limit non-specific adsorption. Two types of fluorescently labelled IgG were used to evaluate the assay specificity: Alexa Fluor® 488 Rabbit Anti-Mouse IgG antibodies (specific target)[14]and mouse monoclonal IgG1 antibodies anti human CD1a (non-specific target). As it will be discussed below, different eluting buffers were investigated:Citrate buffer (0.1M, pH 2-3), Ammonia buffer (0.16% ammonia) at pH 9 and a sodium dodecyl sulphate (SDS)solution($100\,mM$).

To optimize off-chip immunoextraction, the Alexa-IgG detection was achieved on a microtiter plate reader (VICTOR X Multilabel Plate Readers).

[14]14http://products.invitrogen.com/ivgn/product/A11059?ICID==%3Dsearch-product

i. Materials and methods

Dynabeads M-280 sheep anti-rabbit IgG[15] *with a mean diameter of 2.8 µm were purchased from Invitrogen as an aqueous suspension. A volume of 16 µLof this suspension (i.e. 160 µg of microparticles) was pipetted into an Eppendorf tube (Lobind). 25 µL phosphate buffered saline (PBS) (1x) at pH 7.4 containing 0.1% bovine serum albumin (BSA) was added, and the suspension was vortexed for a few seconds. The microparticles were washed by collecting them onto one side of the tube via an external permanent magnet, then the supernatant was removed, and a fresh PBS/BSA buffer was added. This process was repeated twice to ensure that the microparticles were thoroughly washed. Finally, they were resuspended in 16 µL of PBS/BSA i.e. a concentration of 10 mg/mL (≈* $7 \cdot 10^8$ *particles per mL) and stored at 4°C until ready to use.*

Carboxylic acids Dynabeads M-270(Ø 2.8µm) were purchased from Invitrogen as an aqueous suspension (5.3 µL, 160 µg) of this suspension was transferred to an Eppendorf tube (Lobind) and washed with 25 µL of PBS/BSA as described above. Finally, the microparticles were resuspended in 16 µL PBS/BSA i.e. a concentration of 10mg/mL (≈ $7 \cdot 10^8$ *particles per mL) and stored at 4°C.*

Alexa Fluor® 488 Rabbit Anti-Mouse IgG antibodies[16] *(2 mg/mL) and mouse monoclonal antibodies to the human CD1a antigen (IgG1)*[17] *(0.2 mg/mL) are both labelled IgG obtained from Invitrogen. The manufacturer's specification for the working concentration is 1-10 µg of labelled antigen per mL.*

Phosphate buffered saline (PBS) (1x) (pH 7.4) containing 0.1% bovine serum albumin (BSA) was prepared by diluting by ten times a PBS solution and then adding 0.1% of BSA in PBS (W/V). This buffer is freshly prepared for each set of experiments and mainly used to stabilize the microparticles suspension.

Citrate eluent (0.1M) was prepared by dissolving citric acid monohydrate (10.5 g) in 450 mL of purified water; the pH was then adjusted to 2 or 3 with NaOH solution (5M).

---

[15] http://products.invitrogen.com/ivgn/product/11203D?ICID==%3Dsearch-product

[16] http://products.invitrogen.com/ivgn/product/A11059?ICID==%3Dsearch-product

[17] https://products.invitrogen.com/ivgn/product/CD1A20?ICID==%3Dsearch-cd1a20

Ammonia buffer (0.16% ammonia) was prepared and adjusted to pH 9 with hydrochloric acid and a SDS buffer (sodium dodecyl sulphate).

For the microchannel coating step, dimethylacrylamide-allylglycidyl ether (PDMA-AGE) copolymer was used. This copolymer solution was prepared by dissolving 0.5 wt % PDMA-AGE in water.

The detection of the labelled IgG was carried out using VICTOR X Multilabel Plate Readers. This fluorometre is compatible with all types of microtitration plates and enables to compare a series of experiments at the same time. The measurement time is 1 second and the approximate absorbance and fluorescence emission maxima are 495 and 519, respectively.

ii. Off-chip experiments

A first, a set of experiments was performed to investigate the compatibility of IgG particles in the fluidized bed. As the Dynabeads *M-280* sheep anti-rabbit IgG are susceptible to aggregate once the capture is ended, we have investigated the effect of the presence of carboxylic acid beads on the immunocapture. These beads, because of their electrostatic repulsive ability at neutral pH are very stable and thus, have already been used as a model for characterizing the magnetic fluidized bed. As we intended to favour the particle mobility in the bed, we used a 50/50 mixture of anti-IgG dynabeads and COOH-Dynabeads to limit the potential effect of the anti-IgG particle aggregation. For this purpose, a mixture of $50\ \mu g$ of each type of beads was prepared, and resuspended in a solution of Alexa IgG while gently vortixing to avoid settling of the microparticles in the tube. After two washing steps, the microparticles were resuspended in an elution buffer ($25\ \mu L$) and vortexed to allow an efficient elution. Afterwards, the supernatant containing the purified labelled target was pipetted off and transferred to a microtiter plate for detection. These first experiments showed that immunoextraction performed in these conditions was poorly efficient. To evaluate the influence of each type of bead on non-specific binding similar experiments were performed for each type of beads separately. Our findings showed a significant non-specific capture onto the carboxylic –beads acid of the order of 20 to 30%, whereas the anti-IgG beads leads to a non-specific binding of 8%.

In the light of these results, we concluded that the benefit brought along by the use of the Dynabeads *M-270* is not worth the risk, considering their high tendency to bind targets and non-target molecules non-specifically. In other words, we privileged specificity, and used pure Dynabeads *M-280* sheep anti-rabbit IgGaccepting some bead-bead aggregation.

We characterized the performance that could be achieved using such a commercial immunosupport. According to the manufacturer's specification, the working range is

approximately ranging from 0.1 to 1 μg of IgG per 10^7 beads (160 μg of microparticles) to get an efficient immunocapture. Thus, we evaluated the immunosupport capture efficiency in this range. For this purpose, Dynabeads suspension (16 µL) was incubated with two different amounts of specific target (0.3 and 0.8 μg).

The capture efficiency (CE) was estimated as:

$$CE = \frac{\boldsymbol{c}(injected\ IgG) - \boldsymbol{c}(unbound\ IgG)}{\boldsymbol{c}(injected\ IgG)}$$

Equation 37

Where $\boldsymbol{c}(injected\ IgG)$is the initial IgG concentration in the sample and$\boldsymbol{c}(unbound\ IgG)$ the IgG concentration of the supernatant after incubation of the sample with the magnetic immunosupport.

These values were obtained by measuring the initial sample and the supernatant fluorescence signal, using a microtiter plate reader (Table 1). Besides, to evaluate the immunosupport specificity, a non-specific target has been tested (*CD1a antigen (IgG1)).*

	0.3 μgspecific IgG	**0.8 μg**specific IgG	0.8 μg***non-specific IgG1***
Capture efficiency (%)	61 ± 2	50 ± 2	8 ± 1

Table 1: Capture efficiency for samples containing 0.3 μg and 0.8 μg of specific Ag and 0.8 μg of non-specific Ag, respectively.

According to these results, we observed that in this concentration range of target, a capture efficiency of the same order of magnitude is obtained for both amount of IgG, ranging from 50 to 60%. These experiments confirmed the immunosupport specificity as very low capture efficiency was found when incubating the immunosupport with a non-specific target.

Similar experiments were performed to select the most efficient eluting buffer. To this end, different elution buffers, a surfactant solution (SDS100 mM), an acidic solution (citrate buffer pH 2 to 3), and an alkaline solution (ammonia pH 10) were investigated. The citrate buffer leads to the highest elution efficiency probably due to its chaotropic property that allows disrupting the hydrogen bonding network between water molecules and reducing the stability of the native state of proteins by weakening the hydrophobic effect. The citrate buffer (pH 2) was used to elute the captured labelled IgG throughout the experiments.

4. On-Chip Immunoextraction

a. Description of the experimental set-up

The immunoextraction process requires the sequential injection of different solutions in the microfluidic system with a precise control of the injected volume while avoiding the reagents mixing. Moreover, the layout of the different components needs to be finely adapted to allow for safe and reproducible experiments. The following equipment was used for that purpose:

- MAESFLO system :
  - MFCS pressure regulator and its software
  - Flow sensors (feedback loop)
- Direct-acting solenoid valves
- PEEK tubes

As illustrated in Figure III.2, the core part of the experimental set-up is an integrated device comprising a permanent magnet and a PDMS microfluidic chip. Three inlets have been incorporated in the microchip in order to make possible the injection of several solutions I_1, I_2 and I_3 with minimal dead volume. The chip has a single outlet O_1. The permanent magnet is positioned parallel to the midline of the main channel and its distance from the channel wall and from the channel outlet is $2\,mm$ and 2.1cm respectively. Each inlet of the chip is connected to a reservoir via a valve; PEEK tubes are used to connect the reservoir to the device.

Note: During preliminary experiments, different injection systems have been investigated; syringe pump and pressure driver flow controller. We opted for the latter for its ability to fully control the pressure as well as the flow rate (syringe pumps may induce hysteresis effects that would be detrimental for the fluidized bed). As seen in chapter 2, the dependence of the plug permeation coefficient upon flow rate may yield strongly nonlinear hydrodynamic behaviours of the device in the presence of the magnetic particles. A better control is possible when both flow and pressure are controlled with this device, sub-microliter sample can be injected reproducibly.

The solutions were injected by applying a pressure $(45\,mbar)$into the correspondent reservoir through the pressure-driven flow controllers, MAESFLO. The flow velocity could be monitored inside the microfluidic system via the flow sensor integrated at the device outlet.

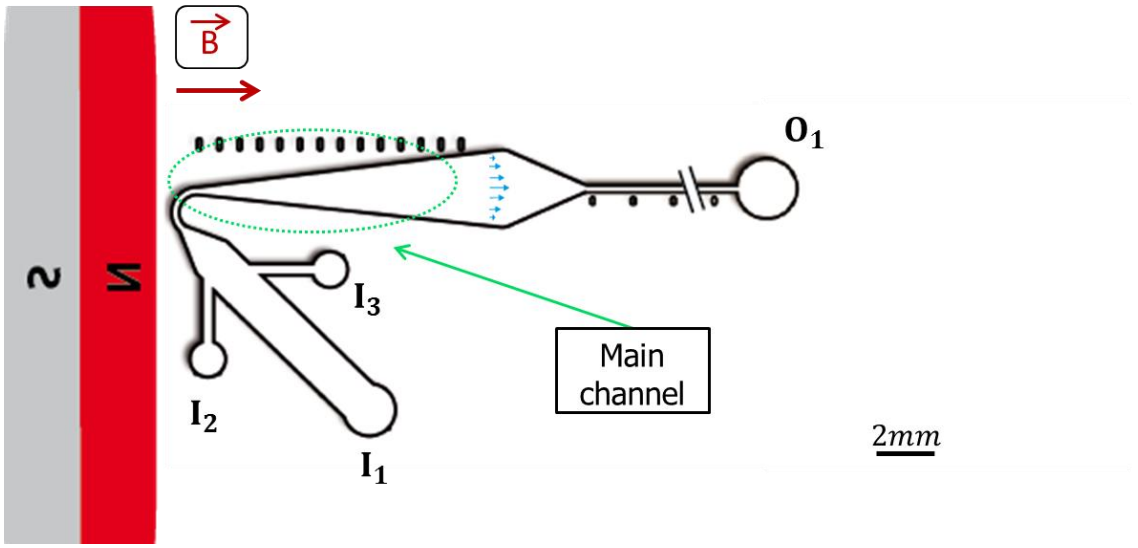

Figure III.2 : Schematic representation of the microfluidic fluidized-bed system using a permanent magnet. The permanent magnet generates a strong magnetic field roughly parallel to the main channel axis, with a gradient opposing the main flow direction.

As compared to chapter 2, the microchip design has been slightly modified in order to integrate a detection zone. A narrower channel downwards the active area of the channelwas used for the fluorescence detection. The detection channel width was designed according the detection window to facilitate measurements. In addition, this geometry allows to perform the measurement far from the bed area thus limiting potential interferences of the particles in the bed with the detection area.

Setting up of the magnetic fluidized bed has required a rigorous control of the resistance of the microchannels thereby leading to calculate the volume of liquid held in each PEEK connections, in the microchip, in the flow sensor (flowmeter) and finally in each valves (see Figure III.3) (cf. chapter 2).

To apprehend the operating conditions of the immunoextraction, Figure I.4 presents the schematic illustration of the microfluidic device. The different steps and solutions required to perform a complete immunoextraction on this magnetic plug are described below.

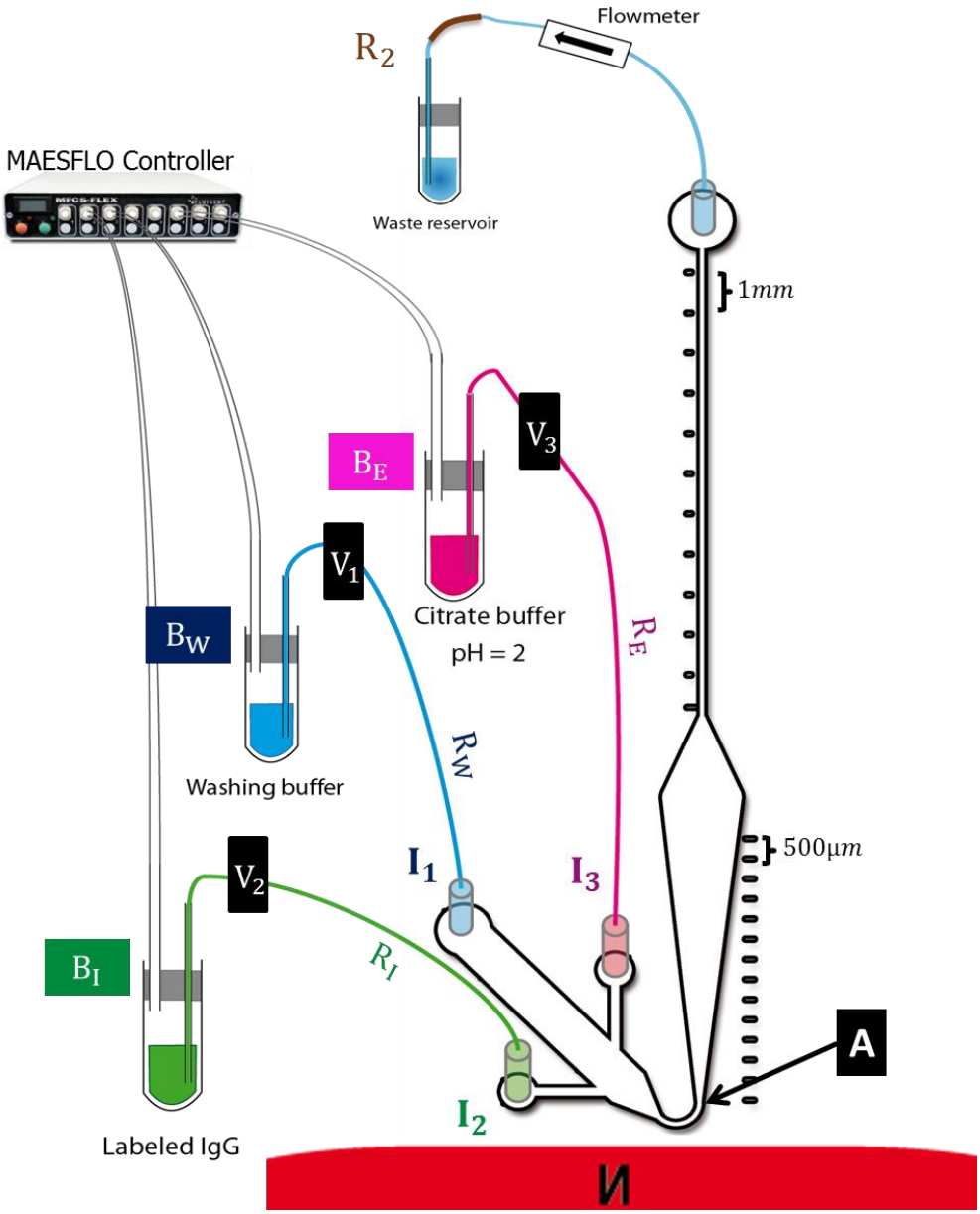

Figure III.3 : Schematic view of the whole microfluidic system, comprising the microchip, the permanent magnet, the valves, the MAESFLO and the accessories (sensor, reservoirs and silicon tubes) and the PEEK tubes connecting the different parts of system.

- Reservoirs:

B_E, Eluting buffer reservoir: citrate buffer (pH 2)

B_W, Washing buffer reservoir: PBS (1x), 0.1% BSA buffer (pH 7.4)

B_I, sample reservoir: either Alexa Fluor® 488 Rabbit Anti-Mouse IgG antibodies or mouse monoclonal IgG1anti-human CD1a.

- Valves:

Valve V_3 is associated to B_E

Valve V_1 is associated to B_W

Valve V_2 is associated toB_I

- Channel inlets:

$I_3$is connected to B_E via V_3

$I_1$is connected to B_W via V_1

$I_2$is connected to $B_I$via V_2

- Fluid paths :

Path B_E -I_3exhibits a resistance R_E, the total dead volume is $V_{B_E - I_3} = 22 \, L$.

Path B_W-I_1exhibits a resistance $R_W = R_E$, $V_{B_W - I_1} = 24 \, L$

Path B_I-I_2 exhibits a resistance R_I, $V_{B_I - I_2} = 22 \, L$

The three paths converge to A, the entrance of the main channel, which corresponds to the active area. In the first step, V_3 and V_2 are closed and the washing buffer is injected through path B_W-$I_1$to perfuse the plug. In the second step the labelled IgG solution is injected through the plug while V_1 and V_3 are closed. In the final step, V_1 and V_2 are closed to allow injection of the elution buffer. It is worthy to note that each valve has been first calibrated to evaluate its swept volume, and thus to determine the appropriate volume of solution to be used at each step.

The connecting tubes (PEEK tube, diameter250 μm) have been selected to avoid any perturbation of the system of flow measurement and consequently to control precisely the volumes injected. Indeed, PEEK is a rigid material that limits the buildup of long-standing back-pressure. Moreover, because of its chemical inertia, negligible adsorption of protein occurs on the tube walls. This has been proven using BSA solution in PEEK and silicon tubes after one hour of incubation, we found that BSA adsorbed strongly on the silicon tube walls while it did not with PEEK tubes.

The MAESLO controller enables a full and accurate control of the injected volumes. This equipment allows an auto-calibration of the microfluidic device which means that the whole resistance of the system is initially calculated. By this way, the flow rate can be set and remains stable in the configuration of the system previously calibrated. Any perturbation due to bubbles or dust coming into the system via the reservoir can be visualised on the panel (see Figure III.4). For all reasons, the solutions involved in sample processes have to be eventually filtered and degased using either vacuum or sonication.

The MAESFLO interface allows on line control of the injected volume from any reservoir. This tool is very useful for our application system because of its ability to maintain a zero flow rate together with a finite pressure, and consequently to prevent the microparticles to move back to their equilibrium location under the effect of the applied magnetic field (see Figure III.4).

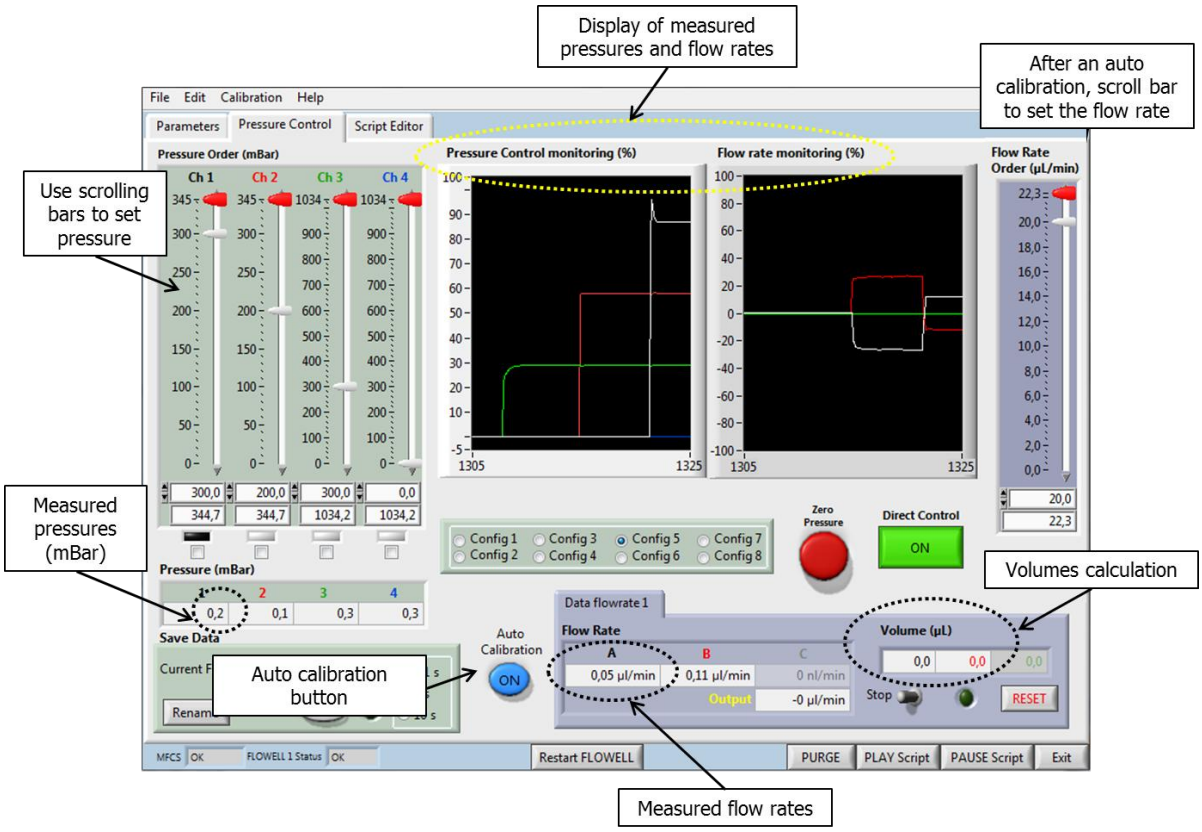

Figure III.4: Pressure Controller panel of the MAESFLO software. Pressure or Flow rate can be controlled, for example, Ch1 channel and a sensor, respectively.

The different steps of the immunoextraction to be integrated are:

- Washing procedure of the microparticles
- Sample incubation
- Washing to remove unbound biomolecules
- Elution of the isolated target

b. Optimisation of the on-chip immunoextraction

Prior to any experiments, the microfluidic chips are coated with PDMA-AGE polymer[18], in order to prevent microparticles and protein from adsorption on the channel surface [158]. It has been recently shown that the use of such hydrophilic and neutral polymer drastically decrease both protein adsorption and electroomostic flow [159]. This channel coating process is very simple a solution of this polymer (0.15 % w/w) is injected in the microchannel just after the channel oxidation by plasma. The polymer was then incubated for 30 min and subsequently washed out with PBS containing 0.1% of BSA.

Once the whole microfluidic system is prefilled with the PBS/BSA buffer, the system is thus ready to use for the sample processing. The temperature is kept at 20°C throughout the experiment.

The labelled IgG solution and citrate buffer is pipetted in reservoirB_I and B_E respectively. The auto-calibration of the microfluidic device is achieved and the response of the system is checked out via the panel controller. The solution of labelled IgG is injected till the inlet $I_2$of microchip, the distance between I_2 and the main channel (at the point A) is long enough to ovoid the diffusion effect before to start the injection of IgG into the plug.

The initial trapping of microparticles in the microchip is one of the most important steps of the assay protocol, since the number of microparticles has to be well-defined (immunosupport capacity) to perform reproducible experiments. To provide an optimal microparticles trapping, several strategies have been investigated and the most efficient one is described below. First, the Inlet I_3 is disconnected and replaced by a pipette tip. By applying a pressure on the reservoir B_W, this pipette tip is filled with PBS, Dynabeads suspension (5 μL) is thus directly injected in it (see Figure III.5). Sedimentation causes the particles to enter the channel where they are trapped due to the applied magnetic field. Some microparticles could adsorb on the tip surface but they can be easily pulled towards to the active area with an additional permanent magnet. Once the solution in the pipette tip looks clear (we assumed that all the microparticles have been efficiently injected in the microchip), the tip is then removed, the inlet I_3 is reconnected and a pressure is applied on the reservoirs B_W and B_E while the PEEK tubes are reconnected, using droplet merging to avoid loading air bubbles within the microfluidic device.

[18] This polymer was a kind gift of M. Chiari (Milano, Italy).

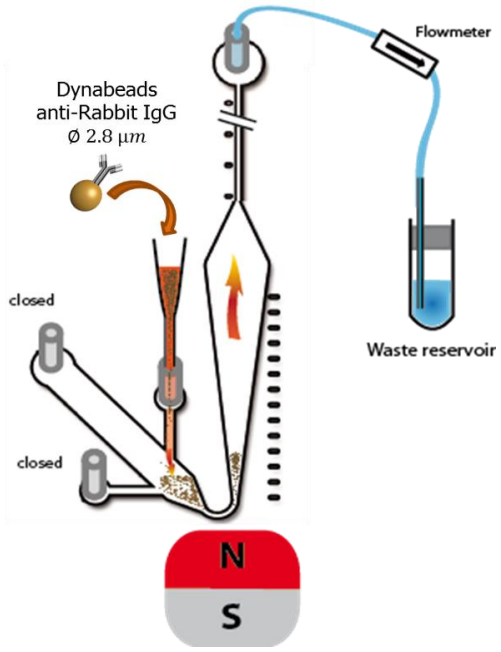

Figure III.5: Injection of the microparticles using plastic pipette tip and incipient plug or plug formation or plug-forming make up of Dynabeads coated with antibodies (IgG).

Afterwards, a washing step (using PBS/BSA) is performed to equilibrate the immunosupport. This washing step is essential for two reasons (see Figure III.6). First, the remaining microparticles in the injection channel are pushed towards the active area. Secondly, during this washing step and due to the applied pressure ($70\,mbar$; $2\,\mu L/min$) the microparticles undergo a transition from the packed to the fluidized regime so that eventual aggregates are completely broken. Moreover, the fluidized regime allows an efficient washing of the microparticles.

Some microparticles are retained on the curved walls but the corresponding amount of those microparticles is negligible compared to the amount of the plug forming microparticles. It is worth noting that even if the whole curved channel would be completely filled with microparticles, their volume represents only 5% of the plug volume.

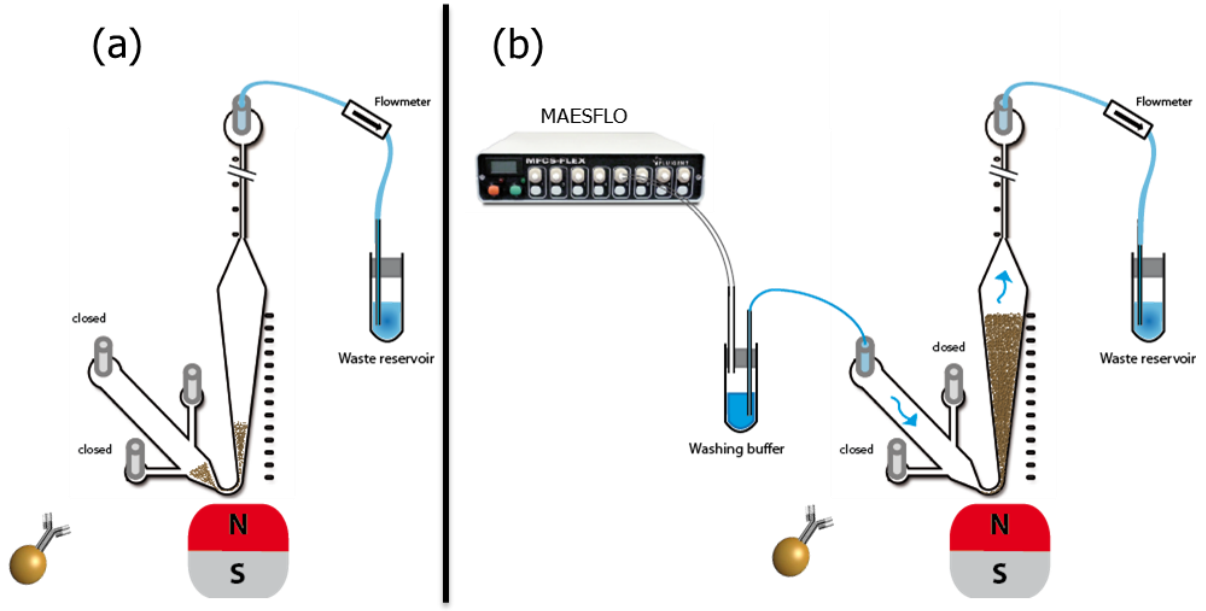

Figure III.6: Bed preparation: (a) injection of the magnetic particles. (b) washing and homogenisation of the bed in the defined active area.

Figure III.7.a depicts the immunocapturing step. In this step, the sample solution that contains a specific labelled IgG (or a non-specific mouse IgG1 to evaluate the capture specificity) is perfused at a flow rate of 1 $\mu L/min$. Subsequently, the unbound compounds are dragged away through a washing procedure by injectinga 20 μL of PBS/BSA buffer solution at flow rate of 2 $\mu L/min$ (Figure III.7.b).

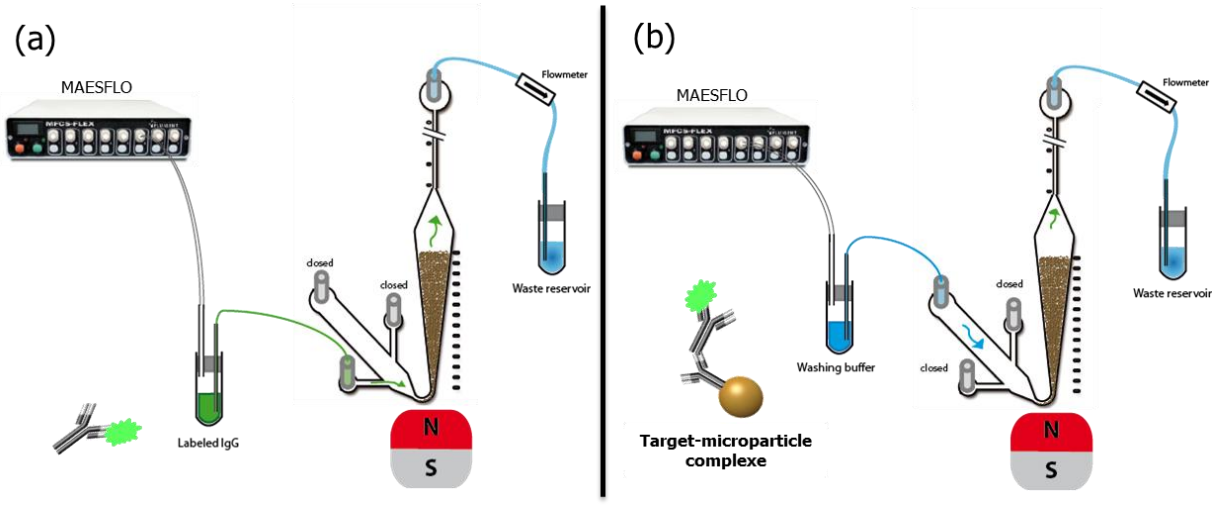

Figure III.7: (a) Injection of the labelled IgG. (b) Washing step to remove unbound Ag.

Figure III.8 illustrates the elution step during which is a citrate buffer is injected at a flow rate of 0.5 $\mu L/min$. This step is criticalto achieve the highest sensitivity. Different approaches of elution have been investigated. The first approach is a conventional continuous elution, during which a volume of 20 μL was percolated through the immunosupport at a flow rate of 0.5 $\mu L/min$. Besides we also investigated the possibility to take benefit of the two different

immunosupport regimes. To this end, a first volume of citrate buffer ($2\,\mu L$) was flown through the immunosupport in a fluidized bed regime (flow rate $0.5\,\mu L/min$ during $2\,min$). In a second step, the flow rate was set at $0\,\mu L/min$ during 10 min, the immunosupport being in a packed bed regime. The flow stoppage should give more time to dissociation to occur, improving the overall process of the target recovery. It can also be expected that performing the elution in packed bed regime should limit the target dispersion and consequently improve the assay sensitivity. The last step of this stop-and-go elution consists in reactivating the fluidization regime during 2 minutes to release the captured targets. The amount of eluted IgG is then detected in the detection channel and quantified by fluorescence.

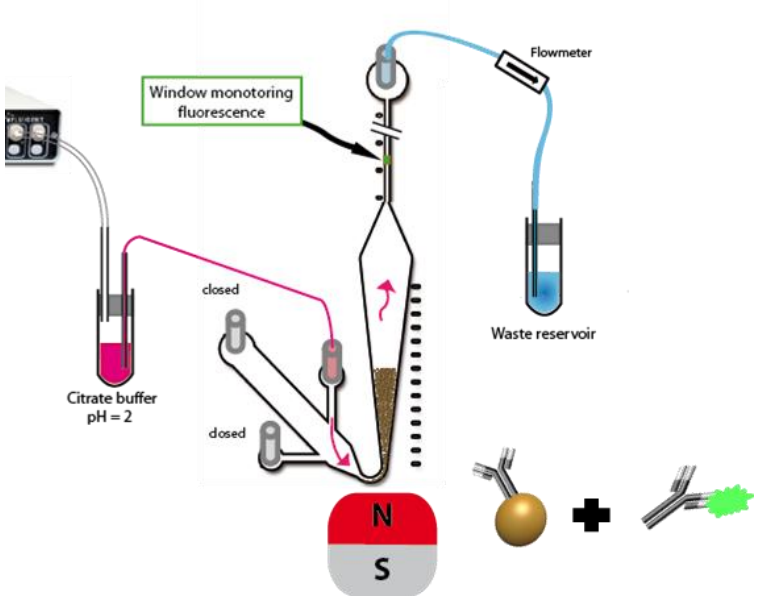

Figure III.8: Elution step to release the isolated labelled IgG and direct fluorescence detection.

5. Results and discussion

As the different steps of the immunoextraction take place under different magnetic plug regimes, we have first estimated the volume occupied by a given amount of functionalized beads ($50\,\mu g$) as a function of the applied flow rate. This will give us information on the plug porosity as well as a first estimation of Ab/Ag complex dispersion for each immunoextraction step. Figure III.9 shows a picture of the plug of anti-IgG magnetic beads in the main channel at a flow rate of $2\,\mu L/min$. In this situation, the magnetic plug is in a fluidized regime like during the washing step. Parameters ℓ and w are the plug length and width, respectively. These are measured at each flow rate and enable to estimate the apparent volume of the plug. The constant parameters b and h are respectively the curved channel width and the microchip height.

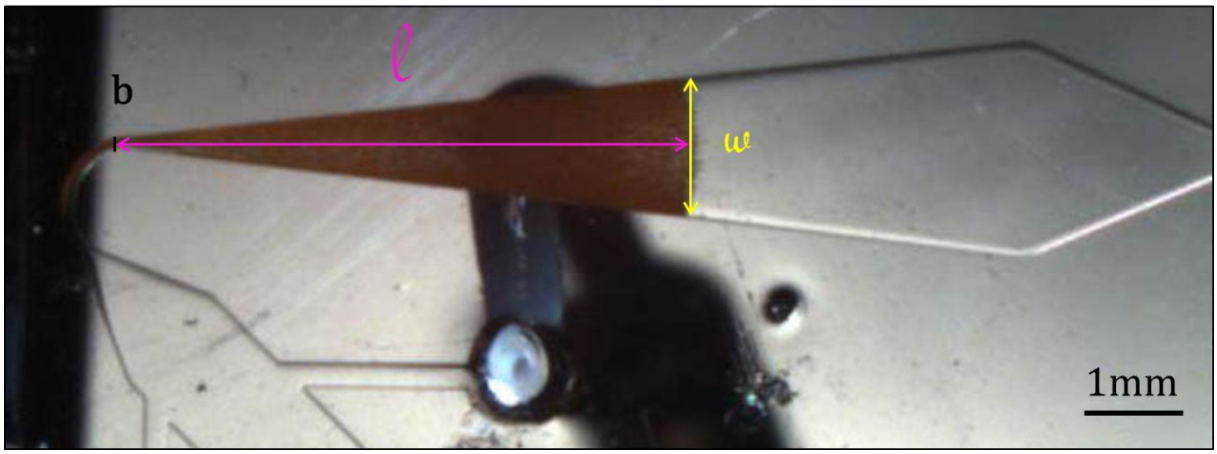

Figure III.9: Picture of the plug in a fluidization state at a flow rate of 2 $\mu L/min$ in the main channel.

The apparent volume of the plug at different flow rates was measured using the ImageJ software.

Flow rate $(\mu L/min)$	Plug width $w(mm)$	Length of plug $\ell(mm)$	**Volume of plug** V_{plug} (mm^3)	**Processing step**
0	0,752	2,942	0,063	**"stop"** elution (citrate injection)
0.5	0,979	4,073	0,110	**"go"**elution / Continuous elution
1	1,051	4,496	0,129	**Immunocapture**
2	1,178	5,061	0,162	Washing

Table 2: Table representing the apparent volume of the plug at different setting flow rates and at different processing steps.

These results show that during the different steps of the bioanalytical assay the plug volume varies from $0.06\,mm^3$ to approximately $0.16\,mm^3$. The immune-complex dispersion is directly related to this apparent volume variation. One can thus expect a sharper eluting band when performing a stop-and-go elution compared to a continuous one.

To confirm this assumption we compared the performances of both elution modes. For that purpose, we achieved two experiments. First the immunosupport was incubated with 20 μL of labelled IgG (100 ng/mL). This incubation was done at 1 $\mu L/min$. As previously mentioned, the magnetic plug behaves as fluidized bed at this flow rate and the whole beads surface is accessible, increasing the surface to volume ratio while the beads recirculation should favour the mixing. After one washing step, also performed in fluidized bed regime, the elution was carried out using a continuous flow or a stop-and-go mode.

Figure III.10 shows the elution peak obtained by fluorescence measurement during the continuous elution ($50\ min$). A large band ($6\ min$) with 100 a.u. height is obtained and the signal to noise ratio is about 20.

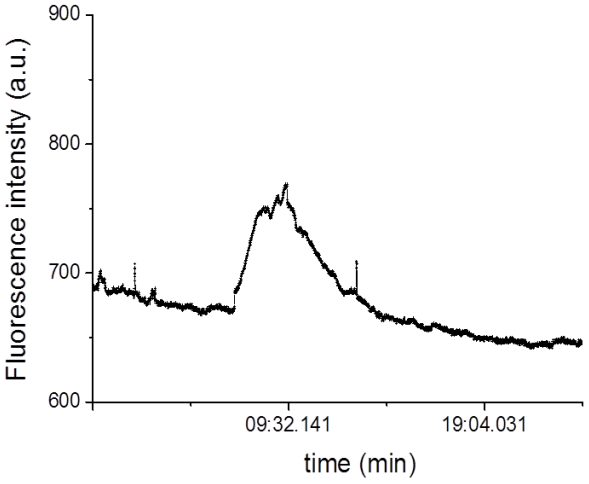

Figure III.10: Continuous elution mode at a flow rate of $0.5\ \mu L/min$ during $50\ min$. A band width of $6\ min$ (exposure time 1 s, gain x2, digital Nikon camera Sight DS-Qi1Mc, 40 X objective).

Similar experiments have been carried out with stop-and-go mode. The fluorescence signal was measured during $2\ min$ with a latent time of $10\ min$ once the microchip was filled up with $2\ \mu L$ of the citrate buffer (pH 2). Four successive elutions were carried out. As expected the four elution peaks are sharper than the one obtained by continuous elution while their intensity decreases as the number of elution steps increases (Figure 12). In terms of analytical performance, the peak intensity of the first elution is 3 times higher than the one obtained by continuous elution leading to a signal to noise ratio almost 3.5 higher. Table 1 has shown that the difference of Ag/Ab dispersion along the x-axis is about 1.5 ($0.5\ \mu L/min$ compared to $0\ \mu L/min$) even though the band width is about 6 times decreased using a stop-and-go elution compared to the continuous elution mode. Several hypotheses can be considered to explain this sensitivity improvement:

- reduction of the initial dispersion of the Ag/Ab complex
- enhancement of the elution recovery
- longer interaction between the complex and the eluent (by giving more time to the dissociation to take place)

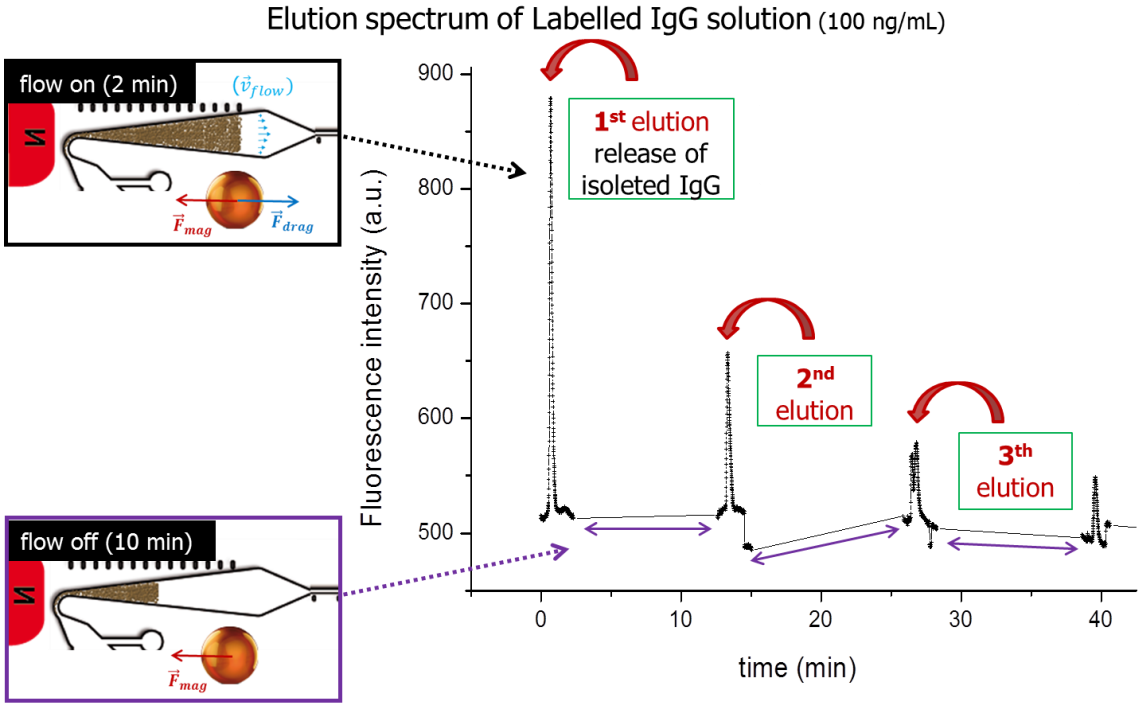

Figure III.11: stop-and-goelution mode. Four successiveelutions. Detections parameters: exposure time 1 s and gain x2.

Finally, it can be concluded that due to the lowest dispersion of the immunosupport combined to a better elution recovery, the stop-and-gomode greatly increases the assay sensitivity as compared to continuous elution (Figure III.10).

Now, to evaluate the immunoextraction specificity, a non-specific target (Alexa-human IgG1) was used. This experiment was performed at a high concentration of the target in order to favour non-specific adsorption. Figure III.12shows that even at high concentration of the non-specific IgG, no peak was observed during a continuous elution mode. This proves that this on-chip magnetic beads based-immunoextraction is highly specific.

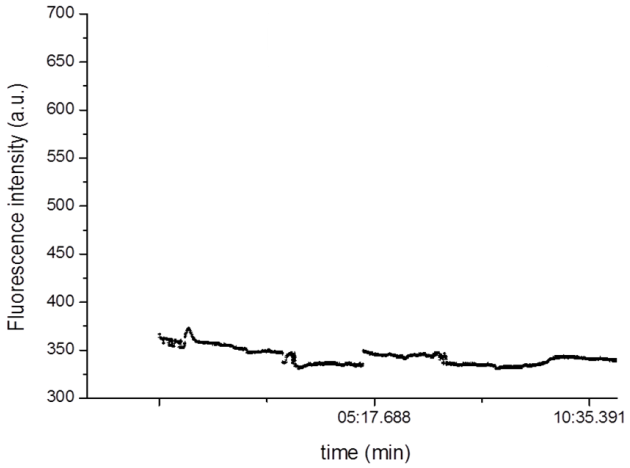

Figure III.12: Elution spectrum of labelled IgG1 (CD1a) solution at $\mathbf{20\mu g/mL}$(0.4 μg).

Finally, these experiments demonstrated the versatility of this immunosupport in terms of elution mode as well as its specificity. After this first proof of concept of such dynamic plug based immunoextraction, we investigated its ability to analyse low concentrated sample.

The firstexperiment was performed by injecting20 μL of a labelled IgG solution at10 ng/mL. The latter represents an amount of 0.2 ng labelled IgG. The experiments were performed using a stop-and-goelution (Figure III.13). In this case, due to a low signal to noise ratio only three elution steps were performed. The signal/noise ratio is 7.5, one can thus expect being able to detect very low concentrations.

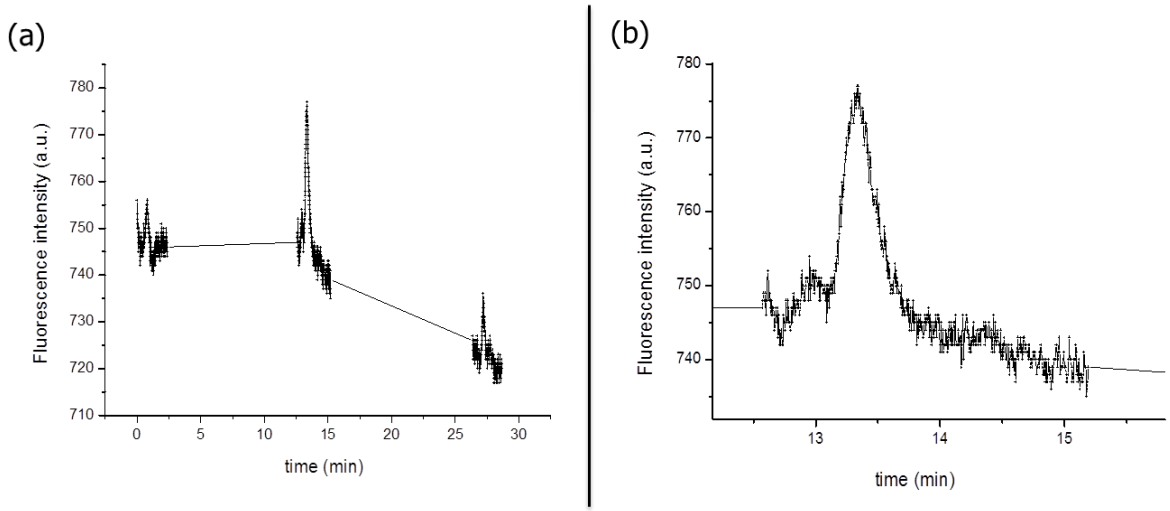

Figure III.13: (a) Elution spectrum of labelled IgG solution at $\mathbf{10\ ng/mL}$. (b) Enlarged view of the second peak. Detections parameters: exposure time 1 s and gain x2

We thus evaluated the possibility to analyse a sample of lower IgG concentration. For that, a labelled IgG solution (20 μL, 5 ng/mL, 0.1 ng) was injected. As shown in Figure III.13, the signal to noise ratio was too low and thus any peak can be detected.

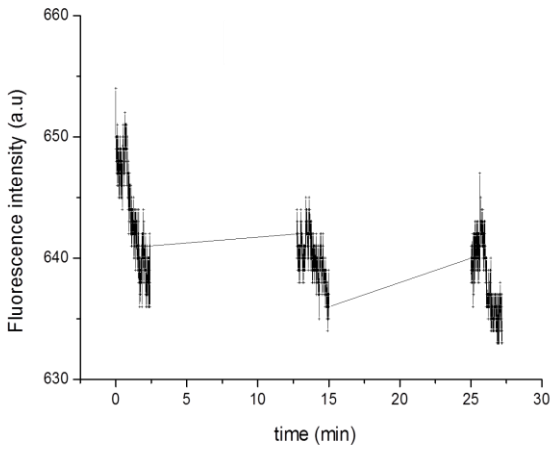

Figure III.14: Elution spectrum of labelled IgG solution at **5 ng/mL**.

These results show that the limit of detection is ranging from 10 to 5 ng/mL (70 to 35 pM), for an injected volume of 20 μL.

As previously mentioned, this work was part of a European project. The objective of this project was to detect low concentrated biomarker in large volume of patient serum. We were interested in investigating the performance of this dynamic plug-based immunoextraction to analyse larger volume of sample. We already showed that an injected amount of 0.2 ng in 20 μL of labelled IgG solution (10 ng/mL) can be detected (S/N: 7.5). To evaluate the possibility to extract biomarkers at low concentration in large volume of sample, we performed the similar experiment injecting the same amount of IgG (0.2 ng) by injection a solution at a lower concentration (1 ng/mL) but in a ten-fold to be injected volume (200 μL) (Figure III.15).

As shown in figure 15, we observed approximately the same fluorescence intensity (S/N: 10) in both cases. This means the injected volume are not limiting but that the signal intensity mainly depends on the initial target amount in the sample. When injecting a 6 pM solution (200 μL), the target can be detected with a fluorescence signal to noise ratio around 10. These experiments demonstrate the ability of this integrated immunoextraction to analyse large volume of sample with a high sensitivity.

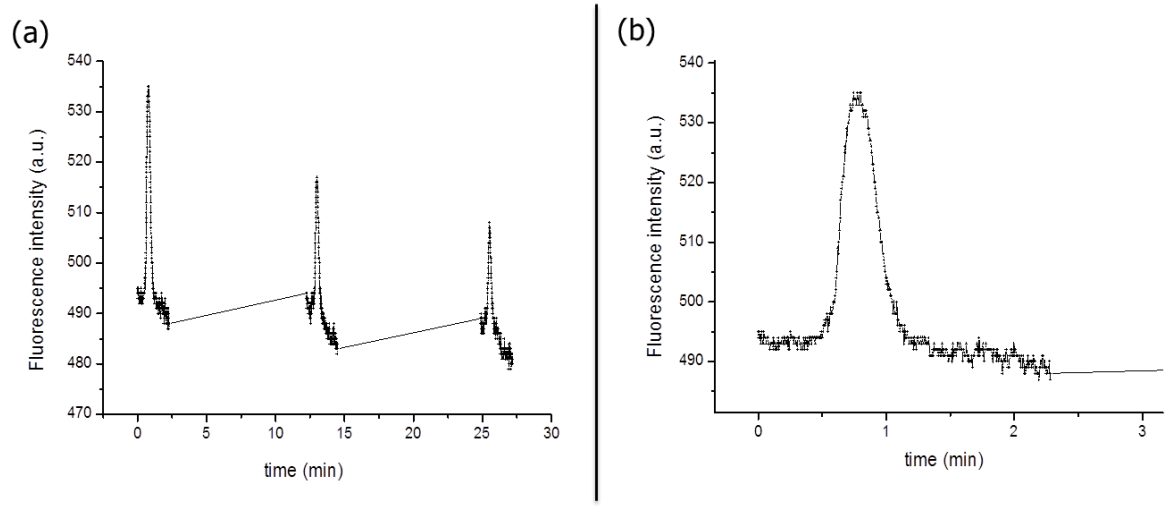

Figure III.15: (a) Elution spectrum of labelled IgG solution at $\mathbf{1}\ \boldsymbol{ng/mL}$. (b) Magnified view of the first peak.

To emphasize the performance using this new generation of magnetic plug, these results have been compared to a previous study in our team of R. Mohamadi[160]. This work was performed using the previous generation of magnetic plug with similar beads and target except that a higher amount of immunosupport (100 μg of beads) was used. Moreover, the targetelution was electrokinetically driven to limit target dispersion. And it can also be mentioned, that a further preconcentration step on a photopolymerized membrane was implemented. Finally, in spite of these favourable conditions the limit of IgG detection was around 100 ng/mL[160]. Thiscomparisonhighlights the potential of our new dynamic magnetic plug for large sample bioanalysis as both large volume samples can be handled and very low limits of detection can be achieved.

6. Preliminary conclusion

We showed the possibility to use this dynamic plug to perform an efficient immunoextraction of model biomolecules by taking benefit of the different regimes of the bed. In order to improve the surface to volume ratio while allowing a uniform mixing, the immunocapture step was performed in a fluidized bed regime. On the contrary, to improve the elution efficiency, the target was eluted according to a stop-and-go mode based on both packed bed and fluidized bed regimes. We thus demonstrated the ability of such dynamic plug to extract specifically biomolecules of interest from a large volume (200 μL) of sample and with a high sensitivity (6 pM). These experiments were performed at flow rate ranging from 0.5 to 2 $\mu L/min$ which is compatible with the analysis of large volume samples.

In order to further characterize this dynamic immunoextraction, a calibration curve should be established, especially to determine precisely the limit of detection as well as the dynamic range. Even if this preliminary study reports satisfying reproducibility, this aspect should be further evaluated. Moreover, in a near future we would like to deal with real

samples analysis, for example by spiking human serum with labelled IgG in order to study the sample matrix effect on these analytical performances. Finally to get better assay sensitivity, we intend to replace this hydrodynamic elution with an electrodriven one. Indeed, an electrokinetic elution should limit the analyte dispersion due to Poiseuille flow and thus improve the assay sensitivity.

In mid-terms perspectives, a transfer of this microfluidic technology to real samples analysis is desired, in the AD diagnosis context, to analyse Aβ peptides. These peptides are produced during the partial transmembrane protein hydrolysis. This proteolytic reaction produces a cocktail of Aβ peptides with different sizes in measurable and stable ratios of healthy patients. In contrary, AD patients exhibit a selective decrease of $A\beta_{41\text{-}42}$ in CSF while $A\beta_{40\text{-}41}$ was reported as biomarker to distinguish different types of dementia disorders [161], [162]. Thus, it would be interesting to combine an efficient immunoextraction of these peptides with an electrokinetic separation to evaluate the relative concentration of these different peptides even if they are initially present at very low concentration in blood.

Finally, due to its high versatility this dynamic magnetic plug could be used for various bioanalytical applications. From a general point view, it could be interesting to compare the achieved performance using this fluidized bed to conventional packed bed in the context of enzymatic digestion or sandwich immunoassay. We also intend to combine this efficient platform for immunoextraction to a droplet compartmentalization to practice subsequent bioassays.

Conclusion

We have developed a new microfluidic component, in which magnetic particles are maintained dynamically in a microchamber, and undergo hydrodynamic recirculation. From a physics point of view, this relatively dense dynamical system is reminiscent of fluidized beds, and its behaviour has been interpreted in this frame. Magnetically stabilized fluidized beds had been used in the macroscopic world, but to our knowledge, this is the first implementation of this principle in microfluidics, in which gravitational fluidized beds would be very limited in dynamic range. Previous systems using magnetic microparticles in microfluidics consisted in i/ either low density static or dynamic systems, with a low capacity and efficiency, or ii/ static systems in which "microcolumns" are trapped in a strong and local field potential. The latter systems have a higher potential capacity, but a limited capture efficiency (when the microchannel remains partly open), or a very limited flow throughput (when the magnetic plug is compact and blocks the channel). The new system developed here bridges the gap between these two previous strategies, and opens new regimes of operation combining a relatively high density of magnetic particles, for high capacity, an active hydrodynamic stirring, for increased kinetics, and a relatively high flow rate, allowing concentration of very dilute analytes from a rather large sample volume.

This system was validated in an immunoassay, using a stop-and-go strategy taking full advantage of the dynamic nature of the magnetic microcolumn. We believe, however, that it also has strong potential of preconcentration of analytes from ml-sized samples to µl or even nl –sized downstream microfluidic analysis modules. Developments in this direction will be made in the laboratory. In particular, this laboratory is involved in the European project Nadine, aimed at developing early diagnosis of Alzheimer's disease in blood. We believe that the present microcolumn will be very useful in this project, since because of the blood-brain barrier, at least some important biomarkers of neurodegenerative diseases risk to be present at a very low concentration(pM or sub-pM), and will thus require a preconcentration step.

Appendix

Flux control in microfluidics, is generally provided with a syringe pump or a peristaltic pump. However, these systems have numerous disadvantages as long as the pipingnetwork is becoming complex: long relaxation time and difficulty in equilibrating the flux inside the pipes. To circumvent these drawbacks, an automated pressure controller was used.

The global schema of operation is depicted in Figure A.1, in the simple case where the inlet pressure of the micro-channel while the outlet reservoir open[163]. In this schema, R_v isthe flow resistance of the computer controlled electro-valve, R_l is the flowresistance of the calibrated leak. $R_v$andR_l represent a pressure divider network and R_c represents the flow resistance of the microchannel. $R_l$andR_v aretypically much smaller than R_c. V_1represents the volume of the pressurereservoir, tubing and connectors. The right-hand pictures shows an eight inlet-controller marketed by Fluigent Company®. This box contains the integrated pressure control system, including the leakage valves and the pressure sensors.

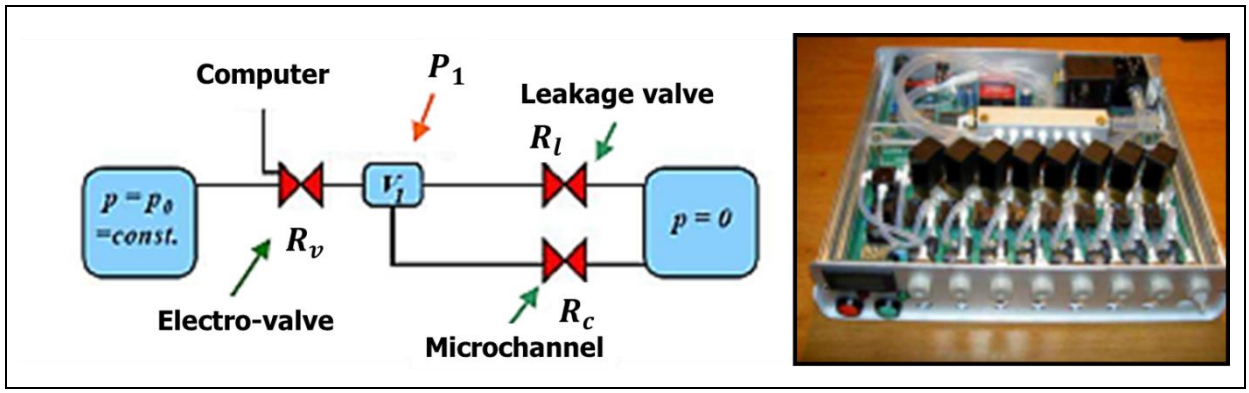

Figure A: (1) Schematic representation of a single channel control device. (2) Pressure control unit. (adapted from [163].

The working principle is based on the hydrodynamic equivalent of a voltage divider: voltage↔ pression; intensity ↔ flux. The inlet resistance of the dividing arrangement (R_v) is adjusted by a computer controlled system. A leakage allows to control the outlet resistance R_0, to reduce pressure till atmospheric one, chosen as reference zero pressure. The microchannel inlet pressure (denotedP_1) is then:

$$P_1 = P_0 \frac{R_l}{R_l + R_v}$$

In this equation, the hydrodynamic resistance of the channel, R_c is does not interfere since it is much larger than the other resistances of the system. Nevertheless, the flux inside the channel,Q_c, is imposed by P_1 and R_c values via the Poisseuille's law:

$$P_1 = Q_c R_c$$

The controlled pressure is, however, subject to fluctuations due, for example, to change in the hydrodynamic resistance of the channel (partially blocked channel). To avoid these undesired effects, a pressure sensor is positioned downstream of the valve which provides the pressure measure upstream of the channel, to the computer which regulates the value to maintain a strictly constant pressure. A Labview interface is used to drive the system from a computer.

More quantitatively, based on a dynamic control of reservoir pressures at the end of each channel and external thermal flow-sensors, all the parameters are measured with a precision down to $25\,\mu Bar$ and $2\,nL/min$. The MAESFLO can control either the flow rate or the pressure with high stability over long period whatever the microsystem characteristics through to adaptive feedback control loop. Moreover, pressure control enables to achieve short response time, less than hundreds of millisecond and by combining pressure actuation with a flowrate monitoring,a short response time isfeasible keeping a high precision flow rate.

This system could be multiplexed as shown in the right picture (Figure A.2), the inlet, pressures through the piping network set, could be precisely controlled independently of each other.

References

[1] A. Le Nel, N. Minc, C. Smadja, M. Slovakova, Z. Bilkova, J.-M. Peyrin, J.-L. Viovy, and M. Taverna, "Controlled proteolysis of normal and pathological prion protein in a microfluidic chip.," *Lab on a chip*, vol. 8, no. 2, pp. 294–301, Feb. 2008.

[2] Q. Ramadan and L. T. Ting, "Reconfigurable Translocation of Microbeads Using Micro-Engineered Locally Controlled Magnetic Fields," *Journal of Microelectromechanical Systems*, vol. 20, no. 6, pp. 1310–1323, Dec. 2011.

[3] A.-L. Gassner, J. Morandini, J. Josserand, and H. H. Girault, "Ring magnets for magnetic beads trapping in a capillary," *Analytical Methods*, vol. 3, no. 3, p. 614, 2011.

[4] A. J. Martin and R. L. Synge, "A new form of chromatogram employing two liquid phases: A theory of chromatography. 2. Application to the micro-determination of the higher monoamino-acids in proteins.," *The Biochemical journal*, vol. 35, no. 12, pp. 1358–68, Dec. 1941.

[5] H. G. KUNKEL and A. TISELIUS, "Electrophoresis of proteins on filter paper.," *The Journal of general physiology*, vol. 35, no. 1, pp. 89–118, Sep. 1951.

[6] S. C. Terry, J. H. Jerman, and J. B. Angell, "A gas chromatographic air analyzer fabricated on a silicon wafer," *IEEE Transactions on Electron Devices*, vol. 26, no. 12, pp. 1880–1886, Dec. 1979.

[7] G. M. Whitesides, "The origins and the future of microfluidics.," *Nature*, vol. 442, no. 7101, pp. 368–73, Jul. 2006.

[8] N.-T. Nguyen and S. T. Wereley, *Fundamentals and Applications of Microfluidics*. Artech Print on Demand, 2002, p. 497.

[9] L. J. Thomas and S. P. Bessman, "Prototype for an implantable micropump powdered by piezoelectric disk benders.," *Transactions - American Society for Artificial Internal Organs*, vol. 21, pp. 516–22, Jan. 1975.

[10] W. J. Spencer, W. T. Corbett, L. R. Dominguez, and B. D. Shafer, "An electronically controlled piezoelectric insulin pump and valves," *IEEE Transactions on Sonics and Ultrasonics*, vol. 25, no. 3, pp. 153–156, May 1978.

[11] P. Woias, "Micropumps—past, progress and future prospects," *Sensors and Actuators B: Chemical*, vol. 105, no. 1, pp. 28–38, Feb. 2005.

[12] P. Tabeling, *Introduction toMicrofluidics*. New York: Oxford University Press Inc, 2003.

[13] J. C. Mcdonald, D. C. Duffy, J. R. Anderson, and D. T. Chiu, "Review General Fabrication of microfluidic systems in poly (dimethylsiloxane)," 2000.

[14] H. Becker and L. E. Locascio, "Polymer microfluidic devices.," *Talanta*, vol. 56, no. 2, pp. 267–287, 2002.

[15] T. Vilkner, D. Janasek, and A. Manz, “Micro total analysis systems. Recent developments.,” *Analytical chemistry*, vol. 76, no. 12, pp. 3373–85, Jun. 2004.

[16] P. S. Dittrich, K. Tachikawa, and A. Manz, “Micro total analysis systems. Latest advancements and trends.,” *Analytical chemistry*, vol. 78, no. 12, pp. 3887–908, Jun. 2006.

[17] D. Brambley, B. Martin, and P. D. Prewett, “Microlithography: An overview,” *Advanced Materials for Optics and Electronics*, vol. 4, no. 2, pp. 55–74, Mar. 1994.

[18] J. C. McDonald and G. M. Whitesides, “Poly(dimethylsiloxane) as a material for fabricating microfluidic devices.,” *Accounts of chemical research*, vol. 35, no. 7, pp. 491–9, Jul. 2002.

[19] J. W. Hong and S. R. Quake, “Integrated nanoliter systems.,” *Nature biotechnology*, vol. 21, no. 10, pp. 1179–83, Oct. 2003.

[20] D. B. Weibel, M. Kruithof, S. Potenta, S. K. Sia, A. Lee, and G. M. Whitesides, “Torque-actuated valves for microfluidics.,” *Analytical chemistry*, vol. 77, no. 15, pp. 4726–33, Aug. 2005.

[21] N.-T. Nguyen and Z. Wu, “Micromixers—a review,” *Journal of Micromechanics and Microengineering*, vol. 15, no. 2, pp. R1–R16, Feb. 2005.

[22] A. Günther, M. Jhunjhunwala, M. Thalmann, M. A. Schmidt, and K. F. Jensen, “Micromixing of miscible liquids in segmented gas-liquid flow.,” *Langmuir : the ACS journal of surfaces and colloids*, vol. 21, no. 4, pp. 1547–55, Feb. 2005.

[23] P. Garstecki, M. A. Fischbach, and G. M. Whitesides, “Design for mixing using bubbles in branched microfluidic channels,” *Applied Physics Letters*, vol. 86, no. 24, p. 244108, Jun. 2005.

[24] D. J. Laser and J. G. Santiago, “A review of micropumps,” *Journal of Micromechanics and Microengineering*, vol. 14, no. 6, pp. R35–R64, Jun. 2004.

[25] T. Thorsen, S. J. Maerkl, and S. R. Quake, “Microfluidic large-scale integration.,” *Science (New York, N.Y.)*, vol. 298, no. 5593, pp. 580–4, Oct. 2002.

[26] H. a. Stone, a. D. Stroock, and a. Ajdari, “Engineering Flows in Small Devices,” *Annual Review of Fluid Mechanics*, vol. 36, no. 1, pp. 381–411, Jan. 2004.

[27] T. M. Squires, “Microfluidics : Fluid physics at the nanoliter scale,” vol. 77, no. July, 2005.

[28] D. J. Beebe, G. a Mensing, and G. M. Walker, “Physics and applications of microfluidics in biology.,” *Annual review of biomedical engineering*, vol. 4, pp. 261–86, Jan. 2002.

[29] P.-A. Auroux, D. Iossifidis, D. R. Reyes, and A. Manz, “Micro total analysis systems. 2. Analytical standard operations and applications.,” *Analytical chemistry*, vol. 74, no. 12, pp. 2637–52, Jun. 2002.

[30] D. R. Reyes, D. Iossifidis, P.-A. Auroux, and A. Manz, “Micro total analysis systems. 1. Introduction, theory, and technology.,” *Analytical chemistry*, vol. 74, no. 12, pp. 2623–36, Jun. 2002.

[31] J. West, M. Becker, S. Tombrink, and A. Manz, “Micro total analysis systems: latest achievements.,” *Analytical chemistry*, vol. 80, no. 12, pp. 4403–19, Jun. 2008.

[32] A. Arora, G. Simone, G. B. Salieb-Beugelaar, J. T. Kim, and A. Manz, "Latest developments in micro total analysis systems.," *Analytical chemistry*, vol. 82, no. 12, pp. 4830–47, Jun. 2010.

[33] G. B. Salieb-Beugelaar, G. Simone, A. Arora, A. Philippi, and A. Manz, "Latest developments in microfluidic cell biology and analysis systems.," *Analytical chemistry*, vol. 82, no. 12, pp. 4848–64, Jun. 2010.

[34] L. Gervais, N. de Rooij, and E. Delamarche, "Microfluidic chips for point-of-care immunodiagnostics.," *Advanced materials (Deerfield Beach, Fla.)*, vol. 23, no. 24, pp. H151–76, Jun. 2011.

[35] J. M. Hicks and M. Iosefsohn, "Reliability of home pregnancy-test kits in the hands of laypersons.," *The New England journal of medicine*, vol. 320, no. 5, pp. 320–1, Feb. 1989.

[36] W. Frank, *Viscous Fluid Flow*. United States: McGraw-Hill, 2005.

[37] D. B. Weibel, M. Kruithof, S. Potenta, S. K. Sia, A. Lee, and G. M. Whitesides, "Torque-Actuated Valves for Microfluidics place ; on curing , it bonds to the surrounding layer of of the threads of the screws . The valves were separated," vol. 77, no. 15, pp. 4726–4733, 2005.

[38] A. Hatch, A. E. Kamholz, K. R. Hawkins, M. S. Munson, E. A. Schilling, B. H. Weigl, and P. Yager, "A rapid diffusion immunoassay in a T-sensor.," *Nature biotechnology*, vol. 19, no. 5, pp. 461–5, May 2001.

[39] C.-Y. Lee, C.-L. Chang, Y.-N. Wang, and L.-M. Fu, "Microfluidic mixing: a review.," *International journal of molecular sciences*, vol. 12, no. 5, pp. 3263–87, Jan. 2011.

[40] V. Hessel, H. Löwe, and F. Schönfeld, "Micromixers—a review on passive and active mixing principles," *Chemical Engineering Science*, vol. 60, no. 8–9, pp. 2479–2501, Apr. 2005.

[41] D. Ahmed, X. Mao, B. K. Juluri, and T. J. Huang, "A fast microfluidic mixer based on acoustically driven sidewall-trapped microbubbles," *Microfluidics and Nanofluidics*, vol. 7, no. 5, pp. 727–731, Apr. 2009.

[42] T.-D. Luong, V.-N. Phan, and N.-T. Nguyen, "High-throughput micromixers based on acoustic streaming induced by surface acoustic wave," *Microfluidics and Nanofluidics*, vol. 10, no. 3, pp. 619–625, Oct. 2010.

[43] M. Campisi, D. Accoto, F. Damiani, and P. Dario, "A soft-lithographed chaotic electrokinetic micromixer for efficient chemical reactions in lab-on-chips," *Journal of Micro-Nano Mechatronics*, vol. 5, no. 3–4, pp. 69–76, Feb. 2010.

[44] Y. Du, Z. Zhang, C. Yim, M. Lin, and X. Cao, "A simplified design of the staggered herringbone micromixer for practical applications.," *Biomicrofluidics*, vol. 4, no. 2, pp. 024105–024105–13, Jan. 2010.

[45] B. Xu, T. N. Wong, N.-T. Nguyen, Z. Che, and J. C. K. Chai, "Thermal mixing of two miscible fluids in a T-shaped microchannel.," *Biomicrofluidics*, vol. 4, no. 4, p. 44102, Jan. 2010.

[46] Y. C. Lam, H. Y. Gan, N. T. Nguyen, and H. Lie, "Micromixer based on viscoelastic flow instability at low Reynolds number.," *Biomicrofluidics*, vol. 3, no. 1, p. 14106, Jan. 2009.

[47] Y. Wang, J. Zhe, B. T. F. Chung, and P. Dutta, "A rapid magnetic particle driven micromixer," *Microfluidics and Nanofluidics*, vol. 4, no. 5, pp. 375–389, Jun. 2007.

[48] T. Tofteberg, M. Skolimowski, E. Andreassen, and O. Geschke, "A novel passive micromixer: lamination in a planar channel system," *Microfluidics and Nanofluidics*, vol. 8, no. 2, pp. 209–215, May 2009.

[49] W. Buchegger, C. Wagner, B. Lendl, M. Kraft, and M. J. Vellekoop, "A highly uniform lamination micromixer with wedge shaped inlet channels for time resolved infrared spectroscopy," *Microfluidics and Nanofluidics*, vol. 10, no. 4, pp. 889–897, Nov. 2010.

[50] C. Y. LEE, C. F. LIN, M. F. HUNG, R. H. MA, C. H. TSAI, C. H. LIN, and L. M. FU, "Experimental and numerical investigation into mixing efficiency of micromixers with different geometric barriers," *Materials science forum*, pp. 391–396, 2006.

[51] A. D. Stroock, S. K. W. Dertinger, A. Ajdari, I. Mezic, H. a Stone, and G. M. Whitesides, "Chaotic mixer for microchannels.," *Science (New York, N.Y.)*, vol. 295, no. 5555, pp. 647–51, Jan. 2002.

[52] D. Moon and K. B. Migler, "Forced assembly and mixing of melts via planar polymer micro-mixing," *Polymer*, vol. 51, no. 14, pp. 3147–3155, Jun. 2010.

[53] C.-H. Lin, C.-H. Tsai, and L.-M. Fu, "A rapid three-dimensional vortex micromixer utilizing self-rotation effects under low Reynolds number conditions," *Journal of Micromechanics and Microengineering*, vol. 15, no. 5, pp. 935–943, May 2005.

[54] R.-T. Tsai and C.-Y. Wu, "An efficient micromixer based on multidirectional vortices due to baffles and channel curvature.," *Biomicrofluidics*, vol. 5, no. 1, p. 14103, Jan. 2011.

[55] S. Hardt, H. Pennemann, and F. Schönfeld, "Theoretical and experimental characterization of a low-Reynolds number split-and-recombine mixer," *Microfluidics and Nanofluidics*, vol. 2, no. 3, pp. 237–248, Dec. 2005.

[56] M. Jain and K. Nandakumar, "Novel index for micromixing characterization and comparative analysis.," *Biomicrofluidics*, vol. 4, no. 3, p. 31101, Jan. 2010.

[57] L. M. Lanning, R. M. Ford, and T. Long, "Bacterial chemotaxis transverse to axial flow in a microfluidic channel.," *Biotechnology and bioengineering*, vol. 100, no. 4, pp. 653–63, Jul. 2008.

[58] S. W. Lee, D. S. Kim, S. S. Lee, and T. H. Kwon, "A split and recombination micromixer fabricated in a PDMS three-dimensional structure," *Journal of Micromechanics and Microengineering*, vol. 16, no. 5, pp. 1067–1072, May 2006.

[59] "Alar Ainla veebi kodu (Alar Ainla's home page)." [Online]. Available: http://www.ims.ut.ee/~alar/microtech/Ch1_2/.

[60] S. K. Sia and G. M. Whitesides, "Microfluidic devices fabricated in poly(dimethylsiloxane) for biological studies.," *Electrophoresis*, vol. 24, no. 21, pp. 3563–76, Nov. 2003.

[61] F. Grasset, N. Labhsetwar, D. Li, D. C. Park, N. Saito, H. Haneda, O. Cador, T. Roisnel, S. Mornet, E. Duguet, J. Portier, and J. Etourneau, "Synthesis and Magnetic Characterization of Zinc Ferrite Nanoparticles with Different Environments: Powder, Colloidal Solution, and Zinc Ferrite−Silica Core−Shell Nanoparticles," *Langmuir*, vol. 18, no. 21, pp. 8209–8216, Oct. 2002.

[62] G.W. Reimers and S.E. Khalfalla, “PRODUCTION OF MAGNETIC FLUIDS BY PEPTIZATION TECHNIQUES,” *U.S. Patent 3843540*, 1974.

[63] M. a. M. Gijs, “Magnetic bead handling on-chip: new opportunities for analytical applications,” *Microfluidics and Nanofluidics*, pp. 22–40, Oct. 2004.

[64] S. Chikazumi and S. H. Charap, *Physics of magnetism*, London : J. Wiley New York, 1964.

[65] N. Pamme, “Magnetism and microfluidics.,” *Lab on a chip*, vol. 6, no. 1, pp. 24–38, Jan. 2006.

[66] R.C. O’Handley, *Modern Magnetic Materials : Principles and Applications O’HANDLEY Robert C.:* . Librairie Lavoisier, 2000.

[67] A. Hubert and R. Schäfer, *Magnetic Domains: The Analysis of Magnetic Microstructures*. 1998.

[68] http://www.physics.ohio-state.edu/~humanic/p112_lecture12.pdf, “Electromagnetic Induction.” [Online]. Available: http://www.physics.ohio-state.edu/~humanic/p112_lecture12.pdf.

[69] “Magnetic Hysteresis Loop including the B-H Curve.” [Online]. Available: http://www.electronics-tutorials.ws/electromagnetism/magnetic-hysteresis.html.

[70] D. L. Leslie-Pelecky and R. D. Rieke, “Magnetic Properties of Nanostructured Materials,” *Chemistry of Materials*, vol. 8, no. 8, pp. 1770–1783, Jan. 1996.

[71] S. Sun, H. Zeng, D. B. Robinson, S. Raoux, P. M. Rice, S. X. Wang, and G. Li, “Monodisperse MFe 2 O 4 (M) Fe , Co , Mn) Nanoparticles,” vol. 4, no. 1, pp. 126–132, 2004.

[72] Q. Pankhurst, J. Connolly, S. Jones, and J. Dobson, “Applications of magnetic nanoparticles in biomedicine,” *Journal of Physics D: Applied Physics*, vol. 36, no. 13, pp. R167–R181, 2003.

[73] A.-H. Lu, E. L. Salabas, and F. Schüth, “Magnetic nanoparticles: synthesis, protection, functionalization, and application.,” *Angewandte Chemie (International ed. in English)*, vol. 46, no. 8, pp. 1222–44, Jan. 2007.

[74] D. Horák, M. Babic, H. Macková, and M. J. Benes, “Preparation and properties of magnetic nano- and microsized particles for biological and environmental separations.,” *Journal of separation science*, vol. 30, no. 11, pp. 1751–72, Jul. 2007.

[75] R. S. YALOW and S. A. BERSON, “Assay of plasma insulin in human subjects by immunological methods.,” *Nature*, vol. 184 (Suppl, pp. 1648–9, Nov. 1959.

[76] A. Hatch, E. Garcia, and P. Yager, “Diffusion-Based Analysis of Molecular Interactions in Microfluidic Devices,” *Proceedings of the IEEE*, vol. 92, no. 1, pp. 126–139, Jan. 2004.

[77] T.-K. Lim, H. Ohta, and T. Matsunaga, “Microfabricated on-chip-type electrochemical flow immunoassay system for the detection of histamine released in whole blood samples.,” *Analytical Chemistry*, vol. 75, no. 14, pp. 3316–3321, 2003.

[78] T. Tachi, N. Kaji, M. Tokeshi, and Y. Baba, “Microchip-based homogeneous immunoassay using a cloned enzyme donor.,” *Analytical sciences : the international journal of the Japan Society for Analytical Chemistry*, vol. 25, no. 2, pp. 149–51, Feb. 2009.

[79] A. E. Herr, J. I. Molho, K. A. Drouvalakis, J. C. Mikkelsen, P. J. Utz, J. G. Santiago, and T. W. Kenny, "On-Chip Coupling of Isoelectric Focusing and Free Solution Electrophoresis for Multidimensional Separations the total IEF channel length was completed in less than," vol. 75, no. 5, pp. 1180–1187, 2003.

[80] J. M. Singer and C. M. Plotz, "The latex fixation test," *The American Journal of Medicine*, vol. 21, no. 6, pp. 888–892, Dec. 1956.

[81] G. F. . K. C. C. J. S. B. and S. A. M. 2007. J. M. and A. M. M. Brooks, *Medical Microbiology*, 24th ed. New York: McGraw Hill Co. Inc., 2007.

[82] Y. Moser, T. Lehnert, and M. a M. Gijs, "On-chip immuno-agglutination assay with analyte capture by dynamic manipulation of superparamagnetic beads.," *Lab on a chip*, vol. 9, no. 22, pp. 3261–7, Nov. 2009.

[83] "Light-Scattering Assays."

[84] J. Baudry, C. Rouzeau, C. Goubault, C. Robic, L. Cohen-Tannoudji, a Koenig, E. Bertrand, and J. Bibette, "Acceleration of the recognition rate between grafted ligands and receptors with magnetic forces.," *Proceedings of the National Academy of Sciences of the United States of America*, vol. 103, no. 44, pp. 16076–8, Oct. 2006.

[85] C. P. Price and D. J. Newman, *Principles and practice of immunoassay*. 1997.

[86] Q. Xiang, G. Hu, Y. Gao, and D. Li, "Miniaturized immunoassay microfluidic system with electrokinetic control.," *Biosensors & bioelectronics*, vol. 21, no. 10, pp. 2006–9, Apr. 2006.

[87] S. K. Sia, V. Linder, B. A. Parviz, A. Siegel, and G. M. Whitesides, "An integrated approach to a portable and low-cost immunoassay for resource-poor settings.," *Angewandte Chemie (International ed. in English)*, vol. 43, no. 4, pp. 498–502, Jan. 2004.

[88] M. Wolf, D. Juncker, B. Michel, P. Hunziker, and E. Delamarche, "Simultaneous detection of C-reactive protein and other cardiac markers in human plasma using micromosaic immunoassays and self-regulating microfluidic networks.," *Biosensors & bioelectronics*, vol. 19, no. 10, pp. 1193–202, May 2004.

[89] T. K. C. E.P. Diamandis, "Potentiometric titration of pharmaceutical compounds in formulations with sodium tetraphenylborate," *Analytica Chimica Acta*, vol. 152, pp. 281–284, 1983.

[90] L. E. M. MILES and C. N. HALES, "Labelled Antibodies and Immunological Assay Systems," *Nature*, vol. 219, no. 5150, pp. 186–189, Jul. 1968.

[91] D. M. Bruls, T. H. Evers, J. a H. Kahlman, P. J. W. van Lankvelt, M. Ovsyanko, E. G. M. Pelssers, J. J. H. B. Schleipen, F. K. de Theije, C. a Verschuren, T. van der Wijk, J. B. a van Zon, W. U. Dittmer, a H. J. Immink, J. H. Nieuwenhuis, and M. W. J. Prins, "Rapid integrated biosensor for multiplexed immunoassays based on actuated magnetic nanoparticles.," *Lab on a chip*, vol. 9, no. 24, pp. 3504–10, Dec. 2009.

[92] H. Jiang, X. Weng, and D. Li, "Microfluidic whole-blood immunoassays," *Microfluidics and Nanofluidics*, vol. 10, no. 5, pp. 941–964, Oct. 2010.

[93] X. Wen, H. He, and L. J. Lee, “Specific antibody immobilization with biotin-poly(L-lysine)-g-poly(ethylene glycol) and protein A on microfluidic chips.,” *Journal of immunological methods*, vol. 350, no. 1–2, pp. 97–105, Oct. 2009.

[94] A. Bange, H. B. Halsall, and W. R. Heineman, “Microfluidic immunosensor systems.,” *Biosensors & bioelectronics*, vol. 20, no. 12, pp. 2488–503, Jun. 2005.

[95] B. Teste, F. Malloggi, A.-L. Gassner, T. Georgelin, J.-M. Siaugue, A. Varenne, H. Girault, and S. Descroix, “Magnetic core shell nanoparticles trapping in a microdevice generating high magnetic gradient.,” *Lab on a chip*, vol. 11, no. 5, pp. 833–40, Mar. 2011.

[96] H. Andersson, C. Jönsson, C. Moberg, and G. Stemme, “Self-assembled and self-sorted array of chemically active beads for analytical and biochemical screening.,” *Talanta*, vol. 56, no. 2, pp. 301–8, Feb. 2002.

[97] R. Oleschuk, L. Shultz-Lockyear, Y. Ning, and D. Harrison, “Trapping of bead-based reagents within microfluidic systems: on-chip solid-phase extraction and electrochromatography,” *Analytical chemistry*, vol. 72, no. 3, pp. 585–90, Feb. 2000.

[98] K. Sato, M. Tokeshi, T. Odake, H. Kimura, T. Ooi, M. Nakao, and T. Kitamori, “Integration of an immunosorbent assay system: analysis of secretory human immunoglobulin A on polystyrene beads in a microchip.,” *Analytical chemistry*, vol. 72, no. 6, pp. 1144–7, Mar. 2000.

[99] M. Ikami, A. Kawakami, M. Kakuta, Y. Okamoto, N. Kaji, M. Tokeshi, and Y. Baba, “Immuno-pillar chip: a new platform for rapid and easy-to-use immunoassay.,” *Lab on a chip*, vol. 10, no. 24, pp. 3335–40, Dec. 2010.

[100] K. Svoboda and S. M. Block, “Biological applications of optical forces.,” *Annual review of biophysics and biomolecular structure*, vol. 23, pp. 247–85, Jan. 1994.

[101] A. Ashkin, J. M. Dziedzic, and T. Yamane, “Optical trapping and manipulation of single cells using infrared laser beams.,” *Nature*, vol. 330, no. 6150, pp. 769–71, Jan. 1987.

[102] A. Haldar, S. Pal, B. Roy, S. Gupta, and A. Banerjee, “Self-assembly of microparticles in stable ring structures in an optical trap,” *Physical Review A*, vol. 85, no. 3, pp. 1–9, Mar. 2012.

[103] T. Laurell, F. Petersson, and A. Nilsson, “Chip integrated strategies for acoustic separation and manipulation of cells and particles.,” *Chemical Society reviews*, vol. 36, no. 3, pp. 492–506, Mar. 2007.

[104] H. M. HERTZ, “STANDING-WAVE ACOUSTIC TRAP FOR NONINTRUSIVE POSITIONING OF MICROPARTICLES ,” *Journal of applied physics*, vol. 78, no. 8, pp. 4845–4849, 1995.

[105] M. Wiklund and H. M. Hertz, “Ultrasonic enhancement of bead-based bioaffinity assays.,” *Lab on a chip*, vol. 6, no. 10, pp. 1279–92, Oct. 2006.

[106] L. Johansson, J. Enlund, S. Johansson, I. Katardjiev, and V. Yantchev, “Surface acoustic wave induced particle manipulation in a PDMS channel-principle concepts for continuous flow applications.,” *Biomedical microdevices*, vol. 14, no. 2, pp. 279–89, Apr. 2012.

[107] H. A. Pohl, *Dielectrophoresis: The Behavior of Neutral Matter in Nonuniform Electric Fields*. Cambridge University Press, 1978, p. 579.

[108] R. Tornay, T. Braschler, N. Demierre, B. Steitz, A. Finka, H. Hofmann, J. A. Hubbell, and P. Renaud, "Dielectrophoresis-based particle exchanger for the manipulation and surface functionalization of particles.," *Lab on a chip*, vol. 8, no. 2, pp. 267–73, Feb. 2008.

[109] J. Ramón-Azcón, T. Yasukawa, H. J. Lee, T. Matsue, F. Sánchez-Baeza, M.-P. Marco, and F. Mizutani, "Competitive multi-immunosensing of pesticides based on the particle manipulation with negative dielectrophoresis.," *Biosensors and Bioelectronics*, vol. 25, no. 8, pp. 1928–1933, 2010.

[110] S. Miltenyi, W. Müller, W. Weichel, and A. Radbruch, "High gradient magnetic cell separation with MACS.," *Cytometry*, vol. 11, no. 2, pp. 231–8, Jan. 1990.

[111] S. Østergaard, G. Blankenstein, H. Dirac, and O. Leistiko, "A novel approach to the automation of clinical chemistry by controlled manipulation of magnetic particles," *Journal of Magnetism and Magnetic Materials*, vol. 194, no. 1–3, pp. 156–162, Apr. 1999.

[112] X. Liu, Y. Guan, Y. Yang, Z. Ma, X. Wu, and H. Liu, "Preparation of superparamagnetic immunomicrospheres and application for antibody purification," *Journal of Applied Polymer Science*, vol. 94, no. 5, pp. 2205–2211, Dec. 2004.

[113] X. Liu, Y. Guan, H. Liu, Z. Ma, Y. Yang, and X. Wu, "Preparation and characterization of magnetic polymer nanospheres with high protein binding capacity," *Journal of Magnetism and Magnetic Materials*, vol. 293, no. 1, pp. 111–118, May 2005.

[114] C. H. AHN, M. G. ALLEN, W. TRIMMER, Y.-N. JUN, and S. ERRAMILLI, "A Fully Integrated Micromachined Magnetic Particle Separator.pdf," *Journal of microelectromechanical systems*, vol. 5, no. 3, pp. 151–158, 1996.

[115] J.-W. Choi, C. H. Ahn, S. Bhansali, and H. T. Henderson, "A new magnetic bead-based, filterless bio-separator with planar electromagnet surfaces for integrated bio-detection systems," *Sensors and Actuators B: Chemical*, vol. 68, no. 1–3, pp. 34–39, Aug. 2000.

[116] J. W. Choi, T. M. Liakopoulos, and C. H. Ahn, "An on-chip magnetic bead separator using spiral electromagnets with semi-encapsulated permalloy.," *Biosensors & bioelectronics*, vol. 16, no. 6, pp. 409–16, Aug. 2001.

[117] J.-W. Choi, K. W. Oh, J. H. Thomas, W. R. Heineman, H. B. Halsall, J. H. Nevin, A. J. Helmicki, H. T. Henderson, and C. H. Ahn, "An integrated microfluidic biochemical detection system for protein analysis with magnetic bead-based sampling capabilities.," *Lab on a chip*, vol. 2, no. 1, pp. 27–30, Feb. 2002.

[118] a Rida and M. a M. Gijs, "Manipulation of self-assembled structures of magnetic beads for microfluidic mixing and assaying.," *Analytical chemistry*, vol. 76, no. 21, pp. 6239–46, Nov. 2004.

[119] A. RIDAA and M. A. M. GIJS, "Dynamics of magnetically retained supraparticle structures in a liquid flow," *Applied physics letters*, vol. 85, no. 21, pp. 4986–4988, 2004.

[120] K. Smistrup, B. G. Kjeldsen, J. L. Reimers, M. Dufva, J. Petersen, and M. F. Hansen, "On-chip magnetic bead microarray using hydrodynamic focusing in a passive magnetic separator.," *Lab on a chip*, vol. 5, no. 11, pp. 1315–9, Nov. 2005.

[121] U. LEHMANN, S. HADJIDJ, V. K. PARASHARA, C. VANDEVYVER, A. RIDA, and M. A. M. GIJS, "Two-dimensional magnetic manipulation of microdroplets on a chip as a platform

for bioanalytical applications," *Sensors and actuators. B, Chemical*, vol. 117, no. 2, pp. 457–463.

[122] Y. Moser, T. Lehnert, and M. a. M. Gijs, "Quadrupolar magnetic actuation of superparamagnetic particles for enhanced microfluidic perfusion," *Applied Physics Letters*, vol. 94, no. 2, p. 022505, 2009.

[123] S. Bronzeau and N. Pamme, "Simultaneous bioassays in a microfluidic channel on plugs of different magnetic particles.," *Analytica chimica acta*, vol. 609, no. 1, pp. 105–12, Feb. 2008.

[124] M. a Hayes, T. N. Polson, a N. Phayre, and a a Garcia, "Flow-based microimmunoassay.," *Analytical chemistry*, vol. 73, no. 24, pp. 5896–902, Dec. 2001.

[125] M. Slovakova, N. Minc, Z. Bilkova, C. Smadja, W. Faigle, C. Fütterer, M. Taverna, and J.-L. Viovy, "Use of self assembled magnetic beads for on-chip protein digestion.," *Lab on a chip*, vol. 5, no. 9, pp. 935–42, Sep. 2005.

[126] N. V Zaytseva, V. N. Goral, R. a Montagna, and A. J. Baeumner, "Development of a microfluidic biosensor module for pathogen detection.," *Lab on a chip*, vol. 5, no. 8, pp. 805–11, Aug. 2005.

[127] A.-L. Gassner, M. Abonnenc, H.-X. Chen, J. Morandini, J. Josserand, J. S. Rossier, J.-M. Busnel, and H. H. Girault, "Magnetic forces produced by rectangular permanent magnets in static microsystems.," *Lab on a chip*, vol. 9, no. 16, pp. 2356–63, Aug. 2009.

[128] F. Lacharme, C. Vandevyver, and M. A. M. Gijs, "Full on-chip nanoliter immunoassay by geometrical magnetic trapping of nanoparticle chains.," *Analytical chemistry*, vol. 80, no. 8, pp. 2905–10, Apr. 2008.

[129] M. a M. Gijs, F. Lacharme, and U. Lehmann, "Microfluidic applications of magnetic particles for biological analysis and catalysis.," *Chemical reviews*, vol. 110, no. 3, pp. 1518–63, Mar. 2010.

[130] N. Pamme and A. Manz, "On-chip free-flow magnetophoresis: continuous flow separation of magnetic particles and agglomerates.," *Analytical Chemistry*, vol. 76, no. 24, pp. 7250–7256, 2004.

[131] S. A. Peyman, A. Iles, and N. Pamme, "Mobile magnetic particles as solid-supports for rapid surface-based bioanalysis in continuous flow.," *Lab on a chip*, vol. 9, no. 21, pp. 3110–7, Nov. 2009.

[132] L. A. Sasso and J. D. Zahn, "Continuous Microfluidic Biosensing With Conjugated Paramagnetic Beads," in *Volume 13: Nano-Manufacturing Technology; and Micro and Nano Systems, Parts A and B*, 2008, vol. 2008, no. 48746, pp. 941–944.

[133] M. Zborowski, L. Sun, L. R. Moore, P. Stephen Williams, and J. J. Chalmers, "Continuous cell separation using novel magnetic quadrupole flow sorter," *Journal of Magnetism and Magnetic Materials*, vol. 194, no. 1–3, pp. 224–230, Apr. 1999.

[134] R. WIRIX-SPEETJENS, W. FYEN, X. KAIDONG, J. DE BOECK, and G. BORGHS, "A force study of on-chip magnetic particle transport based on tapered conductors," *IEEE transactions on magnetics*, vol. 41, no. 10, pp. 4128–4133.

[135] G. Fonnum, C. Johansson, a Molteberg, S. Morup, and E. Aksnes, “Characterisation of Dynabeads by magnetization measurements and Mössbauer spectroscopy,” *Journal of Magnetism and Magnetic Materials*, vol. 293, no. 1, pp. 41–47, May 2005.

[136] S. Julian Seymour, *Classical Electrodynamics*. Westview Press, 1998.

[137] C. H. AHN, M. G. ALLEN, W. TRIMMER, Y.-N. JUN, and S. ERRAMILLI, “A fully integrated micromachined magnetic particle separator,” *Journal of microelectromechanical systems*, vol. 5, no. 3, pp. 151–158, 1996.

[138] B. Richard and S. Fritz, *Electromagnetic Fields and Interactions*. Dover, New York: Courier Dover Publications, 1982.

[139] A. Engel and T. Physik, “On the electromagnetic force on a polarizable body,” no. 3, pp. 1–8.

[140] S. S. Shevkoplyas, A. C. Siegel, R. M. Westervelt, M. G. Prentiss, and G. M. Whitesides, “The force acting on a superparamagnetic bead due to an applied magnetic field.,” *Lab on a chip*, vol. 7, no. 10, pp. 1294–302, Oct. 2007.

[141] R. E. Rosensweig, *Ferrohydrodynamics*. Courier Dover Publications, 1997, p. 350.

[142] N. Minc, “Microfluidique et billes magnetiques autoorganisees pour les analyses biologiques,” Paris VI, 2005.

[143] M. A. Hayes, N. A. Polson, and A. A. Garcia, “Active Control of Dynamic Supraparticle Structures in Microchannels,” *Earth*, no. 16, pp. 2866–2871, 2001.

[144] N. Minc, “Microfuidique et billes magnétiques auto-organisées pour les analyses biologiques,” l’Universit¶e Paris VI, 2005.

[145] J.-C. Bacri, R. Perzynski, D. Salin, V. Cabuil, and R. Massart, “Magnetic colloidal properties of ionic ferrofluids,” *Journal of Magnetism and Magnetic Materials*, vol. 62, no. 1, pp. 36–46, Nov. 1986.

[146] L. Motte, “Ferrofluides - Nanoparticules superparamagnétiques,” vol. 33, no. 0, 2012.

[147] M. Warren, S. Julian, and H. Peter, *Unit Operations of Chemical Engineering*. McGraw-Hill, 2004.

[148] R. H. . Perry and D. . Green, *Perry’s Chemical Engineers' Handbook (7th Edition) - Knovel*. McGraw-Hill, 1997.

[149] H. Richard G., *Fundamentals of Particle Technology*. Midland informations technology and publishing, 2002.

[150] S. Ergun and a. a. Orning, “Fluid Flow through Randomly Packed Columns and Fluidized Beds,” *Industrial & Engineering Chemistry*, vol. 41, no. 6, pp. 1179–1184, Jun. 1949.

[151] B. Formisani, R. Girimonte, L. Mancuso, and R. Cosenza, “Analysis of the fluidization process of particle beds at high temperature,” vol. 53, no. 5, 1998.

[152] D. J. Harrison, A. Manz, Z. Fan, H. Luedi, and H. M. Widmer, "Capillary electrophoresis and sample injection systems integrated on a planar glass chip," *Analytical Chemistry*, vol. 64, no. 17, pp. 1926–1932, Sep. 1992.

[153] D. R. Emerson, K. Cieślicki, X. Gu, and R. W. Barber, "Biomimetic design of microfluidic manifolds based on a generalised Murray's law.," *Lab on a chip*, vol. 6, no. 3, pp. 447–54, Mar. 2006.

[154] R. W. Barber and D. R. Emerson, "Optimal design of microfluidic networks using biologically inspired principles," *Microfluidics and Nanofluidics*, vol. 4, no. 3, pp. 179–191, Mar. 2007.

[155] N. Pamme, J. Eijkel, and a Manz, "On-chip free-flow magnetophoresis: Separation and detection of mixtures of magnetic particles in continuous flow," *Journal of Magnetism and Magnetic Materials*, vol. 307, no. 2, pp. 237–244, Dec. 2006.

[156] J. Verbarg, K. Kamgar-Parsi, A. R. Shields, P. B. Howell, and F. S. Ligler, "Spinning magnetic trap for automated microfluidic assay systems.," *Lab on a chip*, vol. 12, no. 10, pp. 1793–9, Apr. 2012.

[157] J. Hardy and D. J. Selkoe, "The amyloid hypothesis of Alzheimer's disease: progress and problems on the road to therapeutics.," *Science (New York, N.Y.)*, vol. 297, no. 5580, pp. 353–6, Jul. 2002.

[158] M. Chiari, M. Cretich, and J. Horvath, "A new absorbed coating for DNA fragment analysis by capillary electrophoresis.," *Electrophoresis*, vol. 21, no. 8, pp. 1521–6, May 2000.

[159] Y. Shakalisava, M. Poitevin, J.-L. Viovy, and S. Descroix, "Versatile method for electroosmotic flow measurements in microchip electrophoresis.," *Journal of chromatography. A*, vol. 1216, no. 6, pp. 1030–3, Feb. 2009.

[160] R. Mohamadi, "An integrated microfluidic system for immunocapture, preconcentration and electrophoresis of polypeptides: application to Aβ peptides in human cerebrospinal fluid," *Biomicrofluidics*.

[161] R. Fukuyama, T. Mizuno, S. Mori, K. Nakajima, S. Fushiki, and K. Yanagisawa, "Age-dependent change in the levels of Abeta40 and Abeta42 in cerebrospinal fluid from control subjects, and a decrease in the ratio of Abeta42 to Abeta40 level in cerebrospinal fluid from Alzheimer's disease patients.," *European neurology*, vol. 43, no. 3, pp. 155–60, Jan. 2000.

[162] R. Motter, C. Vigo-Pelfrey, D. Kholodenko, R. Barbour, K. Johnson-Wood, D. Galasko, L. Chang, B. Miller, C. Clark, and R. Green, "Reduction of beta-amyloid peptide42 in the cerebrospinal fluid of patients with Alzheimer's disease.," *Annals of neurology*, vol. 38, no. 4, pp. 643–8, Oct. 1995.

[163] C. Fütterer, N. Minc, V. Bormuth, J. Codarbox, P. Laval, J. Rossier, I. Curie, P. M. Curie, and F. E-mail, "Injection and flow control system for microchannels," pp. 351–356, 2005.


Immunoassay
Magnetophoresis
elution
Design
Chemical
Flow distribution
Microchip
Pressure drop
Microparticles
porosity
Viscous
Structure
Fluidized bed
fluidized bed
flow rate
design
principle
Microchannel
Microparticle capture
fluidized beds
Immunoassay
and
mechanical
stop and go
Beads
On chip
Particle
fluid resistance
Darcy's law
properties
Flow distribution
microfluidics
trapping
Microchip
devices
Superparamagnetic
Magnetic
mobility
Magnetic bead
particles
hysteresis
Heterogeneous
Pressure drop
Drag forces
particles
device
Magnetic force
microparticle
On Chip
systems
and
Magnetic
manipulation
permanent
Viscous
Chemical
magnetic
device
elution
Fluid flow
Fluid resistance
Mechanical
Microfluidics
magnets
capture
immobilization
microfluidics
bioassays
Chemical
Magnetic bead
microparticle
particle
Reynolds number
On Chip
Chemical
Permanent plug
plug
mobility
microfluidic
Viscous
Magnetic force
Lab on a Chip
Mechanical
Magnetophoresis
fluid resistance
interaction
particle distribution
Beads
physics
Mechanical
devices
Pressure flow
preconcentration
forces
drag
particle
Particle
Flow control
magnetic plug
physics and
Flow control
particle distribution
trapping
hysteresis
Particle
preconcentration
On chip
handling
magnetic bed
Superparamagnetic
immunoassay
bed porosity
magnetic bead
plug
magnet
magnets
trapping
stop and go
On chip
microfluidic
Lab on a Chip
bioassays
Fluid flow
Immunoextraction
Darcy's law
Minimum fluidisation velocity
Microfluidics
Spatial magnetic field
fluidized bed
immunoassays
elution
Microparticle
Structure
properties
drag force
Immunoextraction
drag force
device
bioanalysis
mechanical